2D materials for Magnetic and Optoelectronic Sensing Applications

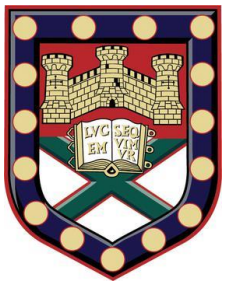

Submitted by Saad Fadhil Ramadhan Alkhalifa to the University of Exeter as a thesis for the degree of Doctor of Philosophy in Physics

July 2018

I certify that all material in this thesis which is not my own work has been identified and that no material has previously been submitted and approved for the award of a degree by this or any other University.

Saad Fadhil Ramadhan Alkhalifa

July, 2018

Abstract

In the last decade, the emerging classes of two-dimensional (2D) materials have been studied as potential candidates for various sensing technologies, including magnetic and optoelectronic detectors. Within the quickly growing portfolio of 2D materials, graphene and semiconducting transition metal dichalcogenides (TMDs) have emerged as attractive candidates for various sensor applications because of their unique properties such as extreme thickness, excellent electrical and optical properties.

In this thesis, I have exploited the unique properties of graphene and TMDs materials to develop 2D detectors based on field effect transistors for sensing magnetic field and light. In the first part of this thesis I have shown how the sensitivity of the properties of 2D materials to their surrounding environment can be turned into a feature useful to create new types of magnetic field sensors. The first experimental demonstration of this concept involved the use of graphene deposited on hexagonal Boron Nitride (h-BN), where the inevitable contaminations occurring at the interface of the two materials was used to generate a large magnetoresistance (MR) for a magnetic field sensor. Specifically, I have demonstrated that the contaminations generate an inhomogeneity in the carrier mobility throughout the channel, which is a required ingredient for magnetic field sensing based on linear magnetoresistance (LMR). Another approach I used to make a LMR sensor was by exploiting the large dependence of the mobility in graphene on the Fermi level position. This concept was used to generate two parallel electron gases with different mobility by tuning the Fermi level with an electrical field employing a field effect transistor. The second part of the thesis is focussed on strategies to reduce the impact of the surrounding environment on the properties of 2D materials in order to improve their performance. In particular, I used a 2D heterostructure encapsulated in an ionic polymer to make

a highly responsive graphene-TMD photodetector. In this device, the ionic polymer covering the heterostructure was employed to screen the long-lived charge traps that limit the speed of such detectors, resulting in a drastic improvement of the detector responsivity properties. Finally, some of the 2D materials properties are very sensitive to the configuration of the electronics measurement setup. For example, effects behind spintronic and valleytronic concepts require non-local electrical transport measurement. We built a novel circuit that enables the detection of such effects without concern about the spurious contributions.

Acknowledgements

The work in this thesis would not have been achieved without the guidance, support and friendship of many people throughout the amazing journey of my PhD.

First of all, I owe a deep debt of gratitude and thanks to my both supervisors Prof. Monica Craciun and Prof. Saverio Russo who gave me the possibility to conduct my PhD in their group. I enjoyed an excellent working environment, in which they gave me direction, asking insightful questions and plenty of freedom to pursue my own ideas. It was a great pleasure to work with them.

I should give special thanks to all my colleagues and friends in Russo/Craciun lab. Without whom this thesis would not have been possible and providing such a friendly environment. I have been fortunate to work with them. I would like to thank Jake Mehew, Matt Barnes, Namphung Peimyoo, Adolfo De Sanctis, Freddie Withers and Janire Escolar Ulibarri, Gareth Jones, Mohsin Aziz, Iddo Amit, Selim Unal, Ana Neves, Nicola Townsend, Adam Woodgate, Peng Tian. I would to give more thanks to Matt Barnes, together we developed room temperature magnetic field system. Adolfo De Sanctis to do Raman analysing and build optocoupler circuit. Mohsin Aziz for assisting me in early measurements. Amit help in AFM analysing.

Above all, I would like to thank the people who mean a lot for me, my mother who was loving to see me in this position, my father, brothers, sisters and the rest of the family for dedication many years of support during my undergraduate studies that provided the foundation for my work. My wife Nada Alahmed for her unfailing love and constant support, for all the late nights and early mornings. Her support and encouragement were in the end what made this dissertation possible. I very appreciate her for looking after our adoring kids (Mohammed, Marya and Taym). I consider myself the luckiest in the world to have such a lovely family. I should not forget all my friends who support me to reach this point. Finally, thanks to my

sponsor The Higher Committee For Education Development in Iraq (HCED-Iraq) to give my this opportunity to do my PhD in uk.

Contents

Figures

List of Abbreviation

2D Two-Dimensional

TMDC Transition Metal

Dichalcogenide

Au Gold

CVD Chemical Vapor Deposition

DOS Density of States

EBL Electron Beam Lithography

EQE External Quantum Efficiency

FET Field-effect Transistor

IPA Isopropyl Alcohol

IQE Internal Quantum Efficiency

LiClO4 Lithium Perchlorate

MEK Methyl Ethyl Ketone

MIBK Methyl Isobutyl Ketone

NEP Noise Equivalent Power

PEO Poly (ethylene oxide)

PMGI Polymethylglumarimide

PMMA Poly-methyl Methacrylate

SiO2 Silicon Dioxide

WS2 Tungsten Disulfide

Chapter 1

Introduction

1.1 Sensor based on two-dimensional (2D) materials

The requirement for small dimensionality is the most important demand for the future emerging technologies. 2D materials have attracted growing attention since the isolation of graphene in 2004 because of their unique structural and electronic properties, as well as their extraordinary capabilities that can be exploited in sensing applications. The very high surface area to volume ratio of 2D materials enables the development of a plethora of sensors, which possess exceptional sensitivity. Since they have distinct transduction properties, 2D materials are considered as the most promising candidate materials for the fabrication of rapid and sensitive sensors for quantitative physical, chemical, and biological detection. The production of high-quality and low-cost 2D materials has progressed quickly in the past few years, opening the door for the development of many different 2D material-based sensors. However, research on 2D material-based sensors is still at an early stage and in some areas far from commercial applications due to the difficulties in fabricating devices with good uniformity and reproducibility. Therefore, more fundamental research and development are needed on various aspects of this field. Firstly, it is critical to have a deep understanding of the behaviour of various 2D materials in sensor devices, both from an experimental and theoretical point of view, as well as of the detection mechanisms and interactions with the surrounding environment. Next, the research prototype devices are normally tested in controllable conditions while many interference factors widely existing in real life environment have not been considered. Therefore, the selectivity and stability of the 2D material-based sensors need to be characterized and optimized for real life environment use. Moreover, the big range of available materials offers a wide opportunity for engineering 2D heterostructures, potentially unveiling as-yet unexplored phenomena. These

materials enable the designing of next generation low-power, low-loss and ultra-energy-efficient active for next-generation “green electronics”.

One of the most popular 2D materials is graphene because it holds extraordinary physical properties. It exhibits record high values of charge carrier mobility[1], high flexibility[2], efficient transmittance (97:7%)[3] and easily mimics the adjacent materials and the environment. Therefore, this thesis is mainly focused on graphene as a base material. Graphene has been shown to operate as a high-speed photodetector with response times comparable to conventional silicon-based devices, but the absence of a bandgap and lack of significant gain mechanism limits its use for ultrasensitive light detection. Other emerging atomically thin materials, e.g. transition metal dichalcogenides (TMDs) such as WS_2, have complementary characteristics to graphene such as semiconducting properties necessary for transistor applications. Thus, in this thesis the combination of graphene with semiconducting WS_2 materials in heterostructure photodetectors was used to enhance light absorption and provide an internal gain mechanism.

1.2 This thesis

The aim of this thesis is to demonstrate highly sensitive sensors for light and magnetic field based on graphene and graphene heterostructures with other 2D materials. To this end, I have exploited the unique properties of graphene and TMDs materials to develop 2D detectors based on field effect transistors for sensing magnetic field and light. In the first part of this thesis I have shown how the sensitivity of the properties of 2D materials to their surrounding environment can be turned into a feature useful to create new types of magnetic field sensors. The second part of the thesis is focussed on strategies to reduce the impact of the surrounding environment on the properties of 2D materials in order to improve their performance.

Chapter 2 will outline the physical concepts that are necessary to understand the experimental findings presented in this work. In this chapter, I will briefly review the band structure of monolayer graphene and of TMDs. I will also dedicate attention to some background concepts relevant for the understanding of charge transport and Raman spectroscopy in graphene, as these are two main techniques that I used in this thesis to understand the detection mechanisms in the graphene sensors. The following two sections will focus on the mechanisms behind magnetic field and light sensing. In the magnetic field sensing section, I will focus on the original source of the linear magnetoresistance (LMR), while in the light sensing section I will be focussing on the fundamental aspects of photocurrent generation mechanisms in materials.

Chapter 3 will describe the most important experimental methods, which I used in the fabrication and characterisation of the sensor devices. These include the fabrication of heterostructure field effect transistors (FET). I will then discuss how Raman spectroscopy can be used for sensing strain and doping in graphene. Furthermore, I will describe the electrical and opto-electrical setups used. Finally, I will discuss how the ionic polymer environment affects the properties of the devices.

Chapter 4 will present the experimental investigations conducted to probe linear magnetoresistance (LMR) of monolayer graphene deposited on hexagonal Boron Nitride (h-BN). In this system, the inevitable contaminations occurring at the interface of the two materials in the form of bubles, was used to generate a large magnetoresistance (MR). Through careful examination of the impact of bubbles at the interface between graphene and hBN, I gained valuable information as to how these bubbles play a big role in generating an inhomogeneity in the carrier mobility throughout the channel, which is a required ingredient for magnetic field sensing

based on LMR. Finally, I show how this inhomogeneity in the carrier mobility can be engineered to enhance the LMR response.

Chapter 5 will present another experimental approach for improving the LMR response of graphene employing two parallel electron gases with different charge carrier motilities. For this purpose, different experimental configurations were explored. These configurations were based on a high difference in the carrier motilities between the two gases to obtain a high MR response.

In **Chapter 6** I will show how an ionic polymer electrolyte can improve the optical responsivity of graphene-WS_2 hybrid photodetectors. In this device, the ionic polymer covering the heterostructure was employed to screen the long-lived charge traps that limit the speed of such detectors, resulting in a drastic improvement of the detector responsivity properties. The optoelectronic properties of this heterostructure are investigated using a scanning photocurrent microscopy and bulk illumination methods.

Chapter 7 will be focused on reducing the impact of the electronics measurement setup on the effects behind some of the 2D materials properties. I will discuss a circuit that was built for high-impedance and non-local electrical transport measurements. I will show how this circuit can be used not only to reduce the environment noise but also to eliminate and distinguish spurious signals from real signals.

References

1. Banszerus L, Schmitz M, Engels S, Dauber J, Oellers M, Haupt F, *et al.* Ultrahigh-mobility graphene devices from chemical vapor deposition on reusable copper. *Science Advances* 2015, **1**(6).

2. Lee C, Wei X, Kysar JW, Hone J. Measurement of the Elastic Properties and Intrinsic Strength of Monolayer Graphene. *Science* 2008, **321**(5887)**:** 385-388.

3. Nair RR, Blake P, Grigorenko AN, Novoselov KS, Booth TJ, Stauber T, *et al.* Fine Structure Constant Defines Visual Transparency of Graphene. *Science* 2008, **320**(5881)**:** 1308-1308.

Chapter 2

Background Concepts

2.1 Graphene Band structure

2.1.1 Direct and Reciprocal Lattice of Graphene

Graphene is a monolayer of carbon atoms with sp^2 hybridization of the orbitals with a honeycomb crystal structure. This material is a single layer of graphite. The length of each carbon–carbon bond is approximately $a_{C-C} \approx 1.42\ A^{\circ}$ .The honeycomb structure can be characterized as a composite Bravais lattice with two atoms in the basis, indicated as A and B in **Figure (2-1a)**.

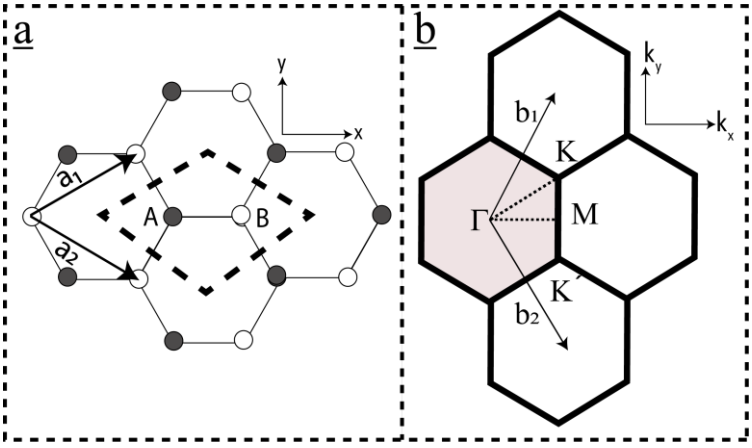

Figure 2- 1 Graphene lattice **a-** Direct lattice showing the unit cell contains two atoms A and B. **b-** Reciprocal Lattice highlighting the first Brillouin zone in shaded hexagon, also indicting the high-symmetry point Γ, M and K in the Brillouin zone.

The primitive unit vectors for a lattice of graphene are

$$\overrightarrow{a_1} = a\cos 30^{\circ}\,\hat{x} + a\sin 30^{\circ}\,\hat{y} = \frac{a}{2}(3, \sqrt{3})$$

$$\overrightarrow{a_2} = a\cos 30^{\circ}\,\hat{x} - a\,\sin 30^{\circ}\,\hat{y} = \frac{a}{2}(3, -\sqrt{3})$$

The reciprocal lattice of graphene, shown in **Figure (2-1b)**, is also a hexagonal structure with reciprocal lattice vectors:

$$\vec{b}_1 = 2\pi \frac{\overrightarrow{a_2} \times \overrightarrow{a_3}}{\overrightarrow{a_1} \cdot \overrightarrow{a_2} \times \overrightarrow{a_3}} = \frac{2\pi}{3a}(1, \sqrt{3})$$

$$\vec{b}_2 = 2\pi \frac{\overrightarrow{a_3} \times \overrightarrow{a_1}}{\overrightarrow{a_1} \cdot \overrightarrow{a_2} \times \overrightarrow{a_3}} = \frac{2\pi}{3a}(1, -\sqrt{3})$$

The Brillouin zone is illustrated as the shaded area in **Figure (2-1b)**. High symmetry points within the Brillouin zone are $\Gamma = (0,0)$, $M = \left(\frac{2\pi}{3a}, 0\right)$, $K' = \left(\frac{2\pi}{3a}, -\frac{2\pi}{3\sqrt{3}a}\right)$ and $K = \left(\frac{2\pi}{3a}, \frac{2\pi}{3\sqrt{3}a}\right)$.[4]

π -orbital and charge transport

When carbon atoms are brought together to form a honeycomb lattice, each one of them has 6 electrons: two electrons fill all states in the 1s orbital, two electrons fill all states in the 2s orbital and two electrons occupy the 2p orbital, see **Figure (2-2a)**. The interaction between s-orbitals ($2s^2$) and p-orbitals ($2p^2$) of the second shell of a neighbouring carbon atom leads to the sp^2—hybridization, see **Figure (2-2b)**. In this case, two of the 2p orbitals are mixed with one 2s orbital, leading to $3sp^2$ hybridized orbitals[5]. Carbon atoms align themselves in a trigonal planar structure at 120° to each other, while the remaining $2p_z$ orbital projects perpendicularly from the lattice plane. A linear combination of atomic orbitals across the lattice leads to the formation two types of bonds. The first type is the σ bonds, in which orbitals are aligned along the lattice plane and lobes point equally away from each other in a form of a trapezium to minimize electron repulsion and to improve overlap[6]. The second type is π bonds, these are formed by the overlap of adjacent $2p_z$ orbitals to form clouds of de-localised electrons above and below the lattice plane. This arrangement is illustrated in **Figure (2-2c)**. The electrons of the σ bonds are strongly localized in between the two carbon atoms, while the electrons in the π bonds are delocalized and move freely in two clouds above and below the lattice plane.

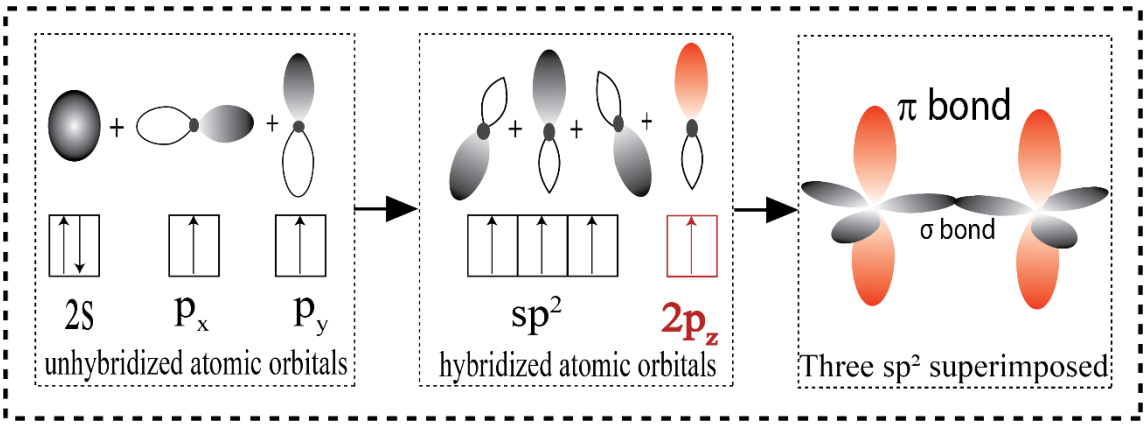

Figure 2- 2 The sp2 hybridization of carbon process.

2.1.2 Electronic Band Structure of Graphene:

The electronic structure of graphene can be accurately described by a linear combination of the partially filled sp2 orbitals, which form the π bands. Put simply, this produces a broadening of the allowed energy states which the delocalised electrons may occupy and it ultimately results in two continuous, intersecting bands with an unusual conical structure at low energy. The allowed energy states of electrons in these orbitals gives rise to a continuous band of states.

A quantitative understanding of the energy dispersion of graphene can be attained within the non-interacting tight bind approximation [4]. This model considers only the hopping of an electron from one atom to the nearest neighbour. The model is closely linked to the linear combination of atomic orbitals (LCAO) method used in chemistry. Due to the translational symmetry of the crystal, these wavefunctions must satisfy the Bloch theorem[7].

To derive the band structure of graphene (E-k relation) one needs to solve the time-independent Schrödinger equation:

$$H\psi\,(k,r) = E(k)\psi(k,r) \qquad (2-1)$$

where H is the Hamiltonian, ψ is the total wave function, E is the energy of electrons in the orbital of graphene, k is the wave vector and r is the position.

The Hamiltonian for the free-moving electron in a periodic electric potential is given by

$$H = \frac{-\hbar^2}{2m}\nabla^2 + \sum_{i}^{N} U(r - R_i) \qquad (2-2)$$

where the first term on the right-hand side of equation (2-2) is the kinetic energy operator and the latter term is the potential energy operator. R_i are the translation vectors, N is the number of primitive unit cells of the crystal, and $U(r - R_i)$ is the potential energy contribution from the atom centred in the *i*th primitive unit cell.

Valid solutions to equation (2-2) must be wavefunctions that satisfy Bloch's theorem

$$\psi(r + R) = e^{ik.R}\psi(r) \qquad (2-3)$$

R is the vector distance between two centres.

Graphene lattice has two carbon atoms, A and B, per unit cell. So, the tight-binding wavefunction is a weighted sum of the two sub-lattice (A-B) Bloch functions:

$$\psi(k, r) = C_A\Phi_A(k, r) + C_B\Phi_B(k, r) \quad (2-4)$$

Where $C_A \; and \; C_B$ are two numerical coefficients.

Hence, the total wave function can be written as a linear combination of two Bloch functions:

$$\Phi_A(k, r) = \frac{1}{\sqrt{N}}\sum_{j}^{N} e^{ik.R_{A_j}}\emptyset\left(r - R_{A_j}\right)$$

$$\Phi_B(B,r) = \frac{1}{\sqrt{N}} \sum_{j}^{N} e^{ik.R_{B_j}} \emptyset\left(r - R_{B_j}\right)$$

Where N is the number of unit cells in the lattice, the Bravais lattice vectors are R_A and R_B; $\emptyset(r - R_A)$ identifying the locations of all type A (B) atoms in the graphene lattice and $\emptyset(r - R_B)$ are the atomic wave functions of the p_z orbitals.

Inserting equation (2-4) in (2-1), we will get: -

$$C_A H\Phi_A(k,r) + C_B H\Phi_B(k,r) = E(k)C_A\Phi_A(k,r) + E(k)C_B\Phi_B(k,r)$$

This can be written in a matrix form when multiplying by complex conjugate of Φ_A, Φ_B and Integrating over all space, we can write the Schrödinger equation

$$\begin{pmatrix} H_{AA} & H_{AB} \\ H_{BA} & H_{BB} \end{pmatrix} \begin{pmatrix} c_A \\ c_B \end{pmatrix} = E \begin{pmatrix} S_{AA} & S_{AB} \\ S_{BA} & S_{BB} \end{pmatrix} \begin{pmatrix} c_A \\ c_B \end{pmatrix} \qquad (2-5)$$

where $H_{ij} = \int_\Omega \Phi_i^* H\Phi_j dr$ are the matrix elements of the Hamiltonian and $S_{ij} = \int_\Omega \Phi_i^* \Phi_j dr$ are the overlap matrix elements between Bloch functions. Ω the entire space occupied by the lattice[8].

Since the atoms in the A and B sublattices are nominally identical carbon atoms, one can set equivalent on-site energy $H_{AA} = H_{BB} = E_{2p}$ and $S_{AA} = S_{BB} = 1$. The off-diagonal terms of the matrices in equation (2-5) are given by

$$H_{AB}(k) = \int_\Omega \Phi_A^* H\Phi_B dr$$

$$H_{AB}(k) = \gamma\,(e^{-ik.R_1} + e^{-ik.R_2} + e^{-ik.R_3} \qquad (2-6)$$

where γ is often called by many names, including the nearest neighbour overlap energy, the hopping or transfer energy, or the carbon–carbon interaction energy.

Mathematically, the electron–hole symmetry forces $S_{AB}(\boldsymbol{k}) = 0$. In addition, E_{2p} is a parameter independent of **k** which can be set equal to zero without loss of generality, i.e. $H_{AA} = H_{BB} = E_{2p} = E_F = 0$. Equation (2-5) can be reduced to

$$E(k)^{\mp} = \mp\sqrt{H_{AB}(k)H_{AB}^{*}(k)} \qquad (2-7)$$

By substituting the expressions of equation (2-6) in equation (2-7), one finds the energy dispersion of the electronic states in graphene.

$$E(k)^{\mp} = \mp\sqrt{1 + 4\cos\frac{\sqrt{3}a}{2}k_x\cos\frac{a}{2}k_y + 4\cos^2\frac{a}{2}k_y} \qquad (2-8)$$

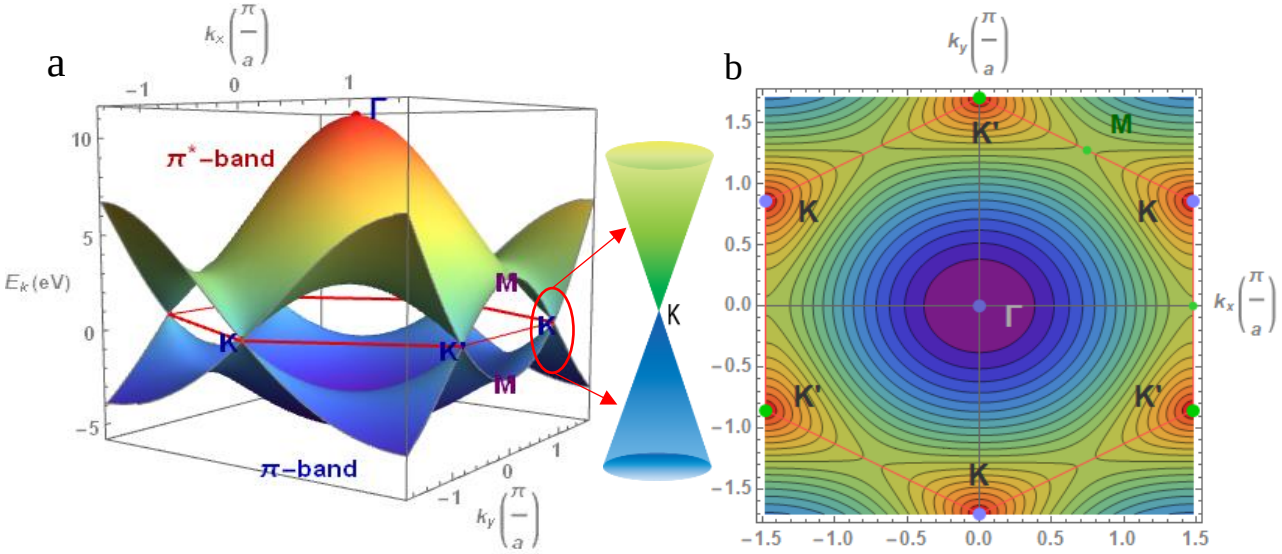

Figure 2- 3 The band structure of graphene **a-** Electronic dispersion relation for monolayer graphene in 3D and 2D plot, the 2D for π band. **b-** the states near the *K* and *K'* points form independent valleys in momentum space[46].

The six K-points in graphene where the conduction and valence bands touch are commonly referred to as Dirac points. At low energy, $E_F \approx 0$, the band structure near the K and K' points have a linear dispersion which is representative of so-called massless particles (particles with zero effective mass). Thus, equation (2-8) can simply be expressed as a linear equation:

$$E(k)^{\mp}_{linear} = \mp\hbar v_F k = \mp\hbar_F v_F \sqrt{k_x^2 + k_y^2} \quad (2-9)$$

where k is now in spherical coordinates and the Fermi velocity is defined as $v_F = (1/\hbar)(\partial E/\partial k)$ evaluated at the Fermi energy and its direction is equal to that of the wave vector. The value of the Fermi velocity is constant: $v_F = \frac{3\gamma_o a}{2} \approx 10^6 m/s$

2.1.3 Charge transport in graphene

The charge carrier mobility is an important metric for describing the efficiency of electronic transport within a given material. It is limited by collisions between charge carriers, crystal defects, and phonons (lattice vibrations).

The electronic transport properties of graphene are determined by the electronic states around the Fermi energy, π electrons. For charge carrier concentrations lower than $n < 10^{11}\ cm^{-2}$ the electronic transport properties of graphene are described by the linear band structure extending +/-1eV about the charge neutrality point[9, 10]. In undoped graphene, the Fermi level is exactly at the *K* and *K'* points. The E_F can be pulled up into the upper cones, making an n-type metal, or depressed into the lower cones, making a p-type metal, by the introduction of additional charge carriers via the electrostatic gating or chemical doping.

Generally, in 2D materials the transport of charge carriers is limited by (1) short-range or (2) long range-scattering. The former, when the length of the range is smaller than the lattice constant while the latter case where it is comparable or larger than the lattice constant[11]. Charge transport in graphene has been studied extensively experimentally[12, 13]and theoretically with specific focus on the role of Coulomb scattering[14, 15, 16, 17], short range scattering[18], electron-phonon scattering[19, 20, 21], substrate surface polar phonon scattering[19, 22, 23], and roughness[24].

In graphene the carrier density n induced per gate voltage (V_g) follows this formal relation $n = 7.3 * 10^{10} * V_{BG}$ $(cm^{-2}V^{-1})$ [25]. The Fermi energy in monolayer is $E_F = \hbar v_F k_F$, while $E_F = \hbar^2 k^2/2m^* = \pi\hbar^2 n/2m^*$ for bilayer and trilayer[26, 27], where m^* is the effective mass the 2D Fermi wave vector is k_F depends on the carrier density through $k_F = \sqrt{2\pi n}$. The density of states $D(E_F)$ in monolayer graphene is $D(E_F) = \frac{2E_F}{\pi(\hbar v_F)^2}$, while in bilayer or trilayer graphene it is constant $D(E_F) = \frac{2m}{\pi\hbar^2}$.

Note that in the Boltzmann treatment the mobility is proportional to the scattering time $\mu = \frac{eD(E_F)v_F^2\langle\tau\rangle}{2n}$. This implies that μ becomes $\mu_{Mon} = \frac{ev_F^2\langle\tau\rangle}{E_F}$ for monolayer and $\mu_{Bi,Tri} = \frac{e\langle\tau\rangle}{m}$ for bilayer and trilayer graphene[28].

The mobility for the supporting monolayer, either SiO_2 or SiC, is very sensitive to temperature because of the associated thermal excitation of surface polar phonons within the SiO_2 substrate[19], which is the commonly used substrate . However, for bilayer and trilayer the mobility increases with temperature: $\mu \, \alpha \, k_B T$ [29]. The mobility of bilayer and trilayer is mainly determined by Coulomb scattering due to its parabolic band structure. In multilayer graphene, lower layers electrostatically screen substrate phonons from interacting with charge carriers in higher layers [30, 31]. The mobility of supported monolayer graphene can reach up to $(4 * 10^4 \frac{cm^2}{V.s})$, while in suspended samples, charge carrier mobility as high as $(20 * 10^4 \frac{cm^2}{V.s})$ has been reported, which is limited by out-of-plane (flexural) phonons[20]. It should be noted, however, that the size of suspended graphene devices is typically limited due to the mechanical fragility of unsupported atomically thin films. hBN was used as a substrate and a mobility of $4* 10^4 \frac{cm^2}{Vs}$ [32] was measured due to the absence of

dangling bonds or surface charge traps in hBN. Recently, two research groups reported successful deposition of CVD grown graphene onto hBN via a dry transfer technique with charge carrier mobility as high as $300 * 10^4 \frac{cm^2}{Vs}$ [33] and $35 * 10^4 \frac{cm^2}{Vs}$ [1] at cryogenic temperatures (around 1.6K).

2.2 Raman Spectroscopy

Raman spectroscopy is a non-invasive technique which probes the interatomic vibrations of a sample molecule or crystal lattice. A laser light is irradiated onto the sample, inelastic scattering occurs between the sample and an infinitesimal fraction (10^{-6} %) of incident photons. After scattering, this small fraction of photons will be of an energy marginally lower than (Stokes scattering) or marginally greater than (anti-Stokes scattering) the photons which undergo the more common process of elastic (Rayleigh) scattering. Using an optical notch filter, inelastically scattered photons are isolated from the back scattered laser line and analysed using a spectrometer. A resultant plot of spectrometer CCD counts as a function of shift in photon wavenumber is referred to as a Raman spectrum. Peaks in the Raman spectrum of a sample material can serve as a 'fingerprint signature' of the vibrational modes specific to its chemical structure, charge carrier concentration, physical strain and a variety of other parameters. Raman spectroscopy can therefore serve as an extremely useful tool for quick, non-destructive characterisation of the physical properties of a materials. The Raman spectrum is widely measured in wavenumbers also known as Raman shift (the reciprocal of wavelength). The shift can be written as

$$\Delta\omega\ (cm^{-1}) = (1/\lambda_o) - (1/\lambda_1)$$

λ_0 is the excitation wavelength, and λ_1 is the Raman selected wavelength

2.2.1 Phonons in graphene

Monolayer graphene contains two carbons atoms in its unit cell A and B therefore there are six phonon dispersion bands, see **Figure (2-4a)**[34]; three are acoustic branches (A) and the other three are optical(O) phonon branches (1-4b). One of the acoustic (A) and optical (O) phonon modes vibrate perpendicular to the graphene plane, these are the so-called out-of-plane (o) phonon modes. The other two acoustic and optic phonon branches correspond to vibrations in the plane of graphene (i). The direction of the in-plane vibration is either parallel with the carbon-carbon atoms or perpendicular to them, referred to as Longitudinal (L) and Transverse (T) respectively. The two in-plane longitudinal modes are denoted as LA (longitudinal acoustic) and LO (longitudinal optical) phonons. The four transverse phonons are assigned to in-plane transverse acoustic (*i* TA), in-plane transverse optical (*i* TO), out-of-plane transverse acoustic (*o* TA) and out-of-plane transverse optical (*o*TO) branches, respectively[34]. At the centre of the Brillouin zone Γ, the only Raman-active mode is E_{2g}, which has two-fold degeneracy at Gamma and produces a Raman peak commonly referred to as the G band.

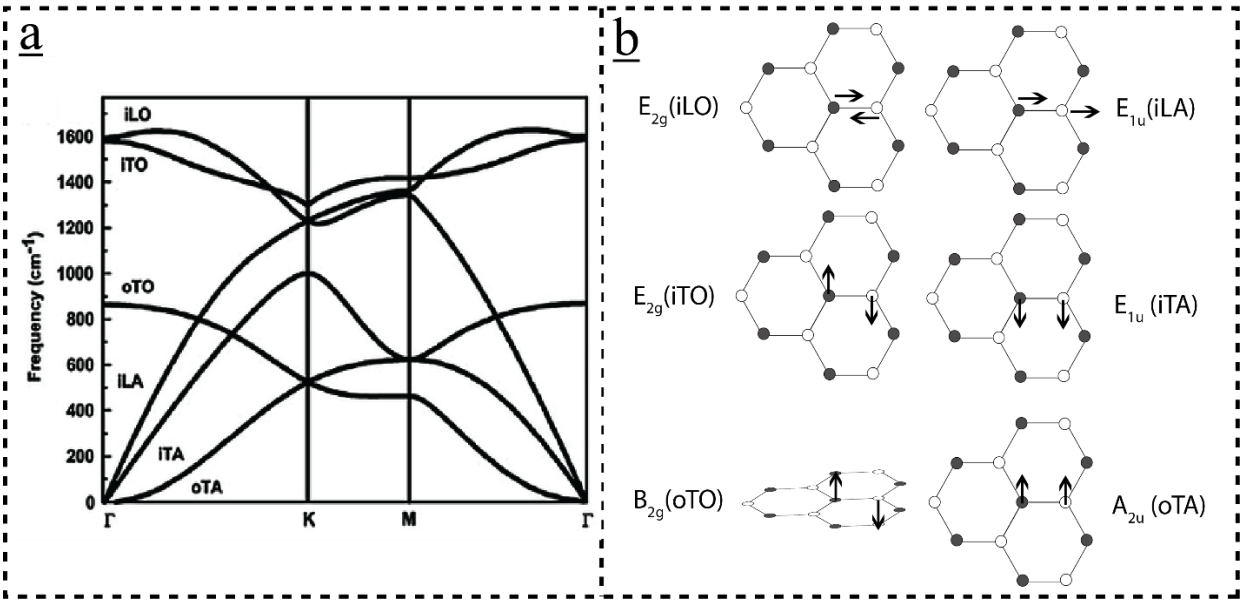

Figure 2- 4 Phonon dispersion in graphene **a-**Phonon relation of graphene[31]. **b-** Phonon eigenvectors of monolayer graphene.

2.2.2 Raman spectrum in Graphene

A typical Raman spectrum of single-layer graphene is shown in **Figure (2-5a)**. The most prominent features of monolayer graphene are the G- and 2D-bands, centred around 1583 cm^{-1} and 2700 cm^{-1}, respectively. The G peak comes from a one phonon process (first order Raman scattering) corresponding to the in-plane bond-stretching optical vibration of sp2-hybridized carbon atoms, see **Figure (2-5b)**. It is associated with the doubly degenerate (iTO and LO) phonon mode, which has E_{2g} symmetry and is located at the Γ point of the Brillouin zone (BZ), i.e. at the Brillouin zone centre. The 2D peak originates from second-order processes which require more than one phonon.

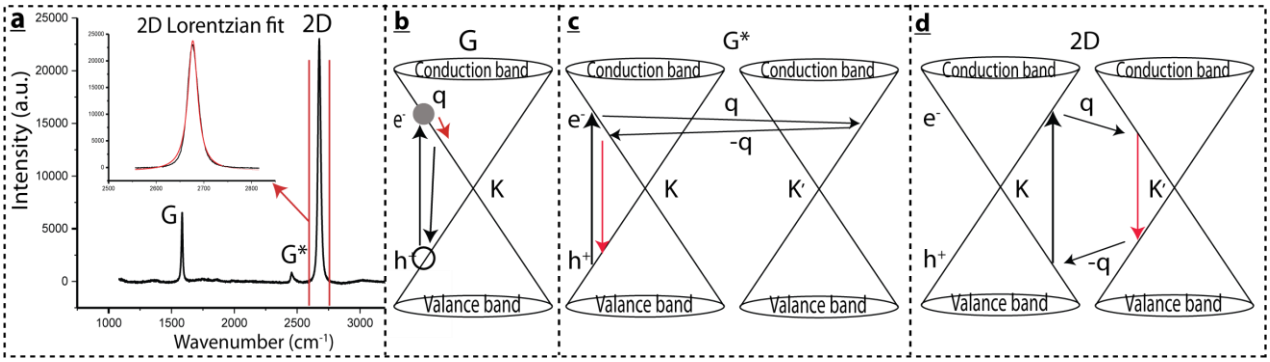

Figure 2- 5 Typical Raman spectrum of monolayer graphene **a**-Raman spectra of pristine Graphene, the inside showing the Lorentzian fit for the 2D peak. **b-c** electron dispersion for G, G* and 2D peaks respectively.

The double resonant processes are characterized by the following transitions. At first an electron is in an initial state *a* characterized by a wavevector $\boldsymbol{k}$ near the *K* point and this is excited to the conduction band state b by absorbing a photon with energy *E*1. For the G* band, the electron emits a phonon with a wavevector $\boldsymbol{q}$ and energy ω_{ph} and is scattered to the state *b* with the wave-vector $\boldsymbol{k} + \boldsymbol{q}$ near the K' point of the BZ. The electron is then scattered back by a defect to the state *c*. The backscattering changes the electron momentum by $-\boldsymbol{q}$. The electron recombines with the hole left behind in the state *i* emitting a photon with the energy *Es*. The process consists of two scattering processes: an inelastic one owing to a phonon emission and an elastic one caused by a defect. Obviously, a disorder must be present in the sample to enable the elastic process. For the 2D band, both scattering events are inelastic involving two near *K* -point phonons. As before, an electron is scattered from the initial state to the *b* state near the K'point . Then, a hole in the valence band around the *K* point is also scattered (by emitting a phonon) to a state near the K' point in the valence band. Both the electron and hole have the same wavevector $\boldsymbol{k} + \boldsymbol{q}$ now, so they eventually recombine resonantly. This can be summarised as a triple

resonance process. The 2D peak is always present since no disorder or defects are needed for inelastic scattering process to occur [34, 35, 36].

2.3 Transition metal dichalcogenides (TMDCs)

The transition metal dichalcogenides (TMDs) are a family of semiconductors. They crystallize in a 2D structure composed of $X-M-X$ (MX_2), Where M is a transition metal atom (group IV, V, VI, VII, IX or X) and a chalcogen atom (such as S, Se or Te). The stacking structure is a hexagonally packed layer of metal atoms (M) sandwiched between two layers of chalcogen atoms (X). Intralayer $M-X$ interactions are dominated by covalent bonding, whereas adjacent layers are coupled only by weak van der Waals force thus allowing easy cleavage of planes. In thermodynamic equilibrium, the structure of single-layered TMDCs form either trigonal prismatic (2H) phase or octahedral (1T) phases, corresponding to ABA and ABC stacking orders respectively. In the 2H phase, chalcogen atoms (A) located in different atomic planes occupy the same position and are located on top of each other in the direction perpendicular to the layer, whilst in the 1T phase the chalcogen atoms (A) are not in the same position, see **Figure (2-6)**[37]. In the case of multi-layered TMDCs, in addition to 2H and 1T phase there is another polymorphic structure, defined as rhombohedral (3R)[38] .The (1T) form displays metallic behaviour, whereas both (2H) and (3R) forms exhibit semiconducting behaviour.

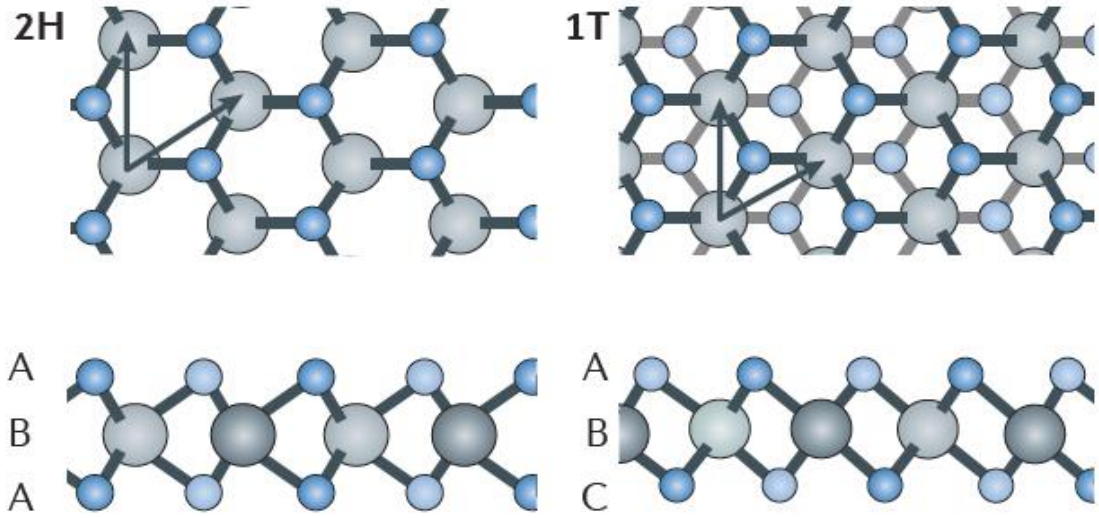

Figure 2- 6 Atomic structure of single layers of transition metal dichalcogenides (TMDCs) in their trigonal prismatic (2H) and octahedral (1T) [34].

2.3.1 Band Structure of WS_2

The 2H phase of Tungsten disulphide (WS_2) displays semiconducting behaviour, whereas the 1T phase is metallic. The unit cell is composed of $S - W - S$ and extends over two layers. The lattice constants as given by Schutte et al. are a=3.191 Å and z= 3.144 Å[39].

Multilayers of WS_2 have an indirect band gap but this becomes a direct band gap in monolayers, as shown in **Figure(2-7)**[40]. In multilayer WS_2 the valence band maximum (VBM) is located at the Γ-point and the conduction band minimum (CBM) is located at the K- point. However, the VBM and CBM of a monolayer are both located at the K point of the Brillouin zone, analogous to monolayer graphene. Thus, charge carriers (electrons and holes) gain an additional valley degree of freedom, which may be used for information encoding and processing[41, 42, 43, 44]. The fundamental band gap is defined by an electronic transition between the Γ- and K-point while the optical direct band gap is situated at the K-point.

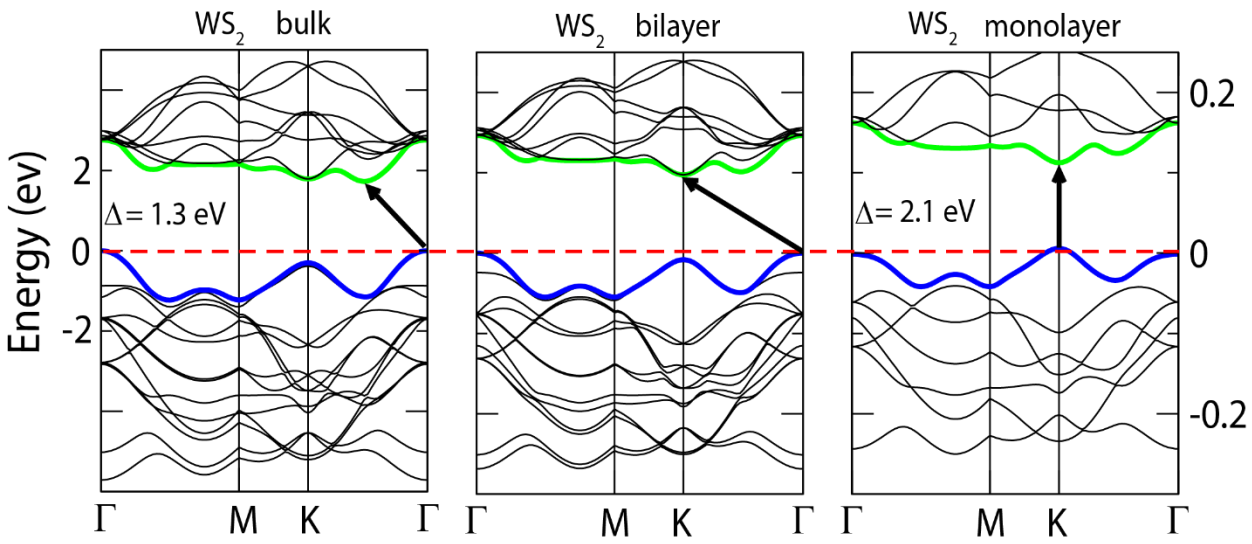

Figure 2- 7 Band structure of WS2 Bulk, Bilayer and monolayer. The horizontal dashed lines indicate the Fermi level. The arrows indicate the bandgap (direct or indirect). The top green line and bottom blue line represent the minimum of valence band and maximum of the conduction band, sequence[37].

The electronic structure of WS_2 originates from mostly transition metal (W) d-electron orbitals because Tungsten has 4-valance-electrons whilst the p-electron orbital (6 electrons) of the chalcogen (S) has a weak contribution. The two orbitals (d and p_z), hybridise generating d_{xy}, d_{xz}, d_{yz}, $d_{x^2-y^2}$ and d_{z^2} orbitals. In this case the d_{xy}, $d_{x^2-y^2}$ and d_{z^2} orbitals are the dominant components for the conduction and valance bands[40, 45, 46, 47].

2.4 Magneto-Resistance (MR)

The classical equation of motion for charge carriers in the presence of an electric field (E) and magnetic field (H) is

$$m\dot{\vec{v}} = -q\left(\vec{E} + \frac{\vec{v}}{c} \times \vec{H} + \frac{m^*}{\tau}\vec{v}\right) \qquad (2-10)$$

In 2D $\vec{E}$ $(E_x, E_y, 0)$, In stationary conditions $\dot{v} = 0$ and we have $\mu = \frac{q\tau}{m^*}$, $J = -ne\vec{v}$ Substituting these terms into equation (2-10), the conductivity in the x-y plane of a 2D material can be expressed as

$$\sigma_{xx} = \frac{\sigma_o}{1 + (\mu H)^2} = \frac{en\mu}{1 + (\mu H)^2} \qquad (2 - 11a)$$

$$\sigma_{yx} = \frac{\mu B \sigma_o}{1 + (\mu H)^2} = \frac{eBn\mu^2}{1 + (\mu H)^2} \qquad (2 - 11b)$$

Under a magnetic field, the current in the y-direction will not be zero due to the Lorentz force. Therefore, the backflow of carriers, propagating along the negative *x*-direction, will act to change the apparent resistivity $\sigma_{xx} = J_x/E_x$, i.e. cause magnetoresistance (MR).

MR is defined as an increase (positive) or decrease (negative) in the electrical resistance of a material in the presence of a change in magnetic field:

$MR(\%) = \frac{R(H) - R(0)}{R(0)} * 100$.

In general, MR can be categorized in three classes.

1- The resistance of a material saturates at a certain field (H) and it has a quadratic dependence at low values of external magnetic field. Most of the materials in this category have a closed Fermi surface (e.g. In, Al, Na and Li).
2- Magnetoresistance which saturates at a given magnetic field threshold in one crystal orientation but does not saturate in a different crystal orientation. This known as the extraordinary anisotropy magnetoresistance. Most of the materials in this category have an open Fermi surface (e.g. Cu, Ag, Pb and Pt).

3- Magnetoresistance which continues to increase linearly up to the highest measurable magnetic field. This is called non-saturating Linear Magnetoresistance (LMR). It is observed in zero or near-zero bandgap materials with fluctuations in mobility and in parallel gases.

In the case of quadratic dependence, the fractional change in resistance is defined as

$$\frac{\Delta R}{R(0)} \alpha \begin{cases} (\mu H)^2, & \mu H < 1 \\ C, & \mu H > 1 \end{cases}$$

Whilst in the case of linear dependence,

$$\frac{\Delta R}{R(0)} \alpha \{H\}$$

Figure (2-8) display the behaviour of these both cases

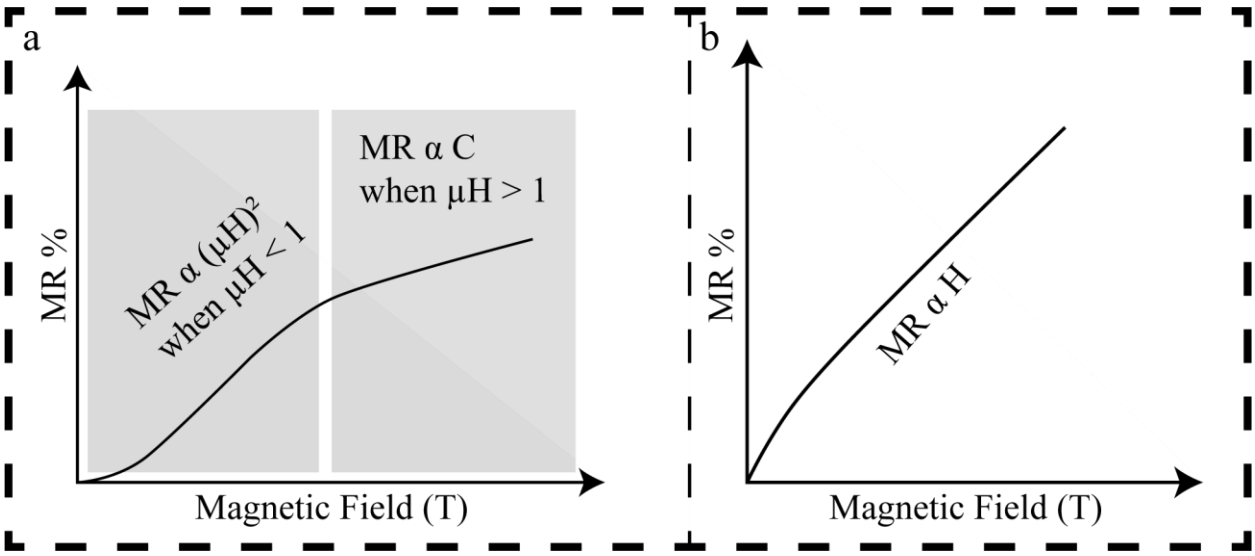

Figure 2- 8 Magnetoresistance behaviour **a-** quadratic dependence. **b-** linear dependence

Magnetic field sensors are typically employed in information storage applications, such as the read head of hard disk drives. Over the last few decades, much work has been directed at finding new materials in which MR has a linear dependence on the magnetic field strength. However, the majority of these MR devices can only operate at low temperatures, hampering their incorporation in electronic devices. This limitation arises from the low mobility of charge carriers in these materials at room temperature. This thesis presents original experimental studies of Linear Magnetoresistance (LMR) in graphene structures.

2.4.1 LMR originating from inhomogeneity

The first observation of LMR was reported in doped silver chalcogenides [48] and it was quickly followed by a fast-growing number of experiments revealing non-saturating LMR in a variety of systems including Dirac[49] and Weyl[50] semimetals, multilayer graphene[51, 52], topological insulators[53, 54], and narrow-gap semiconductors[55]. Positive LMR is a ubiquitous effect in zero and near-zero bandgap materials with non-negligible granularity/inhomogeneity. Depending on the balance of these two features, several appropriate theories have been established. Among those theories, the Parish and Littlewood (PL) model[56] has proven to be widely applicable. It represents the material as an interconnected conductive system, where each sub-micron system has its own mobility, as shown in **Figure (2-9a)**.

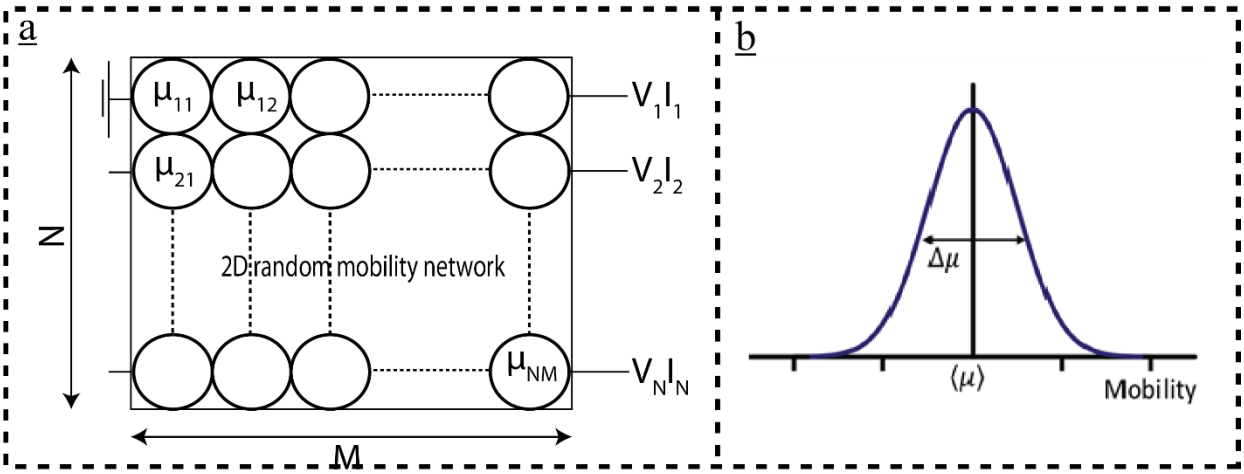

Figure 2- 9 2D random mobility network **a-** The $N \times M$ mobility network has voltage V_i and current I_i associated with the ith input terminal. **b-** Gaussian distribution for the mobility in random mobility network.

In this model the mobility is taken to be a Gaussian distribution, where $\Delta\mu$ and $\langle\mu\rangle$ are the width (variance) and the average of mobility, as shown in **Figure (2-9b)**. The mean is dependent upon the effective mobility rather than the mobility itself.

The simulation of the current paths for large random networks under high magnetic field describes the physical mechanism behind the LMR in inhomogeneous materials, see **Figure (2-10)**. The simulation shows us that the majority of current paths follow the voltage drop. Also, it can be noticed that non-trivial current paths are perpendicular to the external applied voltage. This behaviour makes the Hall current non-zero and has implications on the longitudinal voltage, i.e. $R_h \alpha H$.

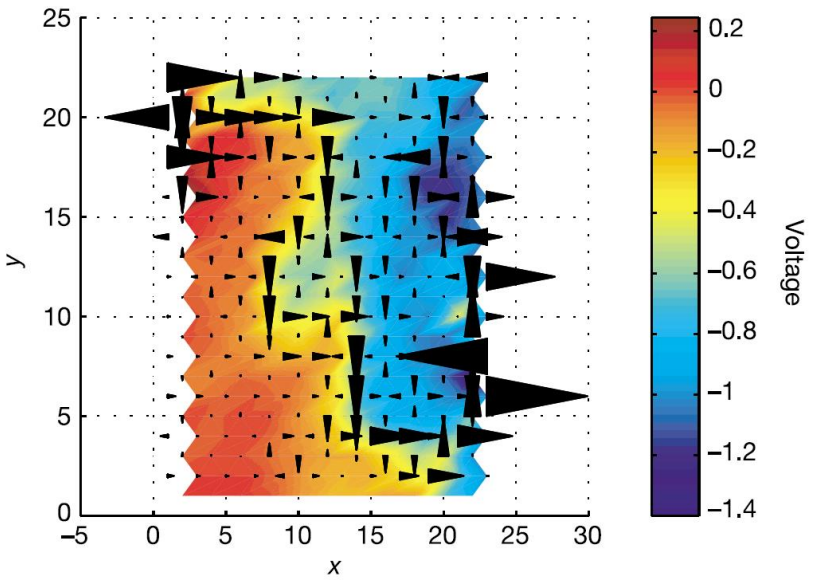

Figure 2- 10 Current paths and voltage simulation for large random network under high magnetic field.

As the size of the network increases, ΔR becomes proportional to H ($\Delta R \; \alpha \; H$). At sufficiently large magnetic fields:

$$\frac{\Delta R(H)}{R(0)} \propto \langle \mu \rangle \qquad for \frac{\Delta \mu}{\langle \mu \rangle} < 1$$

$$\frac{\Delta R(H)}{R(0)} \propto \Delta \mu \qquad for \frac{\Delta \mu}{\langle \mu \rangle} > 1$$

In order to probe this model, a material with high inhomogeneity and/or high effective mobility are required to get high LMR. In chapter 3 the potential of graphene films with bubbles for LMR is discussed.

2.4.2 LMR originating from Parallel gases

Another classical physical model has been found to address the linear magnetoresistance observed in 2D materials. In this model, the magnitude of magnetoresistance is dependent upon the difference in efficiency of charge transport within two parallel electron gases. Here, we assume that both electron gases are

exposed to the same magnetic (B) and longitudinal electric (E) fields. Employing the Drude model, the electrical conductivity of the system can be expressed as shown in equation (2-11a and 2-11b). The current density in a 2D material takes the form

$$J_x = \sigma_{xx}E_x + \sigma_{xy}E_y \qquad (2-12)$$

$$J_y = -\sigma_{xy}E_x + \sigma_{xx}E_y$$

Where J_y is zero because the current is flowing in the x-direction, therefore:

$$E_y = \frac{\sigma_{xy}}{\sigma_{xx}}E_x \text{ or } E_x = \frac{\sigma_{xx}}{\sigma_{xy}}E_y\,. \qquad (2-13)$$

By substituting equation (2-13) into equation (2-12), we find expressions for the resistivity parallel and perpendicular to the direction of current flow:

$$\rho_{xx} = \rho_{yy} = \frac{\sigma_{xx}}{\sigma_{xx}^2 + \sigma_{xy}^2} \qquad (2-14a)$$

$$\rho_{xy} = -\rho_{yx} = \frac{\sigma_{xy}}{\sigma_{xx}^2 + \sigma_{xy}^2} \qquad (2-14b)$$

In the case where two conductors are connected in parallel, the total current flowing in the system is $J = j_1 + j_2 = (\rho_1 + \rho_2)E$. Hence, the total resistivity will be $\rho = \rho_1 + \rho_2$.

By substituting equation (2-11a and b) into equation (2-14a and b), the longitudinal and transverse resistivity can be expressed as a function of the mobility and density of charge carriers in each parallel gas:

$$\rho_{xx} = \frac{\frac{n_1\mu_1}{1+(B\mu_1)^2} + \frac{n_2\mu_2}{1+(B\mu_2)^2}}{\left(\frac{n_1\mu_1}{1+(B\mu_1)^2} + \frac{n_2\mu_2}{1+(B\mu_2)^2}\right)^2 + B^2\left(\frac{n_1{\mu_1}^2}{1+(B\mu_1)^2} + \frac{n_2{\mu_2}^2}{1+(B\mu_2)^2}\right)^2}$$

$$\rho_{xy} = B\frac{\frac{n_1{\mu_1}^2}{1+(B\mu_1)^2}+\frac{n_2{\mu_2}^2}{1+(B\mu_2)^2}}{\left(\frac{n_1\mu_1}{1+(B\mu_1)^2}+\frac{n_2\mu_2}{1+(B\mu_2)^2}\right)^2+B^2\left(\frac{n_1{\mu_1}^2}{1+(B\mu_1)^2}+\frac{n_2{\mu_2}^2}{1+(B\mu_2)^2}\right)^2}$$

In the case where B=0 the expression for the longitudinal magnetoresistance reduces to

$$\rho_{xx,0} = \frac{1}{e(n_1\mu_1 + n_2\mu_2)}$$

In contrast, it can be shown that for B >>μ_1^{-1}, μ_2^{-1} the longitudinal magnetoresistance is

$$\rho_{xx,\infty} = \frac{n_1\mu_2 + n_2\mu_1}{e\mu_1\mu_2(n_1+n_2)}$$

For the limiting case of an infinite MR, the expression will be:

$$MR_\infty = \frac{\rho_{xx,\infty}-\rho_{xx,0}}{\rho_{xx,0}} = \frac{n_1n_2}{(n_1+n_2)^2}\frac{(\mu_1-\mu_2)^2}{\mu_1\mu_2} \qquad (2-15)$$

which can simplified using the approximation (1-15) to find $\mu_1 >> \mu_2$

resulting in $MR_\infty = \frac{n_1n_2}{(n_1+n_2)^2}\ \frac{\mu_1}{\mu_2}$.

2.5 Light Detection

Light detection is the process of converting optical signals into electrical signals using devices such as photodetectors (PDs) and solar cells. On the other hand, devices such as light-emitting diodes (LEDs) can be used to convert electrical signals

to light. This thesis will focus on PDs only. When a PD absorbs light, electrons in the valence band are excited into the conduction band, and their absence in the valence band creates positive charge carriers known as holes. A goal of PD design is to efficiently separate and extract these charges out of the PD so that they can become a measurable electrical current/voltage.

2.5.1 Figures of merit for photodetector devices (PDs)

The electrical response of a photodetector to incident light can be measured in terms of a change in potential difference, electrical current or resistance throughout the active material. Typically, the active material is a semiconductor and the energy of the incident light should be higher than its energy band gap ($E_{ph} > E_{bg}$). To judge the quality of a photodetector device, some general figures of merit should be considered.

Responsivity

This describes the sensitivity of a photodetector to the incident light. It is the ratio of generated current or voltage to the incident light power at a given wavelength, following the phenomenological formula:

$$R(\lambda) = \frac{I_{ph}}{P(\lambda)_{light}\, A}\ (A/W) \quad \text{or} \quad \frac{V_{ph}}{P(\lambda)_{light}} \quad (V/W)$$

where I_{ph} is the photocurrent, P is the incident optical power, A is the area of the `photo-active' light-absorbing region of the photodetector and V_{ph} is the photovoltage.

In other words, it is a measure of the efficiency of the conversion of the light power into electrical current. It varies with the wavelength of the incident light as well as applied reverse bias and temperature[57, 58].

External Quantum Efficiency ($\boldsymbol{\eta_{EQE}}$)

The external quantum efficiency of a photodetector device describes the fraction of incident photons that contribute to photocurrent signal:

$$\eta_{EQE}(\lambda) = \frac{n_e}{n_{photon}^{total}} = \mathrm{R}(\lambda)\frac{hv}{q}$$

Where $\boldsymbol{\eta_{eqe}}$ is less than one except when there is an internal amplification mechanism, such as photo-conductive gain[57, 58]. It defines the number of electrons or holes, with charge q , extracted as photocurrent per incident photon of energy hv.

Internal Quantum Efficiency ($\boldsymbol{\eta_{IQE}}$)

This is the fraction of absorbed photons that are converted to photocurrent and it is given by

$$\eta_{IQE}(\lambda) = \frac{\eta_{EQE}(\lambda)}{A_{abs}(\lambda)}$$

Noise Equivalent Power (NEP)

The noise equivalent power is the minimum power of incident light that the photodetector can sense. The extracted photocurrent (I_{pc}) will equal the noise level of the device (I_n)[57, 58] as described by the relation

$$NEP = \frac{P_{min} I_{pc}}{I_n \sqrt{BW}} \quad (W/\sqrt{Hz})$$

Where BW is the measured bandwidth.

Specific Detectivity D^*

It is the figure of merit that is a measure of the device sensitivity which takes into account the device area. It is given by

$$D^* = \frac{\sqrt{A}}{NEP} \ (cm\sqrt{Hz}\ /W)\ (Jones)$$

where A is the active area of the photodetector. The specific detectivity allows the direct comparison between photodetectors having different geometries[57, 58].

2.5.2 Photocurrent generation mechanisms in 2D

The photocurrent is defined as the difference between the current measured in a device upon illumination and dark condition $(I_{ph} = I_{D,ilum} - I_{D,dark})$. A variety of physical mechanisms can act simultaneously in 2D materials to generate a finite photocurrent. Some of them are driven by electric field separation, for example photoconductivity (PC), and the photovoltaic (PV) effect. Others depend on temperature gradients, such as photo-thermoelectric effect (PTE) and the bolometric effect. The latter effects are prevalent in graphene. In the following, each effect is introduced.

2.5.2.1 Electric field dependent photocurrent mechanisms

A built-in potential can be generated at the interface of two materials with different work functions. Such an interface can be planar or vertical such as the case for stacked van der Waals heterostructures. Planar electric fields can be formed in many ways, for example by an externally applied voltage between source and drain electrodes, gate-induced PN junctions, Schottky barrier at semiconductor-semiconductor or semiconductor-metal interfaces. Whilst the vertical electric field generate when the device architecture is hybrid vertical structure.

Photocurrent generation by local electric fields internal to the device is referred to as the photovoltaic effect (PV). However, photocurrent driven by an externally applied electric field is referred to as Photoconductivity (PC).

In the work presented in this thesis, the main photocurrent mechanism is the charge transfer of photogenerated carriers driven by a built-in electric field at a heterointerface between a layered semiconductor and graphene, see **Figure (2-11)**. In this case, the semiconducting material converts photons to charges whilst the gapless semimetallic graphene is used for the efficient extraction and recirculation of one type of photogenerated carriers. When photons with energy $hv > E_g$, where E_g in the bandgap of the semiconductor, are shone onto the structure, electron-hole pairs are generated in the semiconductor. Depending on the specific choice of materials and their work functions, one charge carrier type can transit across the graphene-semiconductor interface driven by a built-in field. The other charge carrier remains trapped in the semiconductor. Owing to the high charge carrier mobility, it is possible to recirculate the charge carriers many times in graphene before the other carrier type left in the semiconductor relaxes. This leads to an intrinsic gain mechanism. With an external electric field applied perpendicular to the van der Waals heterostructure, it is possible to tune the built-in electric field. This results in a tuneable photo-gating effect. Naturally, the recirculation of charges in the graphene channel requires the application of a finite bias voltage between source and drain electrodes.

The gain mechanism can be quantified by considering the ratio of the trapped carrier lifetime τ_{lt} to the transit time τ_{tr} of the charges in graphene. The gain is defined by.

$$G = \tau_{lt}/\tau_{tr}$$

The transit time is also known as dwell time and it is the time span a free carrier needs to move from one electrode to the other. This is defined as

$$\tau_{tr} = L^2/\mu V$$

where μ is the mobility, L is the channel length and V is the applied drain source bias.

For example, if holes are left in the semiconductor and electrons are recirculated in high mobility graphene, a gain is produced until the holes relax through recombination. In this case the lifetime of electrons is governed by the trapping time of the holes.

Since one type of the photogenerated carriers is trapped and they have a certain spatial distribution, they can produce an additional electric field, effectively acting as a local gate voltage (ΔV_g) to modulate the conductance of the neighbouring graphene channel ($\Delta\sigma$).

$$\Delta\sigma = \Delta nq\mu$$

Where Δn the change in the charge carriers density, μ charge carrier mobility.

The number of traps and their corresponding capture cross section for each carrier type vary for each material and depend on factors such as defects, impurities or surface states. This gain mechanism is limited by the recombination lifetime of the localized trap states and the mobility of the channel. If the charge carrier dynamics can be tailored such that the $\tau_{lt} > \tau_{tr}$, graphene can be engineered into an amplified photodetector. Therefore, photogating has drawn attention by a wide community of researchers.

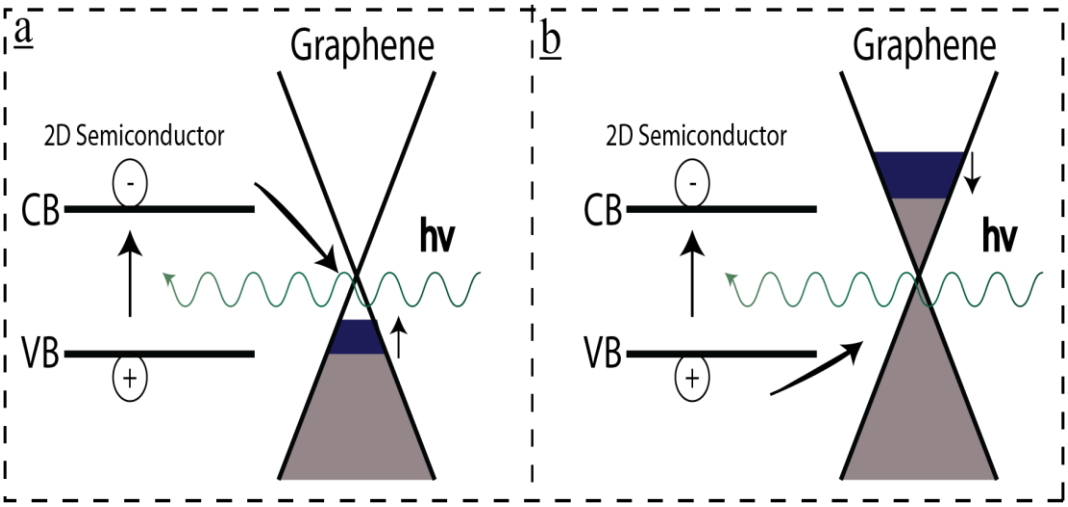

Figure 2- 11 Schematic diagrams of hybrid photogating **a-** Photocurrent is negative**. b-** Photocurrent is positive.

2.5.2.2 Temperature-dependent photocurrent mechanisms

In this mechanism, the incoming photons change the local temperature of the free electron gas leading to a temperature gradient in a material ΔT which is converted to a voltage difference ΔV via the Seebeck effect:

$$S = -\frac{\Delta V}{\Delta T},$$

where S is the Seebeck coefficient (thermoelectric power), ΔT is proportional to the electron temperature difference between the area of optical excitation and its surroundings. In fact, photogenerated carriers will have a temperature which depends on the microscopic dynamic of the specific material.

The Seebeck coefficient is given by the Mott relation[59, 60]:

$$S = \frac{\pi^2 k_B^2 T_h}{3q} \frac{1}{R} \frac{dR}{dV_g} \frac{dV_g}{dE} |_{E=E_F}$$

Where T_h is the temperature for hot charge carriers

For graphene, $\frac{dV_g}{dE}$ is evaluated at the Fermi energy which is $E_f = \hbar v_f (\pi n)^{1/2}$.

The thermoelectric current can be expressed as[61]:

$$I_{TE} \propto S * \Delta T_h$$

The electrodes need to form ohmic contacts to drive the current through the device for this mechanism.

Another mechanism which is dependent upon temperature is the bolometric effect. In this case, the conductivity (resistance) will change by heating associated with the incident photons. The sensitivity in this mechanism is related to the thermal resistance $R_h = dT/dP$ and the heat capacity C_h, which determines its response time $\tau = R_h C_h$[62].

References

1. Wallace P. The Band Theory of Graphite. *Physical Review* 1947, **71**(9)**:** 622-634.

2. Atkins PW, De Paula J, Walters V. *Physical Chemistry*. Macmillan Higher Education, 2006.

3. Craciun MF. Alkali-doped metal-phthalocyanine and pentacene compounds. PhD thesis, TUDelft, 2006.

4. Grosso G, Parravicini GP. *Solid State Physics*. Elsevier Science, 2013.

5. McCann E, Abergel DSL, Fal'ko VI. Electrons in bilayer graphene. *Solid State Commun* 2007, **143**(1)**:** 110-115.

6. Katsnelson MI, Katsnel′son MI. *Graphene: Carbon in Two Dimensions*. Cambridge University Press, 2012.

7. Shon NH, Ando T. Quantum Transport in Two-Dimensional Graphite System. *Journal of the Physical Society of Japan* 1998, **67**(7)**:** 2421-2429.

8. Du X, Skachko I, Barker A, Andrei EY. Approaching ballistic transport in suspended graphene. *Nat Nano* 2008, **3**(8)**:** 491-495.

9. Bolotin KI, Sikes KJ, Jiang Z, Klima M, Fudenberg G, Hone J, *et al*. Ultrahigh electron mobility in suspended graphene. *Solid State Commun* 2008, **146**(9-10)**:** 351-355.

10. Ando T. Screening Effect and Impurity Scattering in Monolayer Graphene. *Journal of the Physical Society of Japan* 2006, **75**(7)**:** 074716.

11. Adam S, Hwang EH, Galitski VM, Das Sarma S. A self-consistent theory for graphene transport. *Proceedings of the National Academy of Sciences* 2007, **104**(47)**:** 18392-18397.

12. Galitski VM, Adam S, Das Sarma S. Statistics of random voltage fluctuations and the low-density residual conductivity of graphene. *Physical Review B* 2007, **76**(24)**:** 245405.

13. Pereira VM, Nilsson J, Castro Neto AH. Coulomb Impurity Problem in Graphene. *Physical Review Letters* 2007, **99**(16)**:** 166802.

14. Adam S, Hwang EH, Das Sarma S. Scattering mechanisms and Boltzmann transport in graphene. *Physica E: Low-dimensional Systems and Nanostructures* 2008, **40**(5)**:** 1022-1025.

15. Chen J-H, Jang C, Xiao S, Ishigami M, Fuhrer MS. Intrinsic and extrinsic performance limits of graphene devices on SiO2. *Nat Nano* 2008, **3**(4)**:** 206-209.

16. Mariani E, von Oppen F. Flexural Phonons in Free-Standing Graphene. *Physical Review Letters* 2008, **100**(7)**:** 076801.

17. Castro EV, Ochoa H, Katsnelson MI, Gorbachev RV, Elias DC, Novoselov KS, *et al.* Limits on Charge Carrier Mobility in Suspended Graphene due to Flexural Phonons. *Physical Review Letters* 2010, **105**(26)**:** 266601.

18. Fratini S, Guinea F. Substrate-limited electron dynamics in graphene. *Physical Review B* 2008, **77**(19)**:** 195415.

19. Hwang EH, Das Sarma S. Acoustic phonon scattering limited carrier mobility in two-dimensional extrinsic graphene. *Physical Review B* 2008, **77**(11)**:** 115449.

20. Cheianov VV, Fal'ko VI. Selective transmission of Dirac electrons and ballistic magnetoresistance of $n\text{-}p$ junctions in graphene. *Physical Review B* 2006, **74**(4)**:** 041403.

21. Novoselov KS, Geim AK, Morozov SV, Jiang D, Zhang Y, Dubonos SV, *et al.* Electric Field Effect in Atomically Thin Carbon Films. *Science* 2004, **306**(5696)**:** 666-669.

22. Hwang EH, Das Sarma S. Graphene magnetoresistance in a parallel magnetic field: Spin polarization effect. *Physical Review B* 2009, **80**(7)**:** 075417.

23. Hwang EH, Adam S, Sarma SD. Carrier Transport in Two-Dimensional Graphene Layers. *Physical Review Letters* 2007, **98**(18)**:** 186806.

24. Zhu W, Perebeinos V, Freitag M, Avouris P. Carrier scattering, mobilities, and electrostatic potential in monolayer, bilayer, and trilayer graphene. *Physical Review B* 2009, **80**(23)**:** 235402.

25. Ferry DK, Goodnick SM, Bird J. *Transport in Nanostructures*. Cambridge University Press, 2009.

26. Ohta T, Bostwick A, McChesney JL, Seyller T, Horn K, Rotenberg E. Interlayer Interaction and Electronic Screening in Multilayer Graphene Investigated with Angle-Resolved Photoemission Spectroscopy. *Physical Review Letters* 2007, **98**(20)**:** 206802.

27. Guinea F. Charge distribution and screening in layered graphene systems. *Physical Review B* 2007, **75**(23)**:** 235433.

28. Dean CR, Young AF, MericI, LeeC, WangL, SorgenfreiS, *et al*. Boron nitride substrates for high-quality graphene electronics. *Nat Nano* 2010, **5**(10)**:** 722-726.

29. Banszerus L, Schmitz M, Engels S, Goldsche M, Watanabe K, Taniguchi T, *et al*. Ballistic Transport Exceeding 28 μm in CVD Grown Graphene. *Nano Letters* 2016, **16**(2)**:** 1387-1391.

30. Banszerus L, Schmitz M, Engels S, Dauber J, Oellers M, Haupt F, *et al*. Ultrahigh-mobility graphene devices from chemical vapor deposition on reusable copper. *Science Advances* 2015, **1**(6).

31. Malard LM, Pimenta MA, Dresselhaus G, Dresselhaus MS. Raman spectroscopy in graphene. *Physics Reports* 2009, **473**(5–6)**:** 51-87.

32. Ferrari AC, Basko DM. Raman spectroscopy as a versatile tool for studying the properties of graphene. *Nat Nano* 2013, **8**(4)**:** 235-246.

33. Saito R, Hofmann M, Dresselhaus G, Jorio A, Dresselhaus MS. Raman spectroscopy of graphene and carbon nanotubes. *Advances in Physics* 2011, **60**(3)**:** 413-550.

34. Manzeli S, Ovchinnikov D, Pasquier D, Yazyev OV, Kis A. 2D transition metal dichalcogenides. 2017, **2:** 17033.

35. Toh RJ, Sofer Z, Luxa J, Sedmidubsky D, Pumera M. 3R phase of MoS2 and WS2 outperforms the corresponding 2H phase for hydrogen evolution. *Chemical Communications* 2017, **53**(21)**:** 3054-3057.

36. Schutte WJ, De Boer JL, Jellinek F. Crystal structures of tungsten disulfide and diselenide. *Journal of Solid State Chemistry* 1987, **70**(2)**:** 207-209.

37. Kuc A, Zibouche N, Heine T. Influence of quantum confinement on the electronic structure of the transition metal sulfide TS${}_{2}$. *Physical Review B* 2011, **83**(24)**:** 245213.

38. Rycerz A, Tworzyd o J, Beenakker C. Valley filter and valley valve in graphene. *Nature Physics* 2007, **3**(3)**:** 172-175.

39. Xiao D, Yao W, Niu Q. Valley-Contrasting Physics in Graphene: Magnetic Moment and Topological Transport. *Physical Review Letters* 2007, **99**(23)**:** 236809.

40. Zhang YJ, Yoshida M, Suzuki R, Iwasa Y. 2D crystals of transition metal dichalcogenide and their iontronic functionalities. *2D Materials* 2015, **2**(4)**:** 044004.

41. Grosso G. 2D materials: Valley polaritons. *Nat Photon* 2017, **11**(8)**:** 455-456.

42. Klein A, Tiefenbacher S, Eyert V, Pettenkofer C, Jaegermann W. Electronic band structure of single-crystal and single-layer ${\mathrm{WS}}_{2}:$ Influence of interlayer van der Waals interactions. *Physical Review B* 2001, **64**(20)**:** 205416.

43. Yun WS, Han SW, Hong SC, Kim IG, Lee JD. Thickness and strain effects on electronic structures of transition metal dichalcogenides: 2H-$M{X}_{2}$ semiconductors (M $=$ Mo, W; X $=$ S, Se, Te). *Physical Review B* 2012, **85**(3)**:** 033305.

44. Liu G-B, Shan W-Y, Yao Y, Yao W, Xiao D. Three-band tight-binding model for monolayers of group-VIB transition metal dichalcogenides. *Physical Review B* 2013, **88**(8)**:** 085433.

45. Xu R, Husmann A, Rosenbaum TF, Saboungi ML, Enderby JE, Littlewood PB. Large magnetoresistance in non-magnetic silver chalcogenides. *Nature* 1997, **390**(6655)**:** 57-60.

46. Liang T, Gibson Q, Ali MN, Liu M, Cava RJ, Ong NP. Ultrahigh mobility and giant magnetoresistance in the Dirac semimetal Cd3As2. *Nat Mater* 2015, **14**(3)**:** 280-284.

47. Shekhar C, Nayak AK, Sun Y, Schmidt M, Nicklas M, Leermakers I, *et al.* Extremely large magnetoresistance and ultrahigh mobility in the topological Weyl semimetal candidate NbP. *Nat Phys* 2015, **11**(8)**:** 645-649.

48. Gopinadhan K, Shin YJ, Jalil R, Venkatesan T, Geim AK, Neto AHC, *et al.* Extremely large magnetoresistance in few-layer graphene/boron-nitride heterostructures. *Nat Commun* 2015, **6**.

49. Kisslinger F, Ott C, Heide C, Kampert E, Butz B, Spiecker E, *et al.* Linear magnetoresistance in mosaic-like bilayer graphene. *Nat Phys* 2015, **advance online publication**.

50. Assaf BA, Cardinal T, Wei P, Katmis F, Moodera JS, Heiman D. Linear magnetoresistance in topological insulator thin films: Quantum phase coherence effects at high temperatures. *Applied Physics Letters* 2013, **102**(1)**:** 012102.

51. Wang W, Du Y, Xu G, Zhang X, Liu E, Liu Z, *et al.* Large Linear Magnetoresistance and Shubnikov-de Hass Oscillations in Single Crystals of YPdBi Heusler Topological Insulators. *Scientific Reports* 2013, **3:** 2181.

52. Lee M, Rosenbaum TF, Saboungi ML, Schnyders HS. Band-Gap Tuning and Linear Magnetoresistance in the Silver Chalcogenides. *Physical Review Letters* 2002, **88**(6)**:** 066602.

53. Parish MM, Littlewood PB. Non-saturating magnetoresistance in heavily disordered semiconductors. *Nature* 2003, **426**(6963)**:** 162-165.

54. Konstantatos G, Sargent EH. Nanostructured materials for photon detection. *Nature Nanotechnology* 2010, **5:** 391.

55. Buscema M, Island JO, Groenendijk DJ, Blanter SI, Steele GA, van der Zant HSJ, *et al.* Photocurrent generation with two-dimensional van der Waals semiconductors. *Chemical Society Reviews* 2015, **44**(11)**:** 3691-3718.

56. Gabor NM, Song JCW, Ma Q, Nair NL, Taychatanapat T, Watanabe K, *et al.* Hot Carrier–Assisted Intrinsic Photoresponse in Graphene. *Science* 2011, **334**(6056)**:** 648-652.

57. Ashcroft NW, Mermin ND. *Solid State Physics*. Holt, Rinehart and Winston, 1976.

58. Patil V, Capone A, Strauf S, Yang E-H. Improved photoresponse with enhanced photoelectric contribution in fully suspended graphene photodetectors. *Sci Rep* 2013, **3**.

59. Richards PL. Bolometers for infrared and millimeter waves. *Journal of Applied Physics* 1994, **76**(1)**:** 1-24.

Chapter 3

Experimental fabrication and characterisation of material and devices

3.1 Introduction

This chapter presents the key aspects of the fabrication of atomically thin transistor-like structures and the characterisation of the opto-electronic properties. Section (3-2) focuses on the main fabrication steps used for 2D Field Effect transistor (FET). In this section, methods to obtain 2D materials and the production of Van der Waals (VdW) heterostructures by stacking are also discussed. Section (3-3) introduces Raman spectroscopy and its use for the characterization of doping and strain in graphene. Finally, section (3-4) presents the experimental techniques for the characterization of the electrical and opto-electronic properties of transistors with different dielectric environments to include the encapsulation in an ionic polymer gate.

3.2 Fabrication

3.2.1 FET based on 2D materials

In field effect transistors the electrical transport properties of the 2D material are modulated by means of an external electric field. A common experimental implementation of FETs relies on the use of a heavily doped Si substrate, which acts as a back gate, and an oxide dielectric layer of SiO_2, which acts as a gate dielectric (see **Figure (3-1a)).** The band diagrams for n FET for both the equilibrium (without voltage bias applied to the back gate) and non-equilibrium (with a finite voltage bias applied to the back gate) cases are shown in **Figure (3-1b)**.

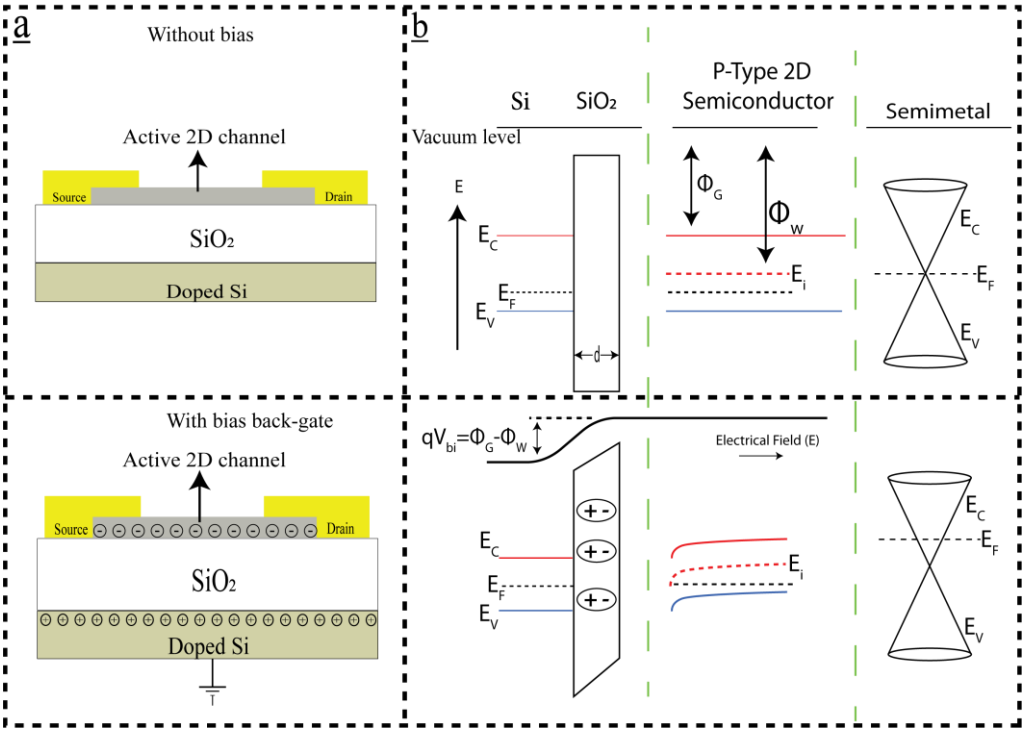

Figure 3- 1 MOS-FET band diagram for semiconductor and semimetal **a-** Device structure with and without bias**. b-** Band diagram for semiconductor and semimetal for equilibrium (without bias) and nonequilibrium (with bias), ϕ_W= work function, ϕ_G= electron affinity, E_i= intrinsic Fermi level**.**

3.2.2 Ultrathin 2D materials

Several techniques have been demonstrated for obtaining mono- and few-layer graphene and other 2D materials. Some of the most widely used methods are mechanical exfoliation, liquid exfoliation, chemical vapour deposition (CVD) and molecular beam epitaxy (MBE). These techniques can be categorised into two main groups: the top-down approach and the bottom-up approach.

Top-down approach

The simplest method for preparation of 2D materials from the bulk is by mechanical exfoliation using scotch tape[25, 63, 64, 65]. This approach takes advantage of the weak

interaction between layers (van der Waals force) and the strong covalent intralayer bonds. A bulk crystal is placed between two pieces of tapes and subsequently exfoliated through several peeling steps. The thin flakes may be transferred to the target substrate (generally SiO2/Si) using gentle pressure.

Bottom-up approach

chemical vapour deposition (CVD) are bottom-up techniques. CVD requires ultrahigh vacuum (UHV) conditions and well-calibrated, high-purity atomic sources which are heated to commence the growth of a material. CVD employs the decomposition or the reaction gas, liquid or solid precursors under a controlled atmosphere to grow 2D materials. In this technique the precursor is present. The precursor evaporates in the reaction chamber and leaves to react with chalcogen elements through vapor-solid reactions under high temperature and vacuum. For CVD, catalytically active substrates are normally utmost effective, and synthesis can be achieved at pressures ranging from atmospheric to UHV. It is worth emphasizing that this method, not only produces ultrathin 2D sheets of high crystal quality, and scalable shape, size and thickness, but also exceptional electronic properties can be achieved, which is extremely important[66, 67, 68].

3.2.3 Van der Waals heterostructure

Atomic layers of a wide range of materials can be assembled into the desired stacking sequence to study a wide range of other physical properties. The interlayer attraction between atomically thin systems is governed by the van der Waal force (vdW). By combining different types of 2D materials to form heterostructures, it is possible to engineer novel electronic and optical properties. A wide range of device functionalities based on heterostructures have been proposed and/or already demonstrated. These include field-effect tunnelling transistors[69, 70, 71], charge trapping memories[71, 72] ,ultrafast photodetectors[73, 74, 75, 76], and 2D light-emitting

diodes (LEDs)[77, 78, 79]. The devices studied in this thesis have been fabricated mainly using a dry transfer process. In this method the first step is the standard mechanical exfoliation of 2D materials on top of a substrate covered by a polymer consisting of polydimethylglutarimide (PMGI) layer under PMMA layer. The bottom PMGI layer is selectively etched with a water based solvent (MICROPOSIT® MF-319) by making a circle around the selected flake. The flake should not be exposed to the solvent to avoid contamination. Following dissolution of the PMGI layer, the top surface of the hydrophobic PMMA film will be floated on top of DI water, by immersing the substrate on it. The floating membrane is then picked up on a metal ring and allowed to dry up. The edge of the ring should be covered by PMMA to make the scooping easy. Then, the ring is loaded upside down into a micromanipulation setup and aligned with a second 2D crystal chosen for the assembly, **Figure (3-2)** illustrates the process.

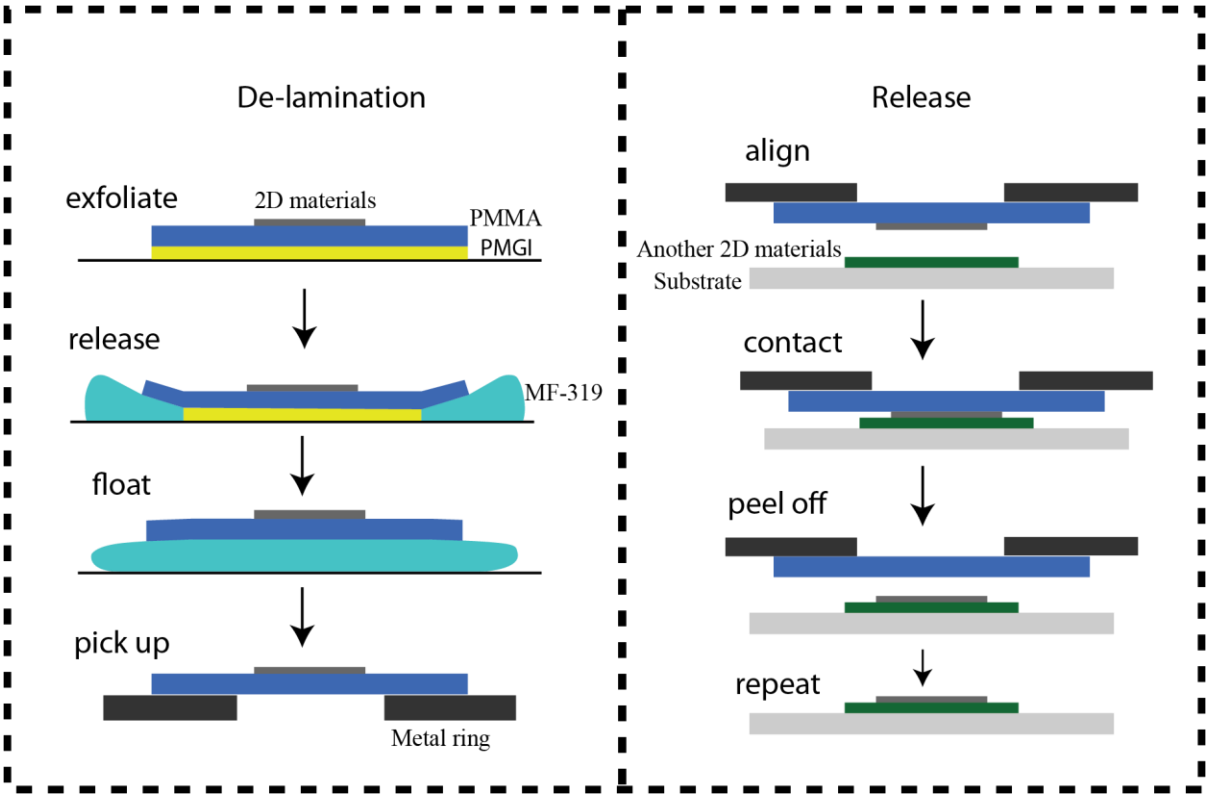

Figure 3- 2 Dry-Peel transfer. The left side showing the process of the de-lamination. The right side showing the process of stacking.

3.2.4 Device fabrication

Specific device geometries and electrical contacts are fabricated using the van der Waals heterostructures. Standard process of electron beam lithography is used to draw nano-scale patterns on a polymer mask spin coating the substrates. For positive resist, the electron beam breaks the bonds of the resist and in the development the exposed PMMA areas are removed. The remaining PMMA then provides a mask for subsequent ion etching of the flake into the desired shape, e.g. Hall bar, or for the deposition of electrical contacts. Finally, the PMMA mask is removed using acetone and IPA.

The deposition of metal thin films takes place in vacuum ($2 * 10^{-6}\ mbar$) with the thermal evaporation of 10nm-thick sticking layer of chromium and 60nm thick gold. The PMMA and excess metal are 'lifted off' using heated acetone overnight to leave just the metal contacts on the flake, **Figure (3-3)**. After this step, the device is left overnight in acetone to remove as much polymer residue as possible. Lastly, the sample is loaded into a chip carrier and wire bonded to allow for electrical measurements to be performed.

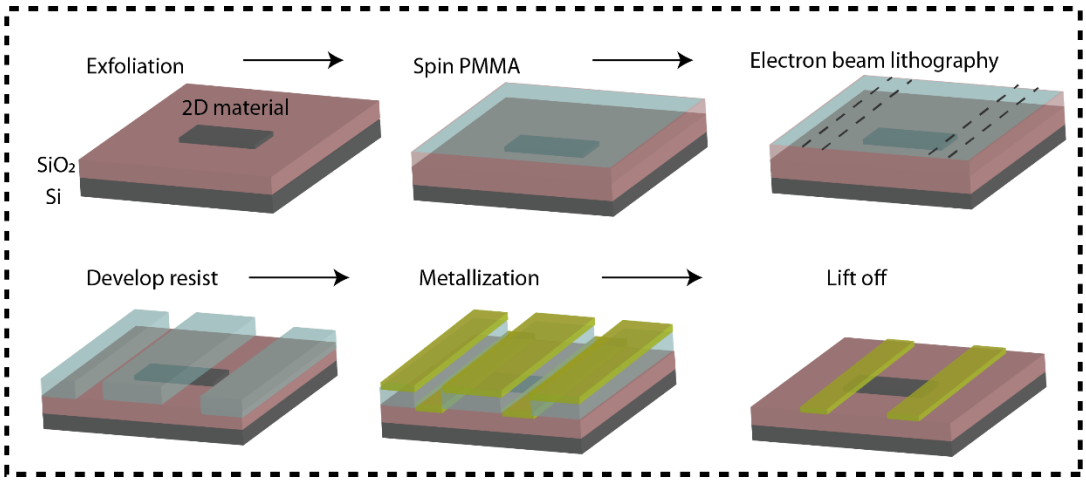

Figure 3- 3 The steps process to fabricate field effect transistor.

3.3 Raman spectroscopy properties of graphene

The fundamental concepts of Raman spectroscopy are outlined in Chapter two. In this section, ways to extract detailed information on doping and strain of graphene from Raman spectroscopy are presented.

3.3.1 Raman spectroscopy of graphene and its relation to doping

The Raman spectrum of graphene has two predominant peaks known as G and 2D whose position in inverse wavelength is strongly influenced by the carrier concentration as demonstrated by several studies[80, 81, 82, 83]. The G peak originates

from a first-order Raman scattering process at the centre of the Brillouin zone (BZ), whereas the 2D peak arises from a second-order double-resonant process between the K and K′ points in the BZ. The G band position reaches a minimum when the Fermi level is at the Dirac point and increase for both electron and hole doping, while the line-width reduces for increasing doping, see **Figure (3-4a)**[84]. The 2D band position also depends on Fermi level and therefore doping. It increases (decreases) as the hole (electron) concentration increases[80].

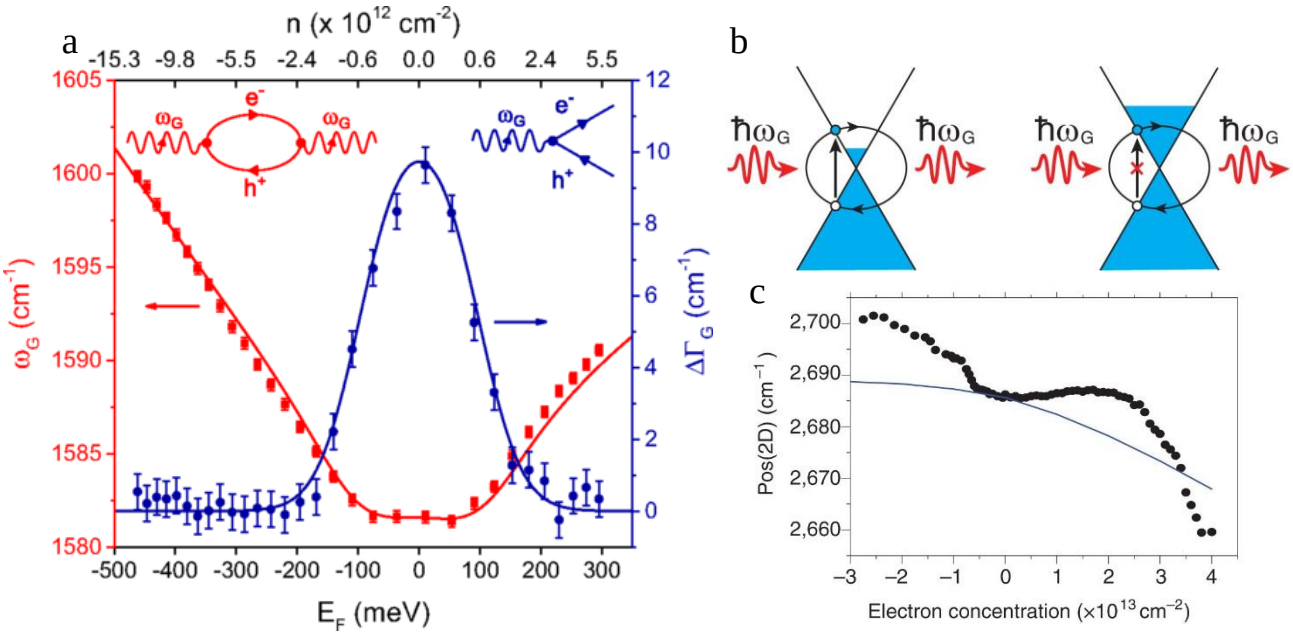

Figure 3- 4 Raman spectrum shows the effect of doping on G and 2D band **a-** G position (red line) and linewidth (blue line) with different doping, the inserts are corresponding Feynman diagram for electron-phonon coupling. The left inset represents the renormalization of the G-mode phonon frequency due to interactions with virtual electron-hole pairs. The right inset represents lifetime broadening due to the resonant decay of a G-mode phonon into an electron-hole pair[36]. **b-** Pauli blocking concept[41], **c-** 2D position with doping[32].

Two effects determine the position of the G band phonons, the adiabatic contribution 'lattice constant expantion'[85, 86] and the nonadiabatic contribution 'Kohn anomaly'[86].

The lattice constant increases (decreases) for electron (hole) doping resulting in a stiffening (softening) of the phonon energy, an adiabatic process. The non-adiabatic process originates that the phonon creates a virtual electron-hole pair that then re-combine and creates another phonon. The new phonon has less energy and lifetime[84, 87, 88]. This interaction is called self-doping, as shown in the left insert in **Figure (3-4a)**[84, 89]. The strength of these interactions depends on the Fermi level[85, 86], which is symmetric with E_F because of the linear dispersion in graphene. By increasing E_F the perturbation of the electrons and phonons will be suppressed.

The reduction of the linewidth of the G-band with doping is also caused by the electron-phonon interaction. However, in this case the phonons decay into electron–hole pairs[86, 90], as shown in right insert in **Figure (3-4a)**[88]. As the charge carrier induce the Fermi level position will change. The allowed energy state by Pauli principle is determined by Fermi level position. By increasing the Fermi level, G band becomes sharper.

The shift in 2D position, unlike the G position comes only from the adiabatic contribution known as 'lattice constant expansion' due to the change in the Fermi energy (E_F), as shown in **Figure (3-4c).**

3.3.2 Raman spectroscopy of graphene and its relation to strain

Strain in graphene can also be probed by Raman spectroscopy since in this material strain can effectively soften the optical-phonon branch[91, 92]. The shift in phonon frequency due to shear (uniaxial) strain is given by [93]:

$$\Delta\omega_{ph}^{s} = \omega_{ph}^{0}\beta_{ph}\varepsilon_{s}$$

where ω_{ph}^{0} is the phonon resonant frequency in the absence of strain, β_{ph} is the deformation potential, ε_s is the shear strain.

If the graphene lattice is subjected to uniaxial strain, the G band will shift and split into two single bands, denoted by G^+ and G^- [94, 95], see **Figure (3-5).** The uniaxial strain breaks the symmetry of graphene, hence the E_{2g} phonon mode splits into two singlet modes that give rise to the G^+ and G^- peaks, respectively[94, 96]. Similar to the G band, the 2D band also splits into two peaks, $2D^+$ and $2D^-$ [94, 96] under homogeneous uniaxial strain[93]. The 2D splitting are found to depend on the direction of the applied strain with respect to the crystallographic orientation. It originates from significant changes in resonant conditions owing to both the distorted Dirac cones and the anisotropic modifications of phonon dispersion under uniaxial strains[97].

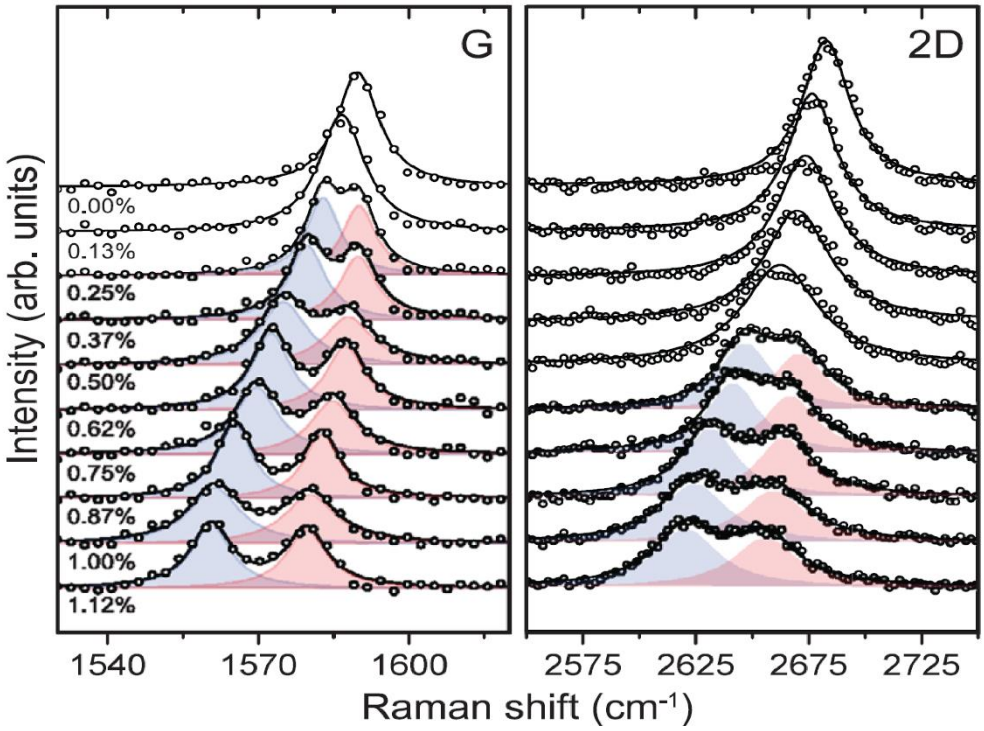

Figure 3- 5 Circular Polarized Raman spectroscopy for Monolayer graphene for G and 2D peaks under uniaxial strain which increases from top to bottom. Fits with one or two Lorentzian peaks are superimposed on the data. G^- and $2D^-$ peaks are coloured blue, G^+ and 2D+ peaks are coloured red [44].

The biaxial strain leads to a shift in the position of the G and 2D peaks, see **Figure (3-6)**[98], given by:

$$\Delta\omega_{ph}^{h} = \omega_{ph}^{0}\gamma_{ph}\varepsilon_{h}$$

where γ_{ph} is the Grueneisen parameter and $\varepsilon_h$is the hydrostatic strain. This strain is responsible of a significant softening of the in-plane phonons because all the in-plane distances are increasing uniformly[91].

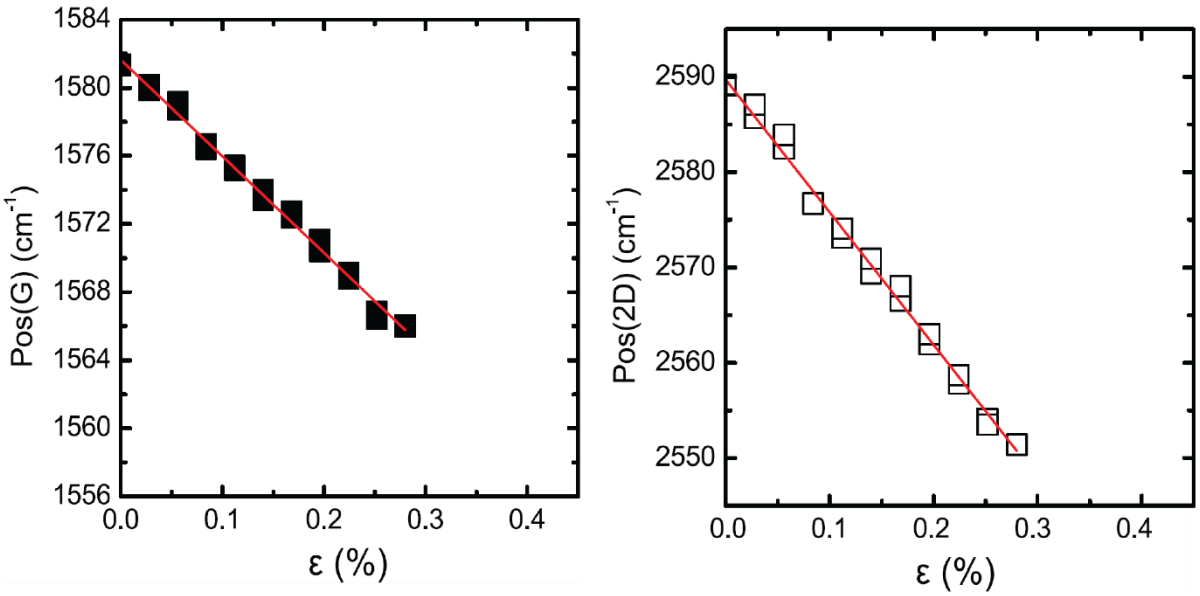

Figure 3- 6 Biaxial strain: the shift of the frequency for the G and 2D peaks with strain[49].

Briefly, shear strain configuration generates an anisotropic distortion of the graphene lattice with keeping the same area of the unit cell as prior to the distortion, while the hydrostatic strain corresponds to an isotropic increase or decrease in the size of the graphene lattice.

Lee et al demonstrated an approach to distinguish the contribution of strain and doping to the shift of ω_G *and* ω_{2D} [99]. However, the drawback of this method is that it cannot be used to determine the amount of strain. Recent experiments have shown that polarized Raman spectroscopy can be used to distinguish between different types of strain[93] as shown in **Figure (3-7)**.

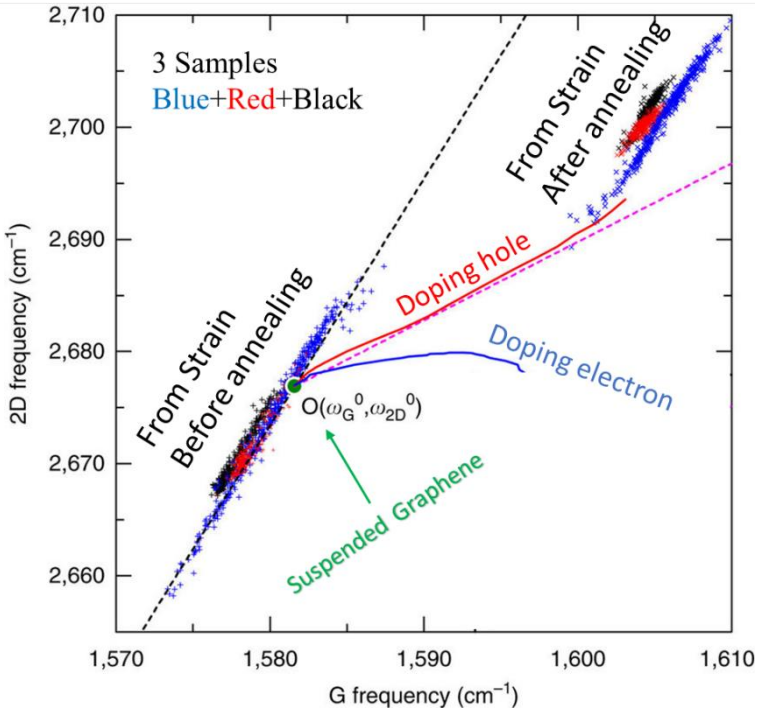

Figure 3- 7 Correlation between G and 2D frequencies shifting to distinguish between strain and doping. If the shifting is due to the strain then it will be linear otherwise it were nonlinear, it would come from doping[50].

3.4 Electrical and Optoelectronic characterization

To assess the quality of the 2D material device, the electrical or optical properties should be measured. Here we use a FET configuration to probe the main electrical properties of the charges in atomically thin materials. To this end, low noise equipment is used such as Lock-in amplifier (DSP 7270) as an AC current source, Keithly 2400 and Xitron 2000 as stable DC source.

3.4.1 Electrical measurement setup

The Fermi level of graphene on Si/SiO2 can be modified by applying perpendicular electrical field through the back gate (Si) which directly modulates the number of charge carriers in the single layer of carbon atoms. The charge carrier concentration

in the conductive channel can be calculated using a simple parallel plates capacitor model:

$$n = \frac{\varepsilon_o \varepsilon_{ox}}{de} V_{BG}$$

Where ε_0 is the vacuum permittivity, V_{BG} is the applied back-gate voltage bias, $d\ and\ \varepsilon_{ox}$ are the thickness and permittivity of SiO_2, respectively.

At the same time, a measurement of the Hall coefficient in a magnetotransport experiment also allows an independent estimate of the charge carrier concentration through the equation

$$n = \frac{I}{e} \frac{dB}{dV_H},$$

where $\varepsilon_o\ and\ \varepsilon_{ox}$ are the permittivities of free space and SiO_2, respectively; e is the electron charge; and d is the thickness of our SiO_2 layer (300 nm), I is the bias current and $\frac{dB}{dV_H}$ is the slope between the magnetic field and the Hall voltage.

Using the Drude model, the charge carrier mobility is given by $\mu = \frac{\sigma}{ne}$, where σ is the conductivity. In an atomically thin system, the conductivity is expressed as $\sigma = L/RW$, where L, W and R are the length, width and resistance between the two voltage probes.

In general, two different electrical circuit configurations for AC and DC current are used to characterise the electrical properties of the devices at zero-frequency and finite albeit low frequency. In the AC characterization an AC constant current is applied to the device to be characterized, see **Figure (3-8 a)**. This is realized using a large resistor i.e. at least two orders of magnitude higher resistance than that of graphene in series to graphene. This is the so-called ballast resistance. An AC voltage source is then connected to the series of the ballast resistor and graphene.

For the DC measurements, a DC voltage source is used to provide constant bias to the device and the current is measured with a multimeter (Agilent 34401A Multimeter), Illustrated in **Figure (3-8b)**.

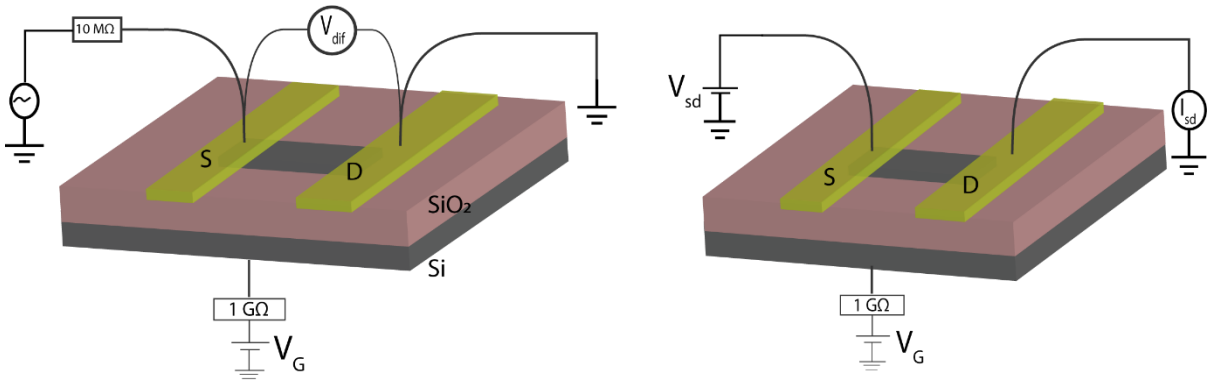

Figure 3- 8 The schematic of the electrical circuit sets up **a-** zero-bias setup or constant current**. b-** constant voltage.

The resistance of graphene can be obtained directly from the lock-in using Kirchhoff's rules. The circuit can be defined as

$$R_{sample} = \frac{V_{A-B} R_{ballast}}{V_{osc}}$$

Where V_{A-B} deferential voltage between A and B probes in lock-in, $R_{ballast}$ ballast resistance and V_{osc} is the applied voltage from the lock-in.

3.4.2 Optoelectronic measurement setup

The optoelectronic measurements presented in this thesis have been acquired using a home developed multifunctional tool built around an upright Olympus BX51 microscope. This system allows for the characterization of low frequency electrical transport, scanning photocurrent microscopy (SPCM), absorption (transmittance and reflectance), micro- Raman and photoluminescence (PL) spectroscopy and mapping, with the possibility to analyse and change the polarization of light.

The system is equipped with Cairn multiline laser bank, spanning from UV to red light and two white light sources used for transmission and reflection characterization. It has the ability to host up to six different wavelengths, with dichroic mirrors and it supports the simultaneous use of different wavelengths. The laser beam passes through a series of kinematic and fixed mirrors as well as focussing lenses before reaching the sample. The motorized microscope stage has a step resolution of 10 nm.

Optical components are selected to keep the fundamental Transverse electromagnetic (TEM_{00}) mode of the used solid-state diode lasers. Each laser module can be digitally modulated, and the output power is adjusted with the laser controller as well as with optical density filters. The system can operate the laser with continuous wave or it can be modulated through the transistor-transistor logic (TTL) of the laser bank controller.

The electrical properties of the devices were taken on a chip carrier which has been purposefully designed to allow for low-noise electrical measurements at low-frequency. This consists of a PCB board. To suppress the noise in the system, the stage is covered by electrically conductive fabric which act as a Faraday cage on the microscope stage. **Figure (3-9)** illustrates a schematic diagram of the system.

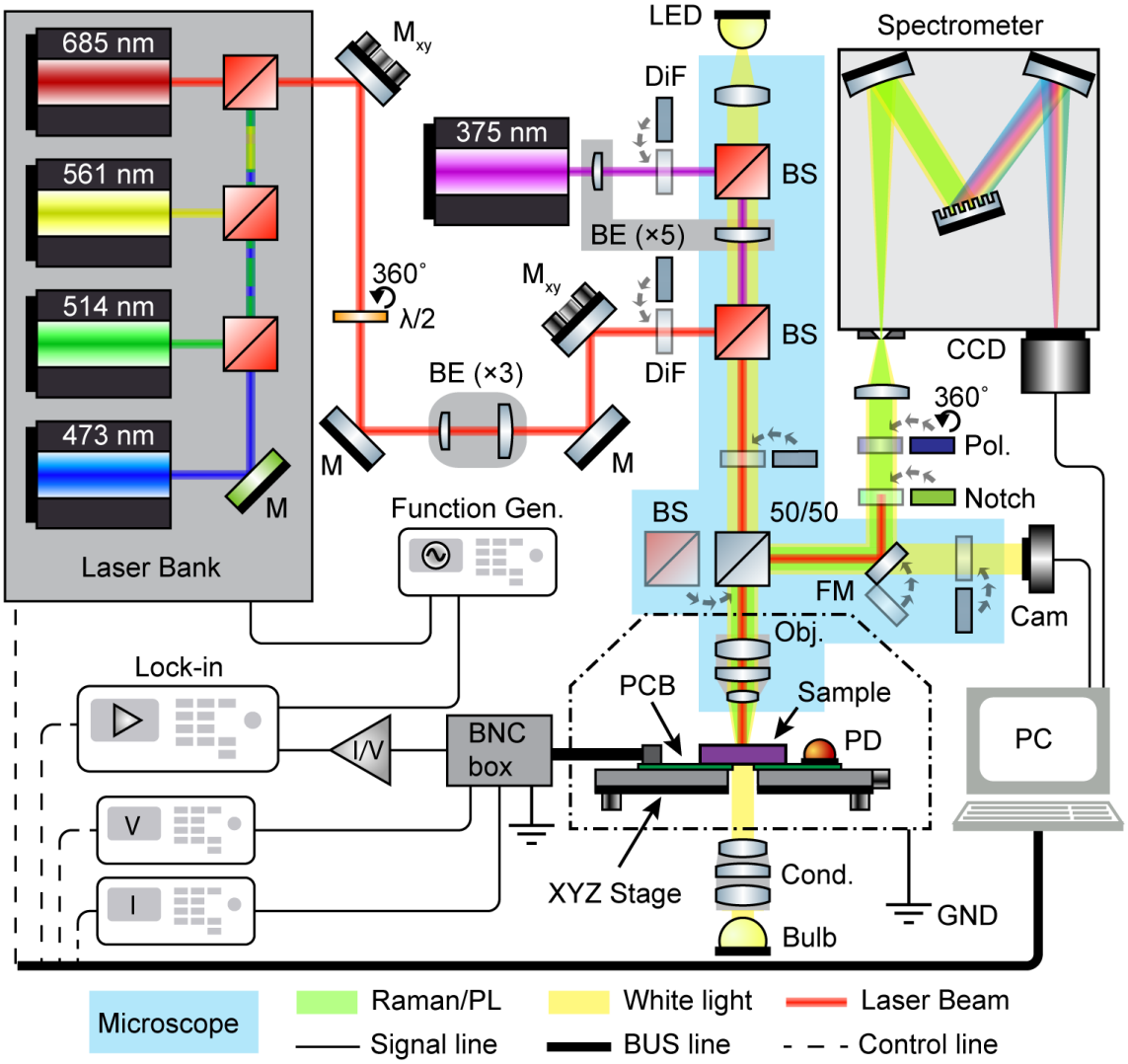

Figure 3- 9 Experimental setup diagram; Laser light is used for scanning photocurrent mapping, Raman and PL spectroscopy. Abbreviations: mirror (M), kinematic mirror (M_{xy}), half-wavelength plate ($\lambda/2$), beam expander (BE, followed by magnification), drop-in filter (DiF), beam splitter (BS, dichroic in red), Polariser/Analyser (Pol.), white light (WL), voltage (V) or current (I) sources/meters, ip mirror (FM), sample holder (PCB), photodetector (PD), condenser (Cond), microscope objective (Obj), imaging camera (Cam), spectroscopy camera (CCD), ground line (GND). Created with Component Library symbols.

3.5 Ionic Gating

A conventional back gate is separated from graphene by a layer of SiO_2 a few hundred nanometres thick, which allows for tuning of the carrier concentration in the range $|n| < 5 \times 10^{13}\ cm^{-2}$ [19, 100]. Solid polymer electrolyte as a top gate is used as an alternative gate, see **Figure (3-10)**. The ions in the electrolyte are free to move under the action of an external applied electric field. More specifically, in ionic liquid gating the coupling between gate electrode and transistor channel is effectively realized through moving ions that form a Debye layer at the interface between 2D materials and the electrolyte, also called electric double layer (EDL). The electric double layer (EDL) formed at liquid/solid (L/S) interfaces, functioning as nanogap capacitors with a huge capacitance, can effectively accumulate or deplete charge carrier over a large range. As a result, the induced carrier density can easily exceed $n_{2D} \approx 10^{14}$ cm^{-2}, more than one order of magnitude larger than that in conventional solid-state field-effect transistors (FETs). Such a strong field effect modulation is valuable for technological applications[101, 102] and it has enabled novel fundamental studies of the physical properties of emerging materials such as graphene[103, 104]. Another advantage of the ionic polymer is their ability to screen charged impurities under or around the active channel[104]. This advantage was exploited to fabricate fast and highly sensitive photodetectors presented in Chapter 6 [76].

The Debye layer of thickness d_{TG} acts like a parallel-plate capacitor. Therefore, the geometrical capacitance in this case is

$$C_{TG} = \varepsilon\varepsilon_o/d_{TG},$$

where ε is the dielectric constant of the PEO matrix. The Debye length is given by

$$d_{TG} = 4\pi ne^2/K_BT$$

where n is the charge carrier concentration and $K_B T$ the thermal energy (= 0.025ev at RT). In the experiments presented in this thesis $n = 10^{14}\ cm^{-2}$ leading to $d_{TG} = 3.5\ nm$.

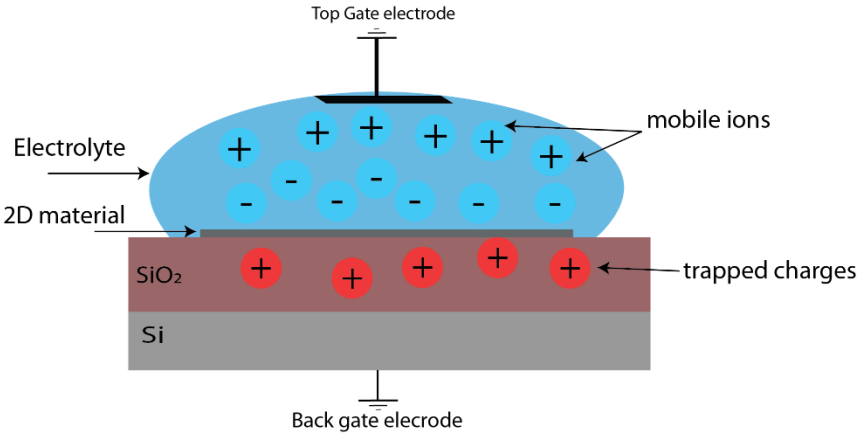

Figure 3- 10 Debye layer for field effect transistor. Also shown how ions bound to the surface to neutralize the traps.

References

1. Novoselov KS, Geim AK, Morozov SV, Jiang D, Zhang Y, Dubonos SV, *et al.* Electric Field Effect in Atomically Thin Carbon Films. *Science* 2004, **306**(5696)**:** 666-669.

2. Novoselov KS, Jiang D, Schedin F, Booth TJ, Khotkevich VV, Morozov SV, *et al.* Two-dimensional atomic crystals. *Proceedings of the National Academy of Sciences of the United States of America* 2005, **102**(30)**:** 10451-10453.

3. Li H, Wu J, Huang X, Lu G, Yang J, Lu X, *et al.* Rapid and Reliable Thickness Identification of Two-Dimensional Nanosheets Using Optical Microscopy. *ACS Nano* 2013, **7**(11)**:** 10344-10353.

4. Li H, Wu J, Yin Z, Zhang H. Preparation and Applications of Mechanically Exfoliated Single-Layer and Multilayer MoS2 and WSe2 Nanosheets. *Accounts of Chemical Research* 2014, **47**(4)**:** 1067-1075.

5. Bang JH, Suslick KS. Applications of Ultrasound to the Synthesis of Nanostructured Materials. *Advanced Materials* 2010, **22**(10)**:** 1039-1059.

6. Smith RJ, King PJ, Lotya M, Wirtz C, Khan U, De S, *et al.* Large-Scale Exfoliation of Inorganic Layered Compounds in Aqueous Surfactant Solutions. *Advanced Materials* 2011, **23**(34)**:** 3944-3948.

7. Cunningham G, Lotya M, Cucinotta CS, Sanvito S, Bergin SD, Menzel R, *et al.* Solvent Exfoliation of Transition Metal Dichalcogenides: Dispersibility of Exfoliated Nanosheets Varies Only Weakly between Compounds. *ACS Nano* 2012, **6**(4)**:** 3468-3480.

8. O'Neill A, Khan U, Nirmalraj PN, Boland J, Coleman JN. Graphene Dispersion and Exfoliation in Low Boiling Point Solvents. *The Journal of Physical Chemistry C* 2011, **115**(13)**:** 5422-5428.

9. Benavente E, Santa Ana MA, Mendizábal F, González G. Intercalation chemistry of molybdenum disulfide. *Coordination Chemistry Reviews* 2002, **224**(1)**:** 87-109.

10. Huang X, Zeng Z, Zhang H. Metal dichalcogenide nanosheets: preparation, properties and applications. *Chemical Society Reviews* 2013, **42**(5)**:** 1934-1946.

11. Yuwen L, Yu H, Yang X, Zhou J, Zhang Q, Zhang Y, *et al.* Rapid preparation of single-layer transition metal dichalcogenide nanosheets via ultrasonication enhanced lithium intercalation. *Chemical Communications* 2016, **52**(3)**:** 529-532.

12. Daeneke T, Clark RM, Carey BJ, Ou JZ, Weber B, Fuhrer MS, *et al.* Reductive exfoliation of substoichiometric MoS2 bilayers using hydrazine salts. *Nanoscale* 2016, **8**(33)**:** 15252-15261.

13. Zeng Z, Yin Z, Huang X, Li H, He Q, Lu G, *et al.* Single-Layer Semiconducting Nanosheets: High-Yield Preparation and Device Fabrication. *Angewandte Chemie International Edition* 2011, **50**(47)**:** 11093-11097.

14. Zeng Z, Sun T, Zhu J, Huang X, Yin Z, Lu G, *et al.* An Effective Method for the Fabrication of Few-Layer-Thick Inorganic Nanosheets. *Angewandte Chemie International Edition* 2012, **51**(36)**:** 9052-9056.

15. Najmaei S, Liu Z, Zhou W, Zou X, Shi G, Lei S, *et al.* Vapour phase growth and grain boundary structure of molybdenum disulphide atomic layers. *Nature Materials* 2013, **12:** 754.

16. Lu X, Utama MIB, Lin J, Gong X, Zhang J, Zhao Y, *et al.* Large-Area Synthesis of Monolayer and Few-Layer MoSe2 Films on SiO2 Substrates. *Nano Letters* 2014, **14**(5)**:** 2419-2425.

17. Bointon TH, Barnes MD, Russo S, Craciun MF. High Quality Monolayer Graphene Synthesized by Resistive Heating Cold Wall Chemical Vapor Deposition. *Advanced Materials* 2015, **27**(28)**:** 4200-4206.

18. Wang X, Zhi L, Tsao N, Tomović Ž, Li J, Müllen K. Transparent Carbon Films as Electrodes in Organic Solar Cells. *Angewandte Chemie International Edition* 2008, **47**(16)**:** 2990-2992.

19. Choucair M, Thordarson P, Stride JA. Gram-scale production of graphene based on solvothermal synthesis and sonication. *Nature Nanotechnology* 2008, **4:** 30.

20. Yoo D, Kim M, Jeong S, Han J, Cheon J. Chemical Synthetic Strategy for Single-Layer Transition-Metal Chalcogenides. *Journal of the American Chemical Society* 2014, **136**(42)**:** 14670-14673.

21. Britnell L, Gorbachev RV, Jalil R, Belle BD, Schedin F, Mishchenko A, *et al.* Field-Effect Tunneling Transistor Based on Vertical Graphene Heterostructures. *Science* 2012, **335**(6071)**:** 947-950.

22. Georgiou T, Jalil R, Belle BD, Britnell L, Gorbachev RV, Morozov SV, *et al.* Vertical field-effect transistor based on graphene-WS2 heterostructures for flexible and transparent electronics. *Nat Nano* 2013, **8**(2)**:** 100-103.

23. Sup Choi M, Lee G-H, Yu Y-J, Lee D-Y, Hwan Lee S, Kim P, *et al.* Controlled charge trapping by molybdenum disulphide and graphene in ultrathin heterostructured memory devices. *Nature Communications* 2013, **4:** 1624.

24. Bertolazzi S, Krasnozhon D, Kis A. Nonvolatile Memory Cells Based on MoS2/Graphene Heterostructures. *ACS Nano* 2013, **7**(4)**:** 3246-3252.

25. Hong X, Kim J, Shi S-F, Zhang Y, Jin C, Sun Y, *et al.* Ultrafast charge transfer in atomically thin MoS2/WS2 heterostructures. *Nature Nanotechnology* 2014, **9:** 682.

26. Wang H, Zhang C, Chan W, Tiwari S, Rana F. Ultrafast response of monolayer molybdenum disulfide photodetectors. *Nature Communications* 2015, **6:** 8831.

27. MassicotteM, SchmidtP, ViallaF, Schädler KG, Reserbat Plantey A, WatanabeK, *et al.* Picosecond photoresponse in van der Waals heterostructures. *Nat Nano* 2016, **11**(1)**:** 42-46.

28. Mehew JD, Unal S, Torres Alonso E, Jones GF, Fadhil Ramadhan S, Craciun MF, *et al.* Fast and Highly Sensitive Ionic-Polymer-Gated WS2–Graphene Photodetectors. *Advanced Materials* 2017**:** 1700222-n/a.

29. Cheng R, Li D, Zhou H, Wang C, Yin A, Jiang S, *et al.* Electroluminescence and Photocurrent Generation from Atomically Sharp WSe2/MoS2 Heterojunction p–n Diodes. *Nano Letters* 2014, **14**(10)**:** 5590-5597.

30. Withers F, Del Pozo-Zamudio O, Mishchenko A, Rooney AP, Gholinia A, Watanabe K, *et al.* Light-emitting diodes by band-structure engineering in van der Waals heterostructures. *Nat Mater* 2015, **14**(3)**:** 301-306.

31. Withers F, Del Pozo-Zamudio O, Schwarz S, Dufferwiel S, Walker PM, Godde T, *et al.* WSe2 Light-Emitting Tunneling Transistors with Enhanced Brightness at Room Temperature. *Nano Letters* 2015, **15**(12)**:** 8223-8228.

32. DasA, PisanaS, ChakrabortyB, PiscanecS, Saha SK, Waghmare UV, *et al.* Monitoring dopants by Raman scattering in an electrochemically top-gated graphene transistor. *Nat Nano* 2008, **3**(4)**:** 210-215.

33. Pisana S, Lazzeri M, Casiraghi C, Novoselov KS, Geim AK, Ferrari AC, *et al.* Breakdown of the adiabatic Born–Oppenheimer approximation in graphene. *Nature Materials* 2007, **6:** 198.

34. Stampfer C, Molitor F, Graf D, Ensslin K, Jungen A, Hierold C, *et al.* Raman imaging of doping domains in graphene on SiO2. *Applied Physics Letters* 2007, **91**(24)**:** 241907.

35. Casiraghi C. Doping dependence of the Raman peaks intensity of graphene close to the Dirac point. *Physical Review B* 2009, **80**(23)**:** 233407.

36. Froehlicher G, Berciaud S. Raman spectroscopy of electrochemically gated graphene transistors: Geometrical capacitance, electron-phonon, electron-electron, and electron-defect scattering. *Physical Review B* 2015, **91**(20)**:** 205413.

37. Ando T. Anomaly of Optical Phonon in Monolayer Graphene. *Journal of the Physical Society of Japan* 2006, **75**(12)**:** 124701.

38. Lazzeri M, Mauri F. Nonadiabatic Kohn Anomaly in a Doped Graphene Monolayer. *Physical Review Letters* 2006, **97**(26)**:** 266407.

39. Yan J, Zhang Y, Kim P, Pinczuk A. Electric Field Effect Tuning of Electron-Phonon Coupling in Graphene. *Physical Review Letters* 2007, **98**(16)**:** 166802.

40. Ryan B, Luiz Gustavo C, Lukas N. Raman characterization of defects and dopants in graphene. *Journal of Physics: Condensed Matter* 2015, **27**(8)**:** 083002.

41. Peres NMR, Guinea F, Castro Neto AH. Electronic properties of disordered two-dimensional carbon. *Physical Review B* 2006, **73**(12)**:** 125411.

42. Lazzeri M, Piscanec S, Mauri F, Ferrari AC, Robertson J. Phonon linewidths and electron-phonon coupling in graphite and nanotubes. *Physical Review B* 2006, **73**(15)**:** 155426.

43. Marianetti CA, Yevick HG. Failure Mechanisms of Graphene under Tension. *Physical Review Letters* 2010, **105**(24)**:** 245502.

44. Liu F, Ming P, Li J. Ab initio calculation of ideal strength and phonon instability of graphene under tension. *Physical Review B* 2007, **76**(6)**:** 064120.

45. Niclas SM, Sebastian H, Miriam Peña A, Patryk K, Sören W, Nick C, *et al.* Evaluating arbitrary strain configurations and doping in graphene with Raman spectroscopy. *2D Materials* 2018, **5**(1)**:** 015016.

46. Mohiuddin TMG, Lombardo A, Nair RR, Bonetti A, Savini G, Jalil R, *et al.* Uniaxial strain in graphene by Raman spectroscopy: G peak splitting, Gr\"uneisen parameters, and sample orientation. *Physical Review B* 2009, **79**(20)**:** 205433.

47. Shioya H, Craciun MF, Russo S, Yamamoto M, Tarucha S. Straining Graphene Using Thin Film Shrinkage Methods. *Nano Letters* 2014, **14**(3)**:** 1158-1163.

48. Huang M, Yan H, Chen C, Song D, Heinz TF, Hone J. Phonon softening and crystallographic orientation of strained graphene studied by Raman spectroscopy. *Proceedings of the National Academy of Sciences* 2009, **106**(18)**:** 7304-7308.

49. Yoon D, Son Y-W, Cheong H. Strain-Dependent Splitting of the Double-Resonance Raman Scattering Band in Graphene. *Physical Review Letters* 2011, **106**(15)**:** 155502.

50. Androulidakis C, Koukaras EN, Parthenios J, Kalosakas G, Papagelis K, Galiotis C. Graphene flakes under controlled biaxial deformation. 2015, **5:** 18219.

51. Lee JE, Ahn G, Shim J, Lee YS, Ryu S. Optical separation of mechanical strain from charge doping in graphene. *Nat Commun* 2012, **3:** 1024.

52. Chen J-H, Jang C, Xiao S, Ishigami M, Fuhrer MS. Intrinsic and extrinsic performance limits of graphene devices on SiO2. *Nat Nano* 2008, **3**(4)**:** 206-209.

53. Morozov SV, Novoselov KS, Katsnelson MI, Schedin F, Elias DC, Jaszczak JA, *et al.* Giant Intrinsic Carrier Mobilities in Graphene and Its Bilayer. *Physical Review Letters* 2008, **100**(1)**:** 016602.

54. Cho JH, Lee J, He Y, Kim BS, Lodge TP, Frisbie CD. High-Capacitance Ion Gel Gate Dielectrics with Faster Polarization Response Times for Organic Thin Film Transistors. *Advanced Materials* 2008, **20**(4)**:** 686-690.

55. Shimotani H, Asanuma H, Tsukazaki A, Ohtomo A, Kawasaki M, Iwasa Y. Insulator-to-metal transition in ZnO by electric double layer gating. *Applied Physics Letters* 2007, **91**(8)**:** 082106.

56. Ye J, Craciun MF, Koshino M, Russo S, Inoue S, Yuan H, *et al.* Accessing the transport properties of graphene and its multilayers at high carrier density. *Proceedings of the National Academy of Sciences* 2011, **108**(32)**:** 13002-13006.

57. Chen F, Xia J, Tao N. Ionic Screening of Charged-Impurity Scattering in Graphene. *Nano Letters* 2009, **9**(4)**:** 1621-1625.

Chapter 4

Linear Magnetoresistance (LMR) from bubbles

4.1 Introduction

Heterostructures of atomically thin systems can be attained by stacking different 2D material layers on top each other. The interaction between layers is governed by the Van der Waal force (vdW). One of the most important features of such artificial materials is the ability to realize clean interfaces which do not suffer of inter-diffusion, and are therefore atomically sharp. The surface of 2D materials is usually contaminated by moisture and hydrocarbons which are inadvertently introduced during the exfoliation and fabrication processes. In stacked structures, the vdW force squeezes the contaminants and localizes them into pockets which appear as 'bubbles' or blisters on the surface of the sample, leaving large interface areas atomically sharp and free of contamination. Consequently, this inhomogeneity can lead to fluctuations of the charge carrier mobility and of the Fermi energy. Presently the fabrication of devices with clean interface takes a considerable effort since clean patches of sufficiently large surface area need to be identified. On the other hand, conductive systems with inhomogeneous charge carrier mobility and/or inhomogeneous charge density can be uniquely suitable to study a non-saturating linear Magnetoresistance (LMR). Indeed, in standard bulk semiconductors stochastic spatial fluctuations of the charge carrier mobility have been shown to lead to LMR as also described by the PL Model[56]. However, the classical 3D semiconductors have issues with thickness reduction. The mobility μ of charge carriers decreases with thickness to the sixth power, $\mu \sim t^6$, and the band gap, ΔE , increases by the square of the thickness, ($\Delta E \sim t^2$) [105, 106, 107].

The emerging class of 2D materials, and in particular graphene, have attracted tremendous attention as unique systems suitable to study non-saturating linear Magnetoresistance (LMR). Graphene is known to exhibit high charge carrier mobility at room temperature which is also highly dependent on the contamination

of the surface. Therefore, it is easy to generate inhomogeneity of the carrier density and/or charge carrier mobility in this single layer of carbon atoms, making this material ideally suited to explore the non-saturating linear magnetoresistance at room temperature.

High Mobility graphene (> 10 $m^2 V^{-1}s^{-1}$) is achieved by placing graphene on hBN[32].The planar surface of hBN cleaves into an ultra-flat surface and the ionic bonding of hBN should leave it free of dangling bonds and charge traps at the surface. Charge carrier mobility in graphene on hBN substrates is mostly limited by contamination which self-cleans into bubbles between the graphene and the hBN[108]. These bubbles play a crucial role on the electrical properties of graphene and act as sources of high inhomogeneity and mobility fluctuations. In this work, we make use of these bubbles to enhance the linear magneto resistance in graphene.

4.2 SAMPLE PREPARATION AND TOPOGRAPHIC CHARACTERIZATION

The heterostructures used in this study are obtained by dry transfer technique as discussed in previous chapter. hBN flakes were peeled from an hBN crystal using adhesive tape and they were subsequently transferred to the Si/SiO_2 wafers where they were left for several hours at ambient conditions. In this time frame, unwanted contaminants present in the atmosphere e.g. hydrocarbons deposit onto the surface of hBN with a longer waiting time resulting in a larger degree of contamination. Single layer graphene was exfoliated on top of PMM/PMGI and transferred on hBN by dry technique to obtained Graphene/hBN heterostructures. In this work, more than 20 samples were fabricated employing different waiting time for the hBN in atmosphere, which resulted in different levels of contamination and ultimately inhomogeneity of the electrical properties of graphene. As a reference, five clean interface samples were also fabricated. The optical contrast images along with the

topography measurements probed with Atomic Force Microscopy (AFM) on a representative device for each subset of samples are shown in **Figure (4-1a and b)**. The AFM images reveal a random distribution in size and shapes of the bubbles along the channel of the contaminated interface, whilst a representative clean device shows no measurable bubbles within the resolution of the AFM instrument.

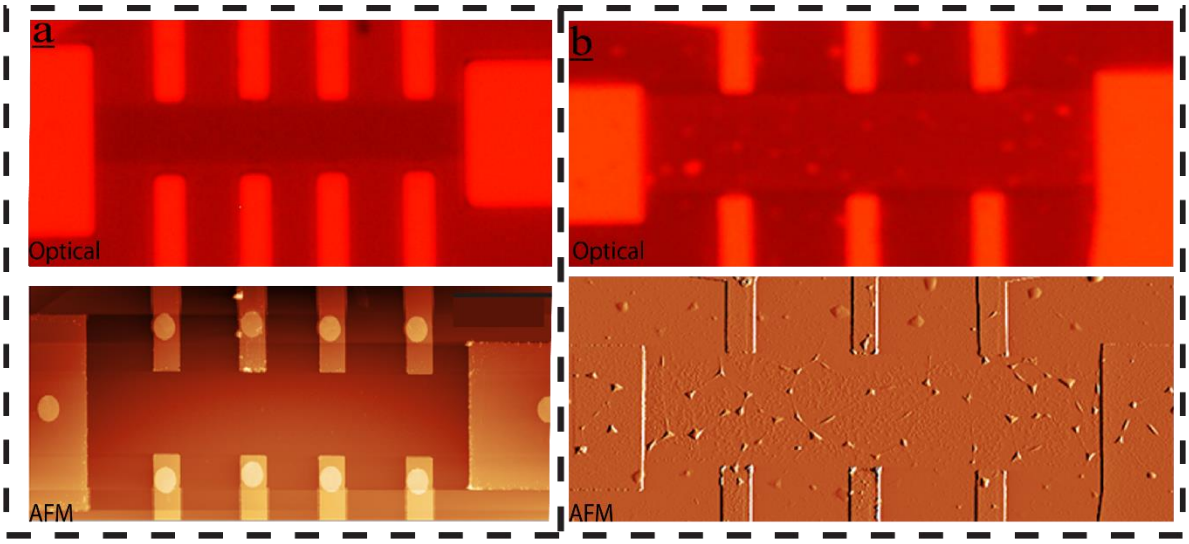

Figure 4- 1 Optical contrast and AFM images **a-** Device without bubbles, upper is optical image while lower is AFM image. **b-** Device with bubbles, upper is optical image while lower is AFM image.

Indeed, a high resolution cross section AFM height measurement acquired at different places in the graphene channel shows a variable height (width) of the bubbles, see **Figure (4-2a)**. A statistical study of the coverage percentage and the average for the entire surface of the two devices (D1 and D2) is shown in **Figure (4-2b)**. The statistical analyses are extracted after the images of AFM have converted to pixels data in MATLAB. It is apparent that these data follow a non-Gaussian distribution such as a Weibull function, widely used in reliability and life data analysis, which demonstrates that there is a single distinct population of pixels and it gives a better estimate of the median, average and standard deviation for small

sample size. **Table (4.1)** gives the summary of coverage percentage, average height, median and standard deviation from D1 and D2.

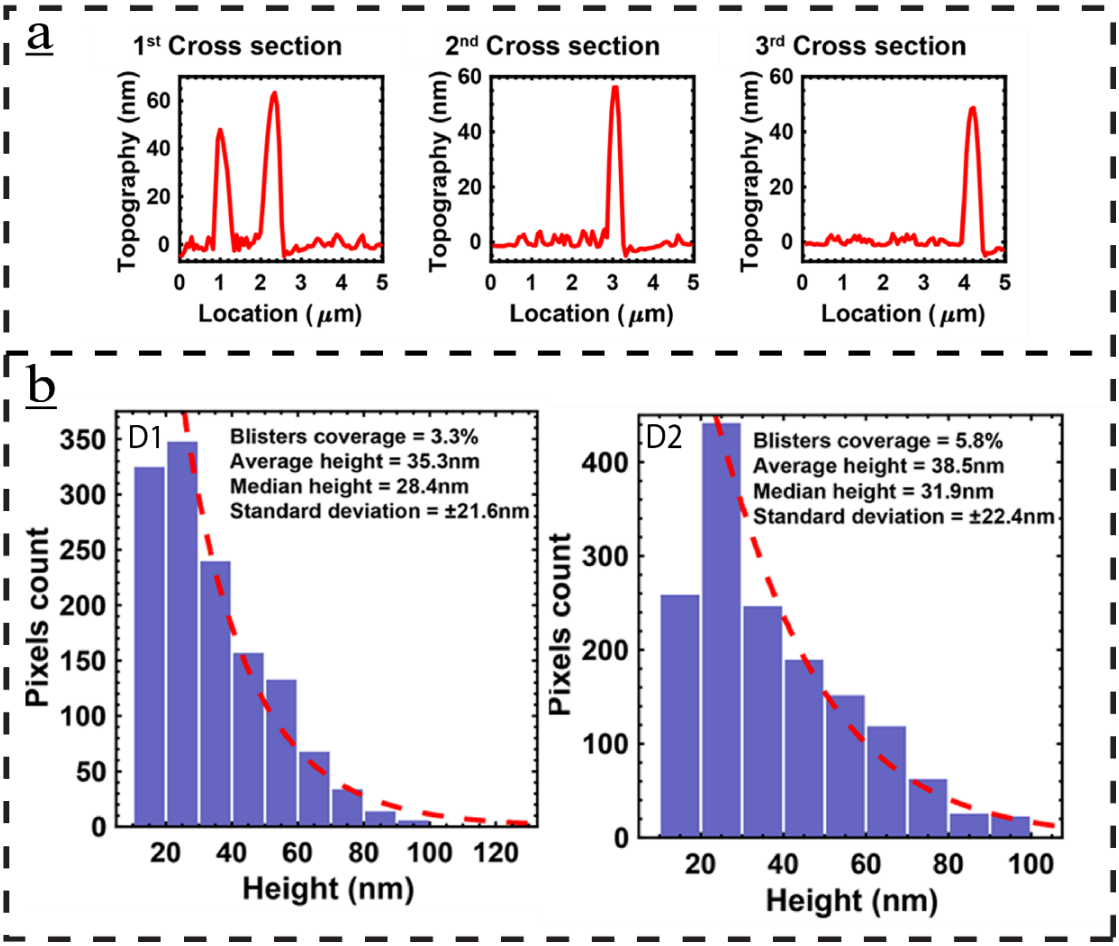

Figure 4- 2 Statistical properties of graphene with bubbles **a-** The profile of selected bubbles, up to 60 nm in height. **b-** The statistical coverage percentage and the Average height for the entire surface of D1 and D2 with bubbles.

Table 4.1: The summary analysis of topological surface of D1 and D2, both with bubbles		
	Device 1	Device 2
Coverage (%)	3.3	5.8
Average height (nm)	35.3	38.5
Median (nm)	28.4	31.9
Standard Deviation (nm)	22.4	21.6

In this case, the probability density function (PDF) is given by

$$PDF(x) = NW_B(\frac{\beta}{\theta})\,(\frac{x-\delta}{\theta})^{\beta-1}\,exp\left[-(\frac{x-\delta}{\theta})^{\beta}\right], \qquad (3\text{-}1)$$

where NW_B is a normalization factor (N- number of samples, W_B- width of the histogram bin), β is the so-called shape factor, θ is the scale factor and δ is the shift factor. The expressions for the mean, median and standard deviation are given by the following equations.

Mean $\bar{x} = \theta.\Gamma\left(1+\frac{1}{\beta}\right)$.

Median $med(x) = \theta(ln2)^{1/\beta}$.

Standard déviation $st.dev(x) = \theta\sqrt{\Gamma(1+\frac{2}{\beta}) - (\Gamma(1+\frac{1}{\beta}))^2}$.

4.3 Electronic Properties

The charge transport in graphene/hBN heterostructure devices with and without bubbles were investigated. For this purpose, the gate and magnetic field dependence of the longitudinal resistance (R_{xx}) was measured using a lock-in technique in a

current bias configuration at room temperature. From these data, the field effect mobility (μ_{FET}) was extracted from a gate-sweep of the longitudinal resistance

$$\mu_{FET} = \frac{Id}{\varepsilon_0 \varepsilon_{ox}} \frac{V_{BG}}{R_{xx}},$$

where I is the applied bias current, ε_0 is the vacuum permittivity, V_{BG} is the applied back-gate voltage bias, d and ε_{ox} are the thickness and permittivity of SiO_2, respectively.

The magnetoresistance is given by $MR = (\Delta R(B)/R(0)) \times 100\%$, where $\Delta R(B)$ is the change of the sample resistance at a fixed value of back gate voltage upon applying magnetic field, $R(0)$ is the value of the sample resistance at zero magnetic field.

A comparison of the graphs of μ_{FET} vs. V_{BG} for the systems without and with bubbles reveals that the measured charge carrier mobility in clean structures is systematically higher than the one measured in devices with bubbles, see **Figure (4-3a)**. The bubbles originate from either trapped hydrocarbons or moisture and they could influence the electronic properties of graphene by either strain or charge and hence affect the overall mobility of devices [108, 109, 110, 111].

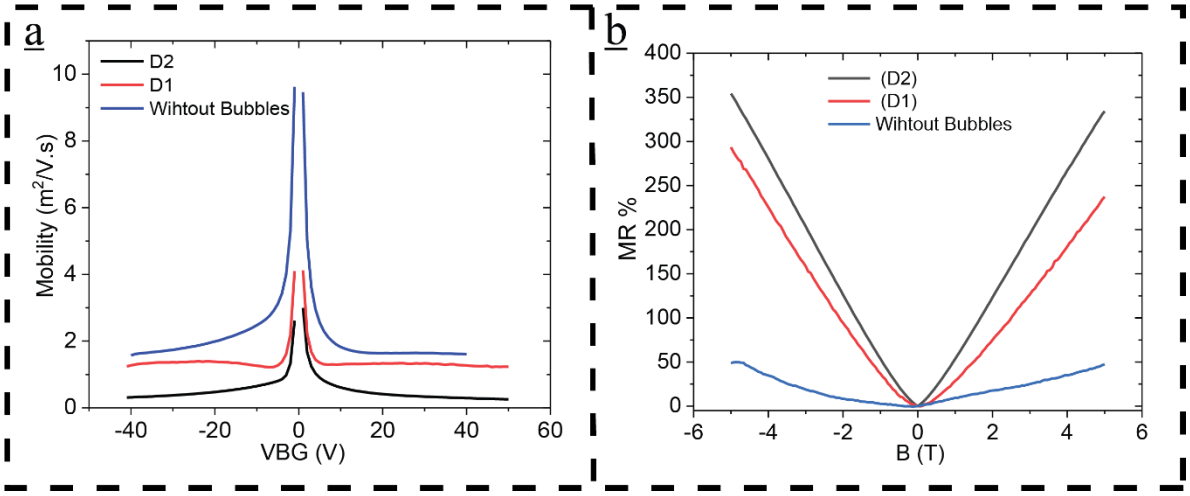

Figure 4- 3 Transport properties **a-** Mobility vs. back gate voltage for three devices; one without and two with bubbles in the different density of coverage. **b-** Room temperature LMR for the devices in (a) when $V_{BG} = 5V$.

At the same time, the devices with the bubbles showed a positive and non-saturating linear magnetoresistance more than 40 times larger than the MR measured in clean structures under the same experimental conditions, see **Figure (4-3b)**. More specifically, at $V_{BG} = 5V$ under a value of magnetic field of 5T applied perpendicular to the plane of graphene and at room temperature in vacuum conditions ($2.5*10^{-6}$ mbar) the devices with bubbles display a MR as large as 350% whilst the MR in clean devices is only up to 50%.

In order to explore the possible microscopic origin of the LMR, the MR of devices with different distributions of bubbles have been studied. The device (D2) with higher density of bubbles showed higher LMR than the one with lower density of bubbles (D1). From **Figure (4-3a)** it is also clear that the charge carrier mobility measured in D2 is much smaller than that measured in D1. This experimental evidence shows a correlation between the LMR signal and the distribution of bubbles in graphene/h-BN structures. The results from both of these devices are summarized in **Table (4.1)**.

A post-processing annealing of the samples under 10% Hydrogen/Argon gases at temperature of 300 °C for 3 hours is a well-known procedure used to remove contaminants from graphene and enhance its electrical properties[111, 112]. The device D2 was subjected to this annealing procedure and a clear enhancement of the charge carrier mobility was observed, consistently with previous reports (see **Figure (4-4a)**). On the other hand, **Figure (4-4b)** shows that a significant decrease in the LMR of the same devices is observed. A topographic study of these devices also shows that upon annealing the overall bubbles coverage area was reduced from 5:8% to 2:3% and 38:5 to 23:5.

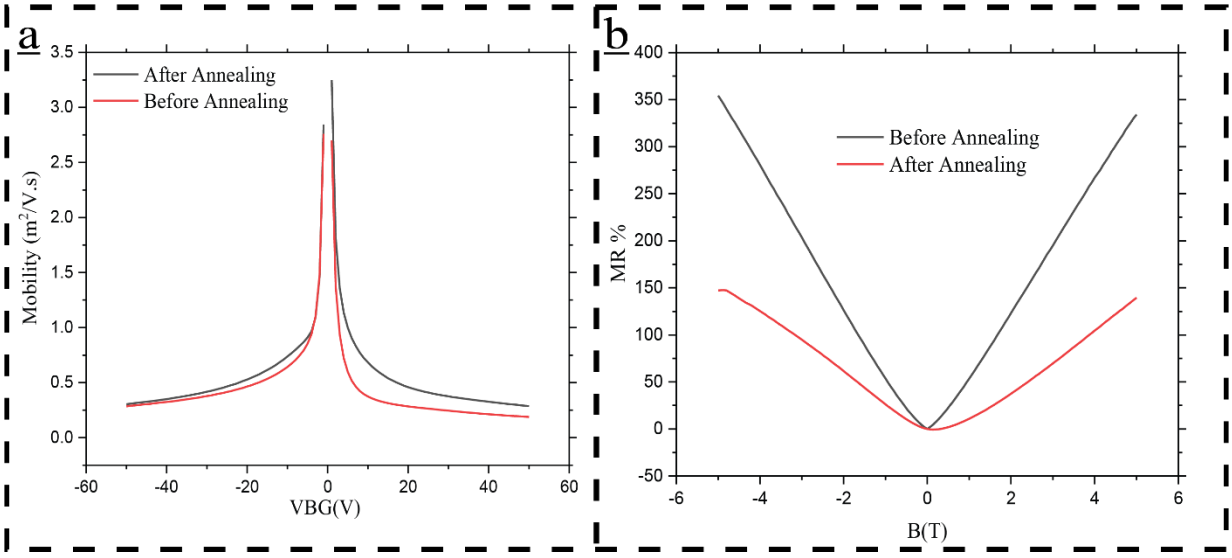

Figure 4- 4 Annealing effect on LMR **a-** Mobility before and after annealing **b-** LMR before and after annealing.

4.4 Raman Spectroscopy of encapsulated graphene in h-BN

Raman spectroscopy is widely recognized to be a powerful and non-invasive method to study atomically thin materials. The range of properties that can be characterized includes the identification of the number of layers, levels of doping and strain[88, 95, 99, 113]. In the case of graphene, this information is predominantly contained in the

phonon frequency of the $G(\omega_G)$ and $2D(\omega_{2D})$ peaks. These are significantly sensitive to doping as well as strain present in the system, owing to the static effect on the bond lengths and non-adiabatic electron-phonon coupling[86, 113]. As discussed in Chapter three (3-3), spatially resolved scans of the Raman spectra provide the spatial information on the shift of the frequency of the G and 2D peak positions.

Raman spectra of the graphene/hBN devices were acquired using an Ar ion laser excitation operated at wavelength 532 nm (2.33 eV) delivered through a single-mode optical fibre, the system is described in Chapter three (3.4.2). Using a long working distance focusing lens with a numerical aperture NA = 0:80 a spot size of about 500 nm on the sample was obtained. Very low incident power of 4-7 μW is employed to avoid sample damage or laser-induced heating. Two-Dimensional Raman maps were acquired in air and at room temperature using motorized stage controls for the x- and y-directions of the microscope stage, with a step size of 0.5 μm. **Figure (4-5a)** shows two colour-coded plots of the spatially resolved position of the $2D(\omega_{2D})$ and $G(\omega_G)$ peaks. For a detailed analysis, each Raman spectrum is offset using the Silicon peak as a reference prior to a fit with Lorentzian curves for the known graphene Raman resonances. The maps exhibit significant position-dependent shifts of the aforementioned peaks. Although, it has been shown that in graphene, both strain and doping can shift the position of the G and 2D peaks, a systematic study that correlates a micro-scale map of strain and doping to the electrical magneto-transport properties in graphene/hBN has not yet been conducted.

A representative spatially resolved Raman map of the samples without bubbles is shown in **Figure (4-5b)**. For this sample high shifts of the G and 2D peak frequencies are measured in the regions between the lateral contact probes as well as in the area near the main contacts. This experimental evidence indicates that the metal contacts introduce strain in graphene. Indeed, Raman studies of graphene on hBN have

revealed a different microscopic strain distribution in the case both layers are oriented to form a commensurate state. In this case, the rotation angle (Ɵ) between the lattice of graphene and that of hBN must be less than the difference between the two lattice constants Ɵ=1.8%[114, 115]. This leads to a dramatic modification of the energy dispersion of graphene with the appearance of satellite Dirac cones at non-zero energy. In electrical transport measurements, such a modification of the energy dispersion in the commensurate state leads to the appearance of a second Dirac peak away from the neutrality point [116]. However, this satellite Dirac peak was not observed in the electrical measurements of the devices of **Figure (4-5d)**.

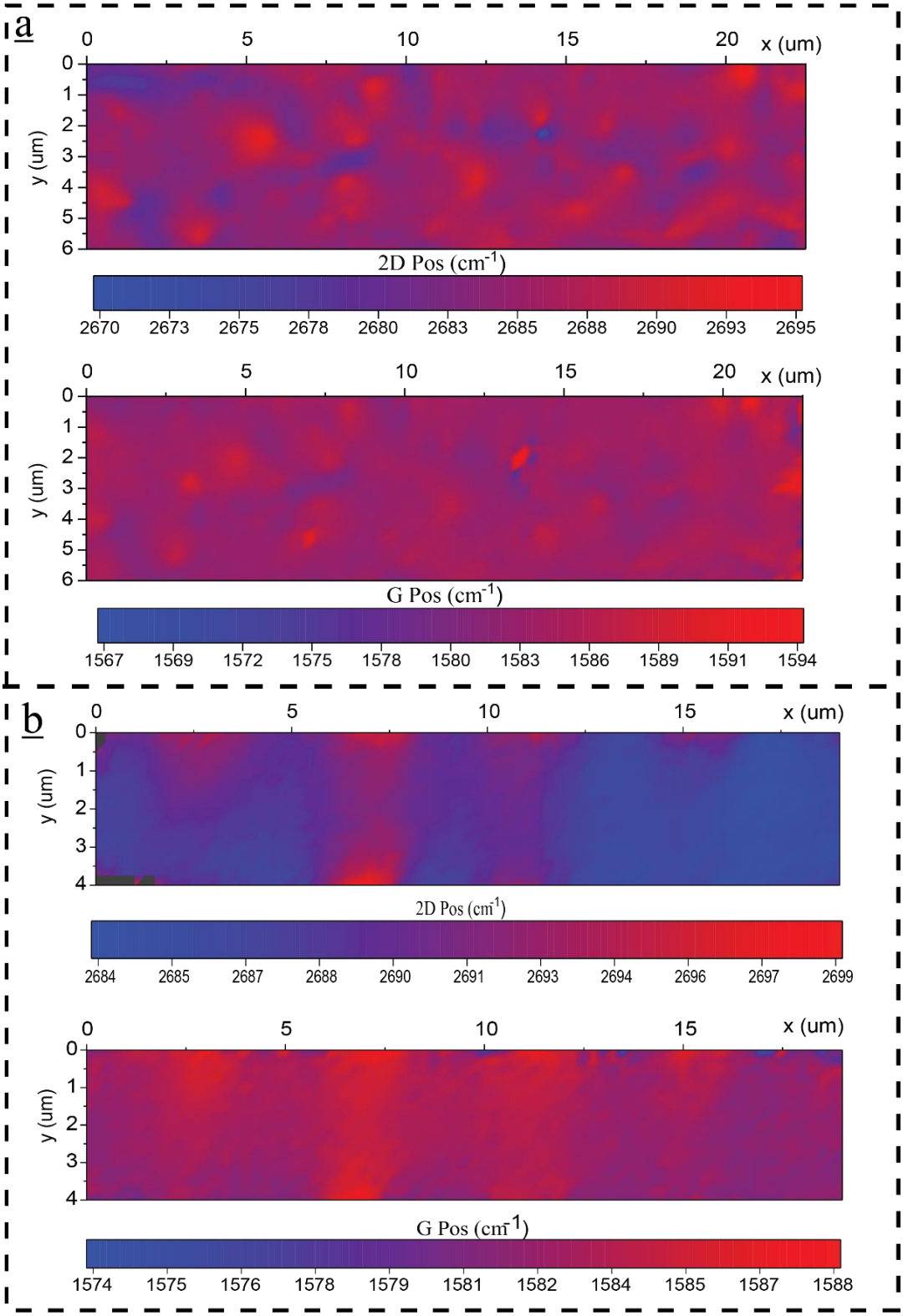

Figure 4- 5 Raman mapping for graphene **a-** with bubbles: 2D peak shifting and G peak shifting**. d-** without bubbles: 2D shifting and G shifting

4.4.1 Doping and Strain quantities and correlation

The peak positions of the $G(\omega_G)$ *and* $2D(w\omega_{2D})$ Raman resonances contain valuable information on the quality, doping level, and strain of graphene samples. In other words, this unique relation between the position of G and $2D$ peaks provide us either the strain or the doping in the sample, as we showed in section (3.3.2). If the strain is dominated the relation between ($G(\omega_G)$ *and* $2D(\omega_{2D})$) should be linear while when the doping is dominated the relation will be nonlinear[99, 113].

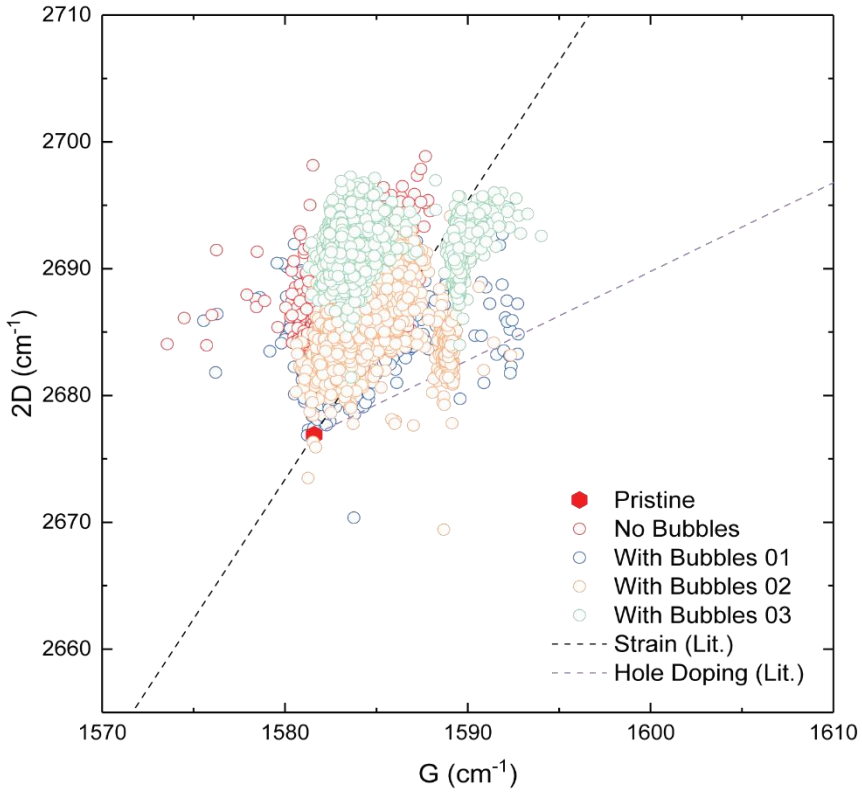

Figure 4- 6 Correlation between the frequencies of the G and 2D peaks: The data were extracted from Raman mapping for three devices; two with bubbles while the other one without bubbles. The magenta dashed line is an average of experimental data ($G(\omega_G)$ *and* $D(\omega_{2D})$) for strain-free graphene with varying density of holes (n). The black dashed line represents a prediction of ($G(\omega_G)$ *and* $D(\omega_{2D})$) for charge-neutral graphene under randomly oriented uniaxial stress area.

Strain and doping can be extracted from these data by projecting the point onto the correlation axes between strain and doping indicated by dashed lines in the plot of **Figure (4-6)**.

To extract the values of the charge density for graphene from the Raman spectra, a model developed by Lazzeri et al[86] can be used.

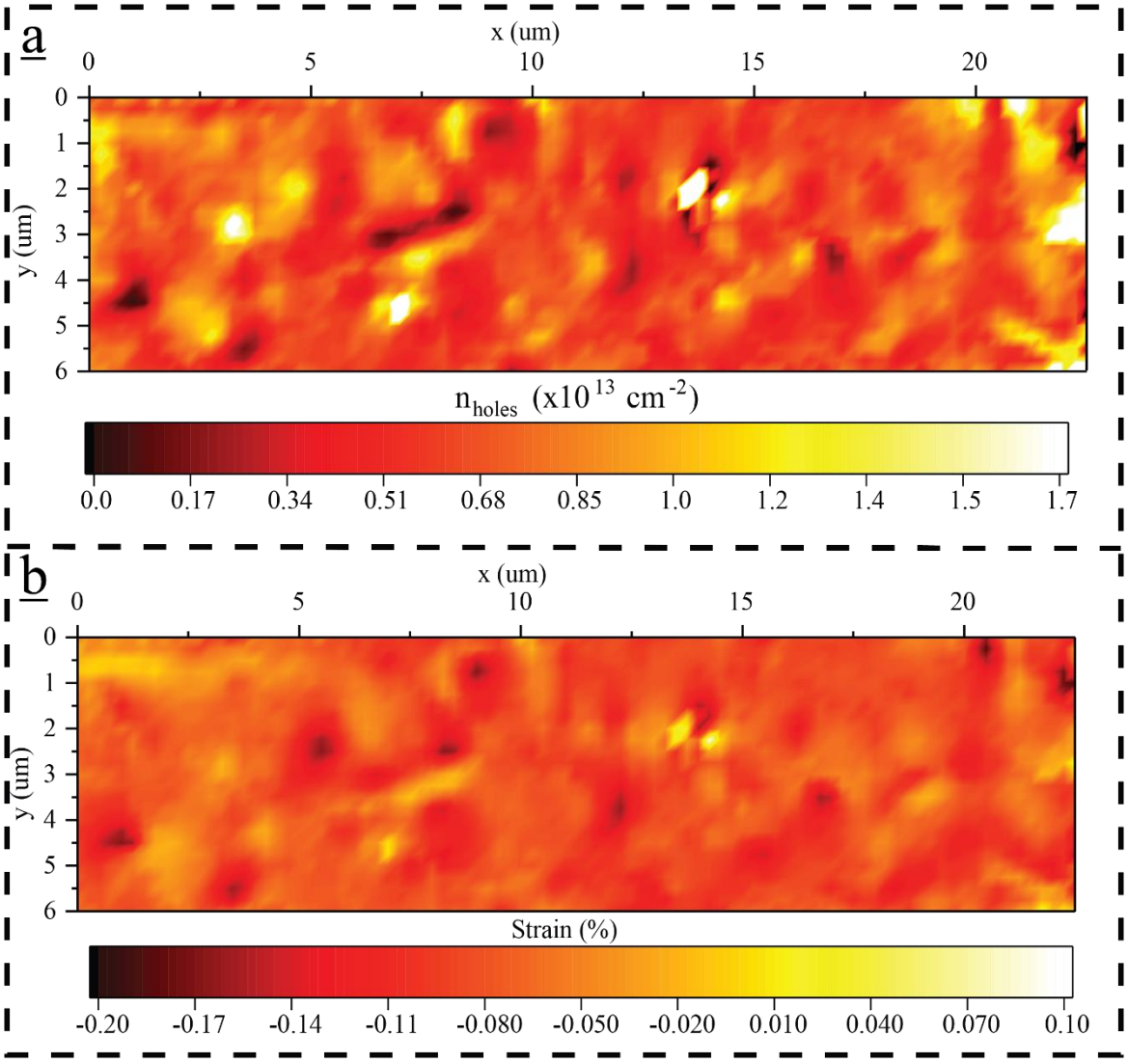

Figure 4- 7 Decomposition of the effect of spatial variation of strain and doping concurrent in the whole graphene layer **a**- Doping variation**. b**- Strain variation.

A relation between *n* and the upshift of the G-peak position with an accuracy less than 10% has been demonstrated. **Figure (4-7a)** shows the spatial dependence of the charge density extracted using the aforementioned model in a representative sample. Significant charge density fluctuations are apparent. The strain values can be extracted using a model developed by Lee et al [99]. **Figure (4-7b)** gives the values of strain throughout graphene surface.

Using a fit to a Gaussian function, the full width half maximum (FWHM) of the statistical distribution of strain and doping for graphene devices can be determined. A comparison of the statistical distribution for several graphene/hBN devices reveals that the FWHM of charge density is typically larger than that of the strain, see in **Figure (4-8a)**. This finding show that doping will have a prominent role on the properties of typical graphene/hBN. In addition to that, the strain variation width among the samples are comparable for all the studied samples, see **Figure (4-8b)**. Therefore, the relative variation of strain is less important than the variation of the doping. We extracted Δn, change in the charge carrier density, for the devices with bubbles are ($3.35 \times 10^{12}\, cm^2$) and ($2.21 \times 10^{12}\, cm^2$) while for the one without bubbles it is ($1.25 \times 10^{12}\, cm^2$).

4.5 MACROSCOPIC PROPERTIES

The presence of non-uniform doping and strain in graphene/hBN with bubbles has a profound impact on the performance of devices based on these heterostructures. In such systems, the inhomogeneity of the charge carrier mobility can be modelled with a 2D random resistor network. In this case the fluctuation of the conductivity Δσ rather than the conductivity σ itself dominate the electrical transport properties.

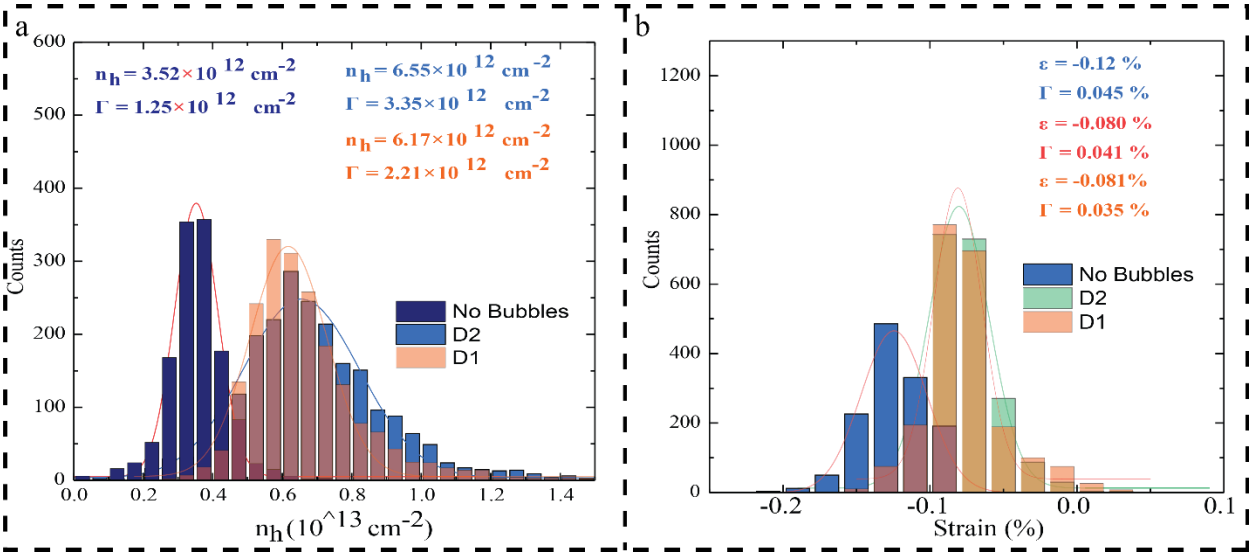

Figure 4- 8 Statistical study of $\Delta n \; and \; \Delta\varepsilon$ over the whole graphene layer for three samples; two with bubbles and one without bubble. **a-** charge density distribution where $\Gamma = (3.35, 2.21 \; and \; 1.25)e^{12}cm^{-2}$ **b-** strain distribution where ($\Gamma = (0.045, 0.041 \; and \; 0.035)$ %, with and without bubbles respectively.

The PL model shows that $\Delta R \propto H$ in the case of a 2D random resistor network, justifying the observation of a linear magnetoresistance in a random network of graphene bubbles. It can be shown that within the PL model and at sufficiently large values of magnetic fields: -

$$\frac{\Delta R(H)}{R(0)} \propto < \mu > \quad for \; \frac{\Delta\mu}{< \mu >} < 1$$

$$\frac{\Delta R(H)}{R(0)} \propto \Delta\mu \qquad for \; \frac{\Delta\mu}{< \mu >} > 1$$

Where $\Delta\mu$ and $< \mu >$ are the width and the average value of the statistical distribution of the mobility in a device.

A correlation of the statistical study of the distribution of the charge density and strain in a representative device to their magneto-transport properties reveals that the larger is the fluctuation of charge carrier density Δn, the larger is the measured value of LMR, see **Figure (4-8 and 4-3)**. Since, our data in **Figure (4-8)** is compatible with the first condition ($\frac{\Delta\mu}{<\mu>} < 1$); that means LMR is determined by the average of mobility$< \mu >$ in our inhomogeneity conductor.

The above analysis indicates the following mechanism behind our observed magnetoresistance. In the absence of an applied magnetic field, the local current will percolate through the media with higher conductivity. This means that the current path will be aligned with the direction of the applied voltage, resulting in the local Hall current to be zero. Under an applied perpendicular magnetic, the Lorentz force will force the effective drift velocity paths of the current to become no longer aligned to the direction of the applied voltage. The current paths will acquire spatial fluctuations in both magnitude and direction, because of the small-angle scattering near low-mobility islands. This will result in current loops within the inhomogeneous system, leading to a non-zero local Hall current. The inhomogeneity across the channel will make a significant proportion of the Hall current paths throughout the channel. Their paths will be perpendicular to the direction of the applied voltage. This will lead to a linear magnetoresistance especially at high field, because the current strongly disrupts the medium along the longitudinal voltage. Therefore, the Hall resistance $(R_h \alpha H)$ largely contributes to the effective magnetoresistance.

Figure (4-9) displays the specific LMR of all reported materials depend on inhomogeneity approach, traditional semiconductor[48, 117, 118], semimetal[119, 120, 121, 122, 123] transition-metal dichalcogenide[124] and Topological Insulator[50, 54, 125]. All the values of LMR were extracted from the references at room temperature with applied 5T. Furthermore, although black phosphorus is the most stable allotrope of phosphorus, it may not be as robust in air as other layered materials[126, 127]. This is explaining why the mobility degradation of thinner films and could be overcome by exfoliating and encapsulating few-layer black phosphorus while in an inert atmosphere. However, in our structure h-BN is more stable than BP and can be prepared in the atmosphere environment.

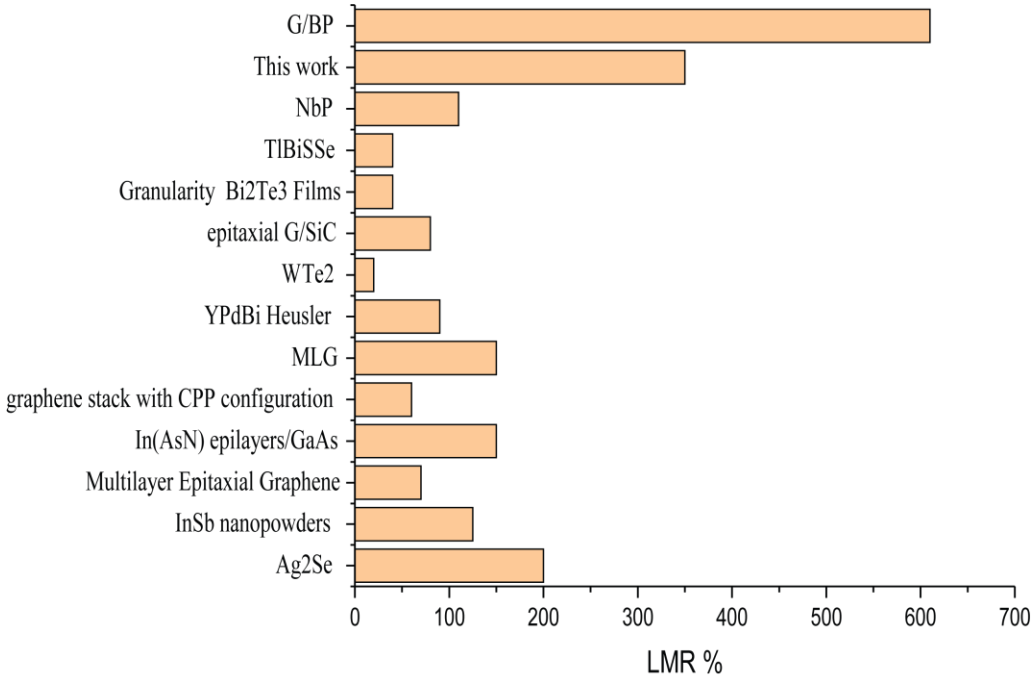

Figure (4-9) displays the LMR for all materials and heterostructures based on the inhomogeneity concept.

References

1. Parish MM, Littlewood PB. Non-saturating magnetoresistance in heavily disordered semiconductors. *Nature* 2003, **426**(6963)**:** 162-165.

2. Sakaki H, Noda T, Hirakawa K, Tanaka M, Matsusue T. Interface roughness scattering in GaAs/AlAs quantum wells. *Applied Physics Letters* 1987, **51**(23)**:** 1934-1936.

3. Jena D. Tunneling Transistors Based on Graphene and 2-D Crystals. *Proceedings of the IEEE* 2013, **101**(7)**:** 1585-1602.

4. Kang J, Cao W, Xie X, Sarkar D, Liu W, Banerjee K. Graphene and beyond-graphene 2D crystals for next-generation green electronics. SPIE Defense + Security; 2014: SPIE; 2014. p. 7.

5. Dean CR, Young AF, MericI, LeeC, WangL, SorgenfreiS, *et al.* Boron nitride substrates for high-quality graphene electronics. *Nat Nano* 2010, **5**(10)**:** 722-726.

6. Haigh SJ, Gholinia A, Jalil R, Romani S, Britnell L, Elias DC, *et al.* Cross-sectional imaging of individual layers and buried interfaces of graphene-based heterostructures and superlattices. *Nat Mater* 2012, **11**(9)**:** 764-767.

7. Andres C-G, Michele B, Rianda M, Vibhor S, Laurens J, Herre SJvdZ, *et al.* Deterministic transfer of two-dimensional materials by all-dry viscoelastic stamping. *2D Materials* 2014, **1**(1)**:** 011002.

8. Shioya H, Russo S, Yamamoto M, Craciun MF, Tarucha S. Electron States of Uniaxially Strained Graphene. *Nano Letters* 2015, **15**(12)**:** 7943-7948.

9. Chen JH, Jang C, Adam S, Fuhrer MS, Williams ED, Ishigami M. Charged-impurity scattering in graphene. *Nat Phys* 2008, **4**(5)**:** 377-381.

10. Ishigami M, Chen JH, Cullen WG, Fuhrer MS, Williams ED. Atomic Structure of Graphene on SiO2. *Nano Letters* 2007, **7**(6)**:** 1643-1648.

11. Ryan B, Luiz Gustavo C, Lukas N. Raman characterization of defects and dopants in graphene. *Journal of Physics: Condensed Matter* 2015, **27**(8)**:** 083002.

12. Shioya H, Craciun MF, Russo S, Yamamoto M, Tarucha S. Straining Graphene Using Thin Film Shrinkage Methods. *Nano Letters* 2014, **14**(3)**:** 1158-1163.

13. Lee JE, Ahn G, Shim J, Lee YS, Ryu S. Optical separation of mechanical strain from charge doping in graphene. *Nat Commun* 2012, **3:** 1024.

14. Neumann C, Reichardt S, Venezuela P, Drogeler M, Banszerus L, Schmitz M, *et al*. Raman spectroscopy as probe of nanometre-scale strain variations in graphene. *Nat Commun* 2015, **6**.

15. Lazzeri M, Mauri F. Nonadiabatic Kohn Anomaly in a Doped Graphene Monolayer. *Physical Review Letters* 2006, **97**(26)**:** 266407.

16. Yankowitz M, Xue J, Cormode D, Sanchez-Yamagishi JD, Watanabe K, Taniguchi T, *et al*. Emergence of superlattice Dirac points in graphene on hexagonal boron nitride. *Nat Phys* 2012, **8**(5)**:** 382-386.

17. Woods CR, Britnell L, Eckmann A, Ma RS, Lu JC, Guo HM, *et al*. Commensurate-incommensurate transition in graphene on hexagonal boron nitride. *Nat Phys* 2014, **10**(6)**:** 451-456.

18. Ponomarenko LA, Gorbachev RV, Yu GL, Elias DC, Jalil R, Patel AA, *et al.* Cloning of Dirac fermions in graphene superlattices. *Nature* 2013, **497**(7451)**:** 594-597.

Chapter 5

Linear magnetoresistance (LMR) from two parallel electrons gases

5.1 Introduction

To optimise and understand the physics process behind the linear response of graphene to magnetic fields, many theories and experiments were devised and carried out. Linear Magnetoresistance (LMR) was studied in epitaxial multilayer graphene[119], chemical vapour deposition grown few-layer graphene[128], single layer of graphene[120] and mosaic-like bilayer graphene [52]. Most of these experiments invoke one of two models for the interpretation of this phenomenon, they are (1) the inhomogeneity model[56] and (2) quantum model [129].

Prompted by the huge demand for MR sensors with a high sensitivity, low energy consumption, low cost and simple fabrication process, a new approach was developed, which maximises the LMR in graphene. The new model builds on the conventional Drude theory, and is based on the difference in mobility between two electrons gases. Equation (4-1), shows the expression that generates the MR in these devices. The full derivation for this equation can be found in section (1.4.2)

$$MR_{\infty} = \frac{\rho_{xx}(\infty) - \rho_{xx}(0)}{\rho_{xx}(0)} = \frac{n_1 n_2}{(n_1 + n_2)^2} \frac{(\mu_1 - \mu_2)^2}{\mu_1 \mu_2} \ldots\ldots (4-1)$$

$$In\ case\ \mu_1 >> \mu_2$$

$$MR_{\infty} = \frac{n_1 n_2}{(n_1 + n_2)^2} \frac{\mu_1}{\mu_2}$$

Based on Eq. 4-1, two different ways can be proposed to probe and maximise the LMR namely by controlling independently the charge carrier mobility and/or the charge carrier density of two distinct conductors. There are many possible practical implementations which would allow the full control over n and μ, of these the simplest would consist of two spatially separated electron gases belonging to distinct graphene transistors. In this case, the two devices can then have either the same back

gate biases, or independent biases which allows to manipulate the Fermi levels independently. With the emergence of stacked heterostructures, a second simple implementation might consist of layered gases of charges separated by an energy barrier. In this thesis, both the aforementioned experimental implementations have been studied and an LMR as high as 100% was observed for two transistors, where the back gates were independently biased, and an LMR of 300% was measured for a stacked mono/bilayer graphene encapsulated in hexagonal boron nitride (h-BN). All of the measurements were performed at room temperature, with magnetic fields of up to 5T. This chapter will describe in detail the set up and measurements of both configurations.

5.2 Case 1: Magnetoresistance in spatially separated electron gases

Two different ways to realize spatially separated electron gases are discussed in this section. The first technique involves etching of a strip from the middle of the active graphene channel resulting in a split-transistor geometry. The second technique involves the fabrication of two separate transistors with the transistors biased by the same back gate or by independent side or top gates.

4.1.1 Magnetoresistance in split-transistor devices

Graphene monolayer was first mechanically exfoliated from bulk crystal on a p-doped Si/SiO_2 substrate which acts as a global back gate. Next, metal electrodes and side gates were patterned by electron beam lithography followed by metal deposition. Finally, a slit was etched in the main graphene channel was divided into two parallel channels of equal width. Consequently, the finished device has a common source and drain electrodes with independently controlled side gates for each of the parallel channels, as is schematically seen in **Figure (5-1)**.

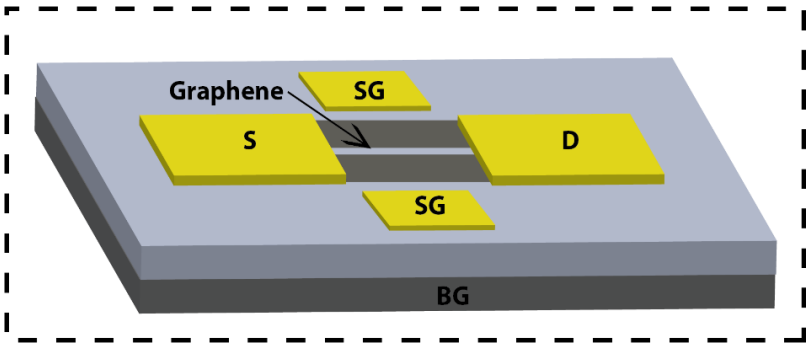

Figure 5- 1 schematics of the first configuration

Figure (5-2) shows the electrical gate dependence of the resistance and the magneto-resistance for the split-transistor configuration. The device exhibits p-doping, with the Dirac point observed at V_{BG} = 58V, as shown in **Figure (5-2a)**. For the magneto-resistance measurements, the Fermi level was fixed at the Dirac point and the magnetic field was varied. When both side-gates are connected to the ground of the circuit, the LMR reaches up to 60% at 5T at room temperature, see **Figure (5-2b)**.

Subsequently, the side-gates were modulated to attain a different conductivity in each sub-channel. First, V_{BG} was fixed to the Dirac point with one side-gate grounded, while the other was set to a finite voltage. The results of the magnetic field sweep, seen in **Figure (5-2c)**, show no significant change in LMR. Next, V_{BG} was fixed to the Dirac point and the two side-gates were set to different biases.

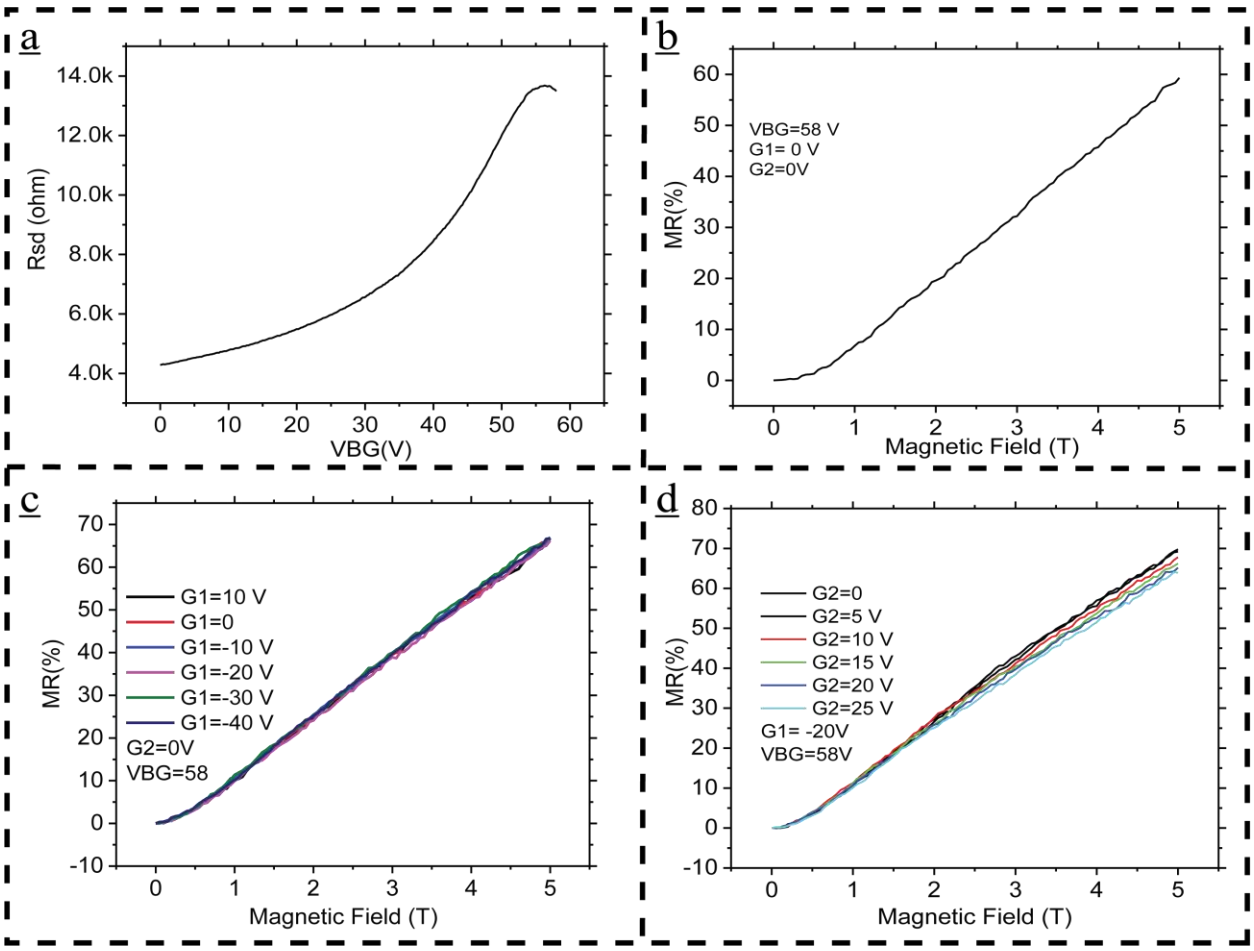

Figure 5- 2 Electrical Properties **a-** The Source- Drain resistance versus the back-gate voltage when both sides gates are zero. **b-** Magnetoresistance at Dirac point for case (a). **c-** MR when one of the side gate is zero while the other is biased steps **d-** Same as c but the side gate is fixed at finite voltage.

No obvious improvement of the value of LMR was observed, suggesting that this experimental implementation does not allow to attain a large difference in the charge carrier mobility between the sub-channels.

4.1.2 Magnetoresistance of two transistors in parallel

Two independent transistors are fabricated on either the same or on different substrates. When fabricated on the same substrate, one transistor consists of a monolayer channel and the other is a bilayer. When they are fabricated on two different substrates, both transistors consist of a monolayer channel. The table below shows the dependence of the density of states and the position of the Fermi Energy on n for monolayer graphene and for graphene of two or more layers.

	Monolayer	Two or more layers
Density of states	$D(E_F) = \frac{2E_F}{\pi(\hbar v_F)^2}$	$D(E_F) = \frac{2m^*}{\pi\hbar^2}$
Fermi Energy	$E_F = \hbar v_F k = \hbar v_F \sqrt{\pi n}$	$E_F = \frac{\hbar^2 k^2}{2m} = \frac{\hbar^2 \pi n}{2m^*}$

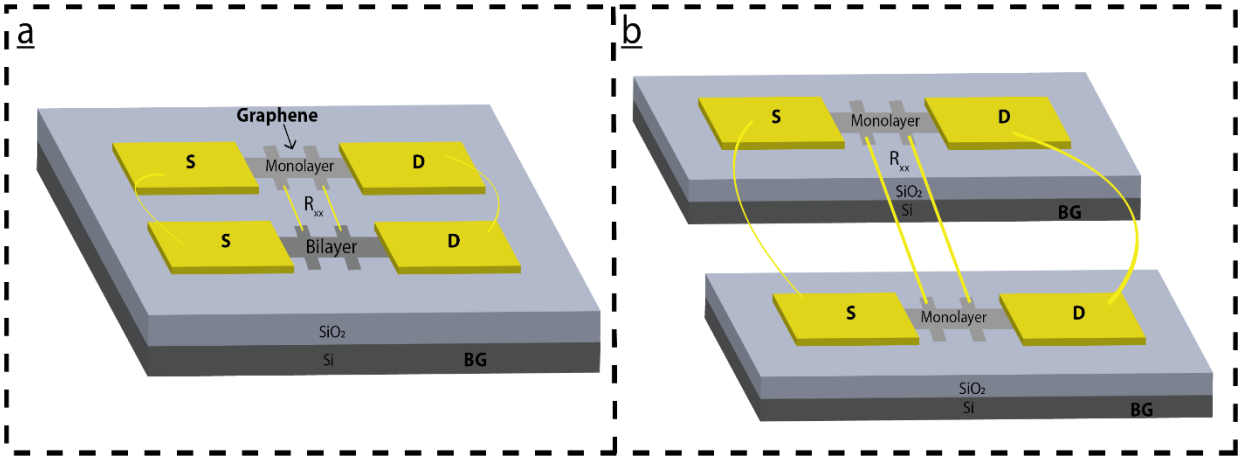

Figure 5- 3 Second configuration **a-** Two transistor on one chip carrier **b-** Two transistors on different chip carriers.

The experimental results for the configuration of two separate transistors with same VBG, where one is a monolayer and the other a bilayer graphene in shown in **Figure**

(5-3a), show small values of MR. **Figure (5-4a)** shows the resistance versus V_{BG} (R-V_{BG} plot) for each individual transistor. The monolayer graphene shows n-type doping in contrast to the bilayer graphene, which shows p-type doping. When both are measured in a parallel configuration, two Dirac peaks corresponding to the two different neutrality points for the single- and bi-layer device are observed in **Figure (5-4b)**.

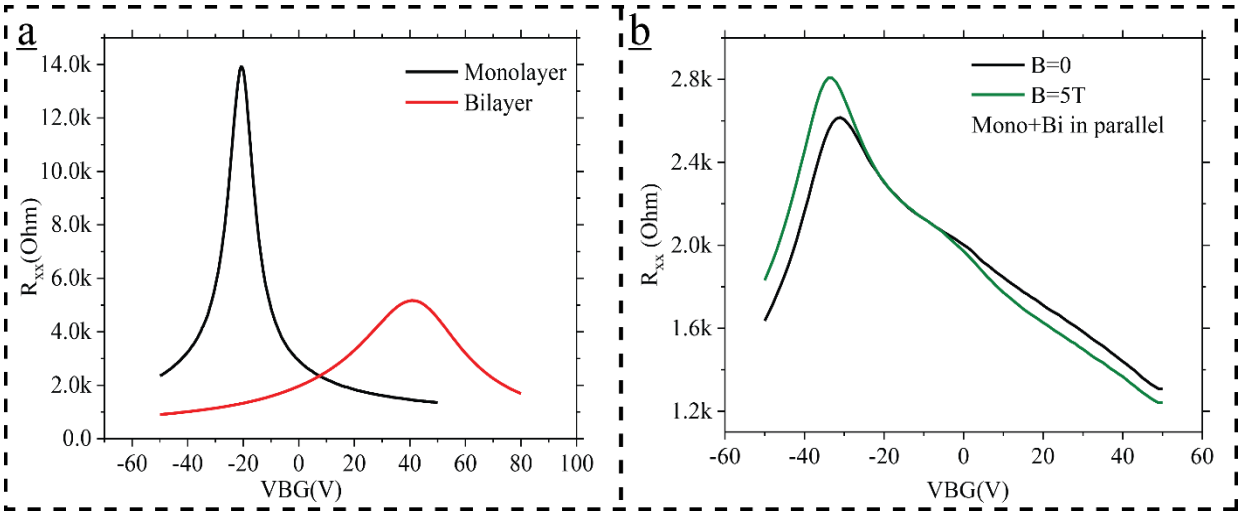

Figure 4- 4 Electrical properties for parallel devices with same V_{BG} **a-** Independent R-V_{BG} for each transistor. **b-** R-V_{BG} for both transistor in parallel without and with existing magnetic field.

As the configuration considered in the previous paragraphs did not yield significant MR, a configuration in which each gate is subjected to independent V_{BG} was fabricated, as is shown in **Figure (5-3b)**. The R-V_{BG} plots for this configuration are shown in **Figure (5-5a)**. Initially, the two transistors were measured independently, and the total resistance for both was calculated as a sum of resistors in parallel, i.e. ($\frac{1}{R_T} = \frac{1}{R1} + \frac{1}{R2}$). Then, both transistors were measured simultaneously with a common-source / common-drain configuration. Both of these measurements are

shown in **Figure (5-5a)**. Subsequently, the full range of MR for this configuration was probed by independently sweeping the two side gates, i.e. $V_{BG(1)}$ and $V_{BG(2)}$. **Figure (5-5)** compares the measured resistance at zero (panels (c)) and finite (panel (d)) values of external magnetic field applied perpendicular to the plane of graphene.

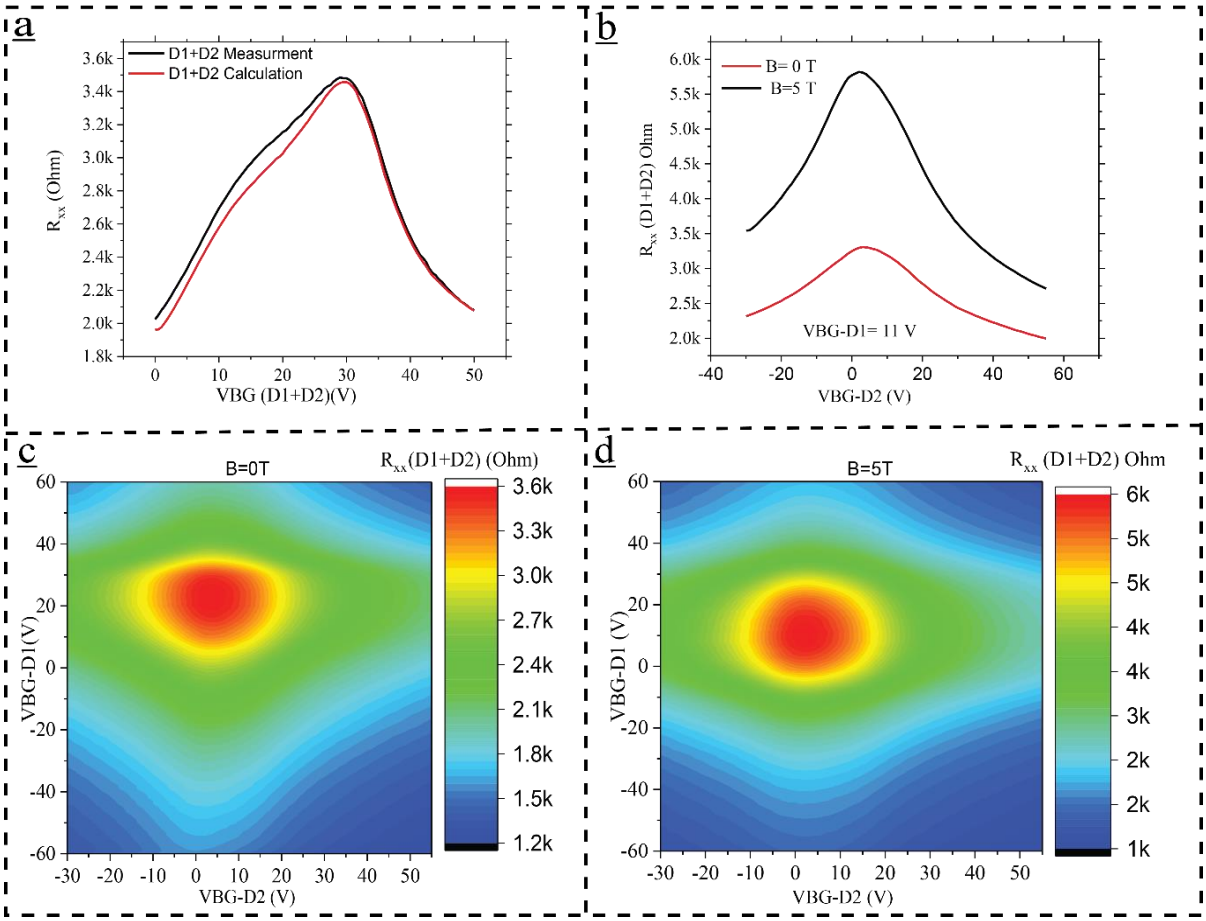

Figure 5- 5 Electrical properties for parallel devices with different V_{BG} **a-** Calculated (black) and measured (red) plots of the total R-V_{BG} for the system. **b-** R-V_{BG} for a single sweep at selected B. (**c-d**) Colour map for the resistance in the absence and presence of the magnetic field (zero and 5T).

The obtained MR are comparable to those obtained for the previous configuration. The highest measured MR is shown in **Figure (5-5b)**, where the values of $V_{BG(2)}$ are swept while $V_{BG(1)}$ remains fixed. The observed small values of MR are attributed to the low charge carrier mobility in both channels.

To address this issue, graphene transistors were fabricated using h-BN as a surface passivation layer for one of the transistors.

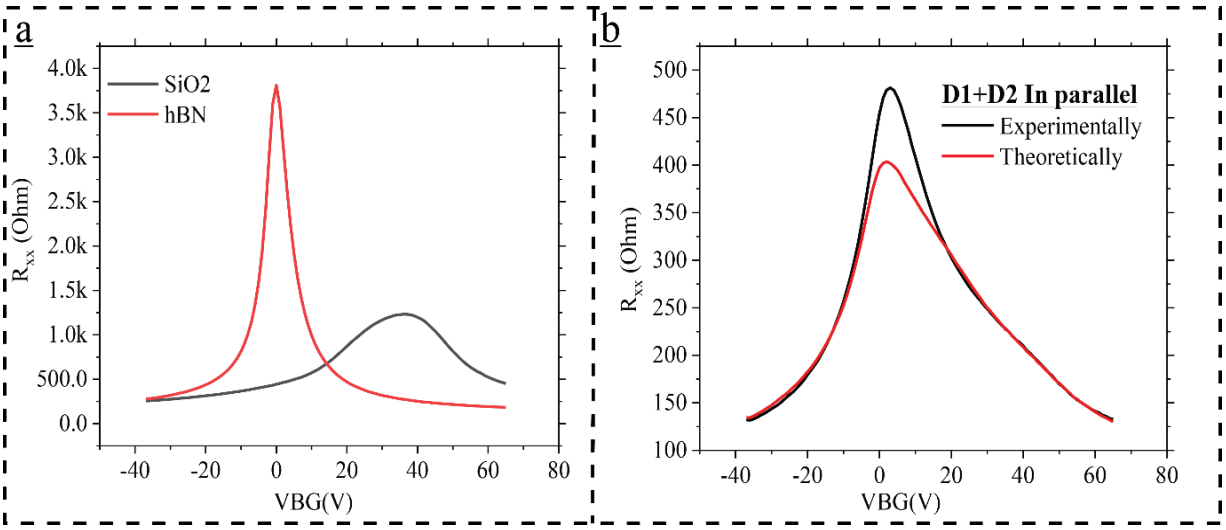

Figure 5- 6 Electrical properties for parallel gases with different VBG, one on SiO_2 and the other on hBN **a-** RVG independently for the transistor on hBN (red line) and SiO_2 (black line). **b-** RVG dependence when both are connected in parallel (black line), the redline for the theoretical calculation.

Figure (5-6) shows the R-V_{BG} traces for each of the transistors in panel (a) and for the total resistance in panel (b). **Figure (5-6a)** reveals that the two transistors significantly differ in their charge transport characteristics. The transistor fabricated on h-BN has a higher mobility than the one on SiO_2. In **Figure (5-6b)**, VBG (1) and VBG(2) are swept simultaneously while the transistor operates in a common-source / common-drain mode. The experimental results are plotted in black, while the theoretical calculation, which is in good agreement with the measurements, is shown in red. The independent MR for each of the transistors was recorded as well, and is plotted in **Figure (5-7a)**. The transistor with larger values of charge carrier mobility is found to exhibit larger magneto-resistance. **Figure (5-7 c and d)** show colour coded plots of the MR as a function of the two gates. The red coloured area

represents the Dirac point, where the Fermi surface shrinks into a point. In this regime. From these detailed gate-maps of the MR, one can identify the gate combination that yields the highest sensitivity to magnetic fields. Once the optimum values of gate bias have been identified, the LMR is studied and values up to 110% have been reported at room temperature, see **Figure (5-7b)**.

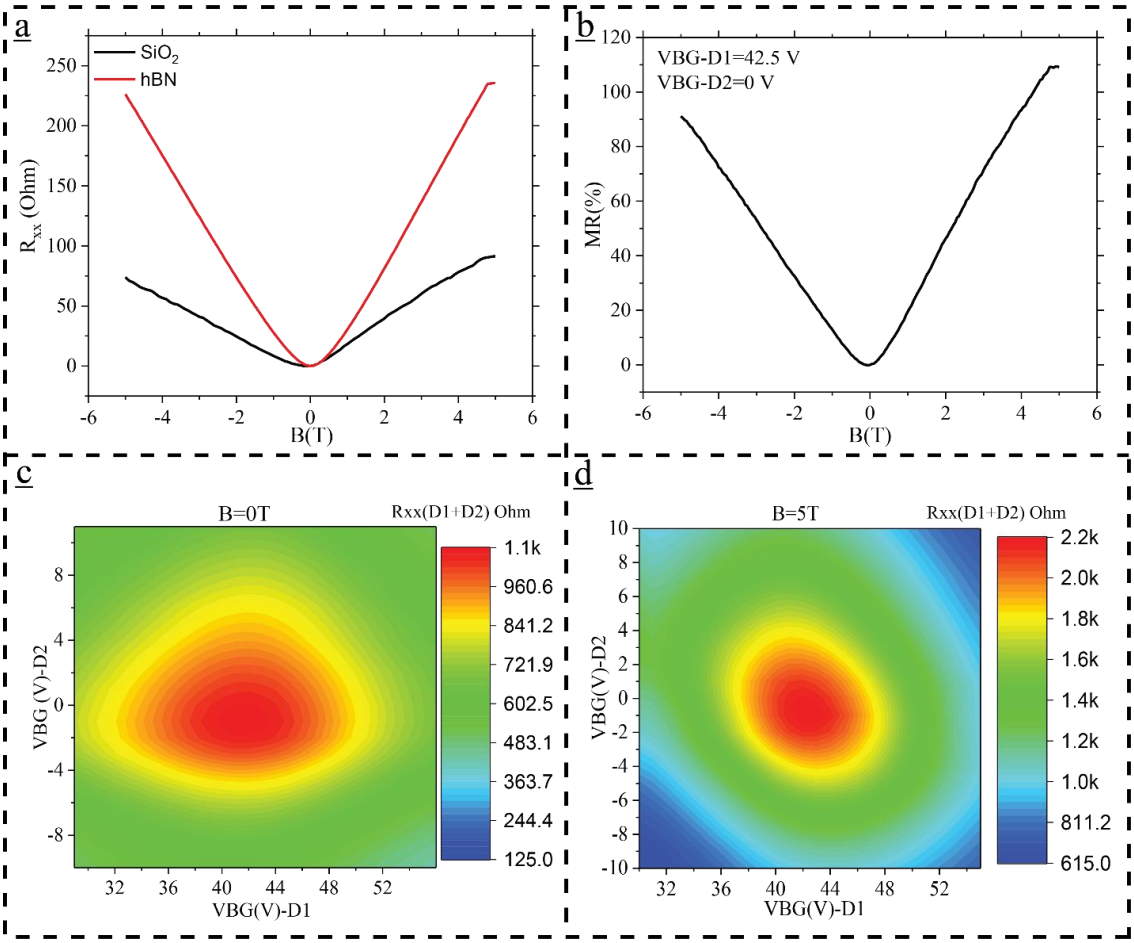

Figure 5- 7 Magnetoresistance for parallel gases with different V_{BG} one on SiO_2 and the other on h-BN **a-** MR for individual transistor, one on SiO_2 and the other on h-BN. **b-** LMR for the gates showing highest resistance change with magnetic field LMR. **c-** and **d-** 2D map for the resistance with and without perpendicular magnetic field.

5.3 Case 2: Stacked graphene devices

In this section a stacked configuration of graphene layers leading to the observation of LMR is presented. At first a layer sequence of four systems was considered, this consisted of h-BN, monolayer graphene, h-BN that partially covers the monolayer graphene and a final bilayer graphene on top which is in electrical contact to the single layer graphene at two ends of the flake, see **Figure (5-8c)**. In this structure, the monolayer graphene is expected to have a very high conductivity because it is encapsulated in hBN. The measured conductivity as a function of V_{BG} for this configuration is shown in **Figure (5-8a)**. The figure shows two different traces, the first (in black) is the total conductivity measured in Region A (**see Figure 5-8d**), and the second (in red) is the top bilayer alone, measured in Region B. The two traces exhibit the same qualitative characteristics with the combined (total) conductivity producing higher values, as can be expected.

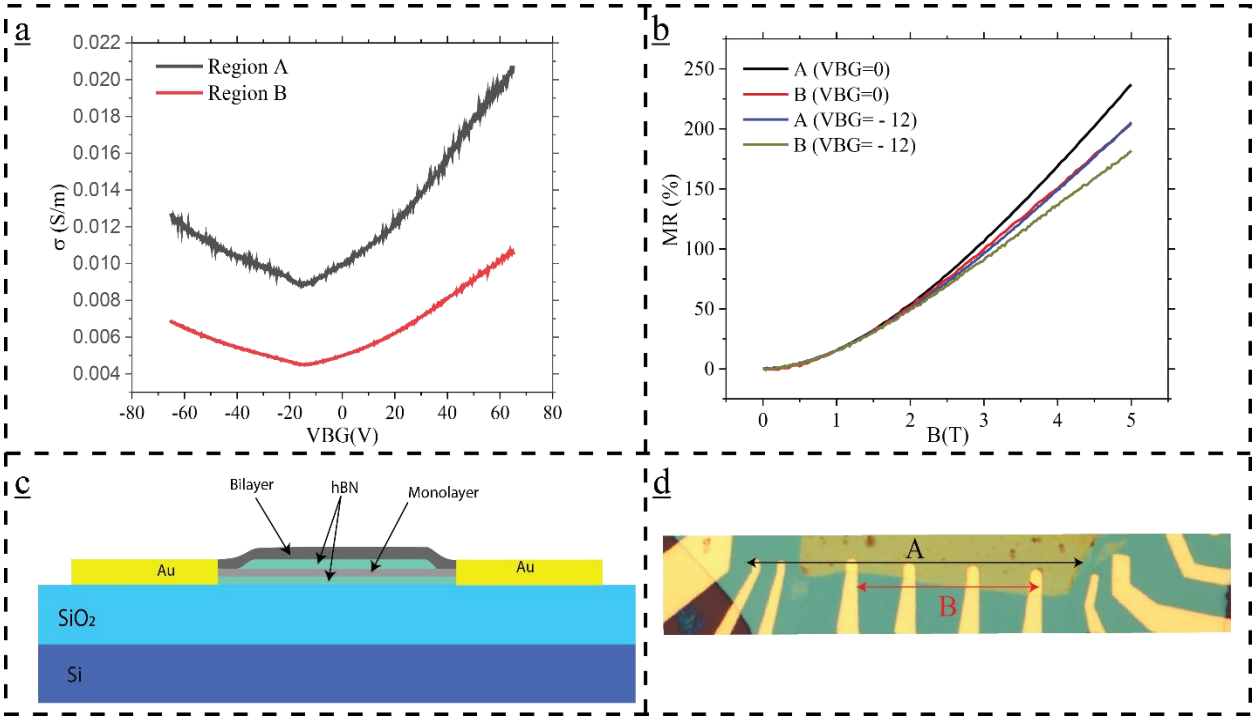

Figure 5-8 Electrical properties and schematic structure for two overlapping electron gases at the ends **a-** the conductivities for Region A and B, as shown in (d). **b-** MR for the two regions at CNP and VBG=-12V. **c-** Side view of the two parallel gases, shorted at end. **d-** Optical image of the device.

The MR for the different regions show a parabolic behaviour at low fields (< 2T), which evolves into a linear dependence at higher fields (> 2T), see **Figure (5-8b)**. The MR reaches up to 240% in Region A and 200% in Region B. This difference can be attributed to the parallel transport in the single layer graphene becoming predominant at high magnetic field.

The other configuration consists of a three layers stack, produced by dry transfer. In this case, an h-BN passivation layer is exfoliated on SiO_2, this is then covered by a graphene monolayer and a graphene bilayer on top of it. **Figure (5-9c)** illustrates schematically the heterostructure of this device. The R-V_{BG} for this heterostructure is shown in **Figure (5-9a)** at room temperature, and the room temperature MR is

shown in **Figure (5-9b)**. In this device, the LMR was found to be three times bigger than in the previous configurations, reaching up to 280% at 5T.

The physical origin of the observed improvement in LMR is the encapsulated monolayer located between the bilayer and the h-BN. This is a better conductor than the bilayer, and at large values of magnetic field will tend to shorten the transport in the structure. The LMR, which is parabolic at low magnetic fields (< 0.3T), evolves into a linear dependence at higher fields with no indication of saturation. As V_{BG} is tuned away from the CNP, the LMR percentage decreases. We conclude that the large mobility difference in the two channels is the origin of the large observed MR, which is in agreement with the model[51].

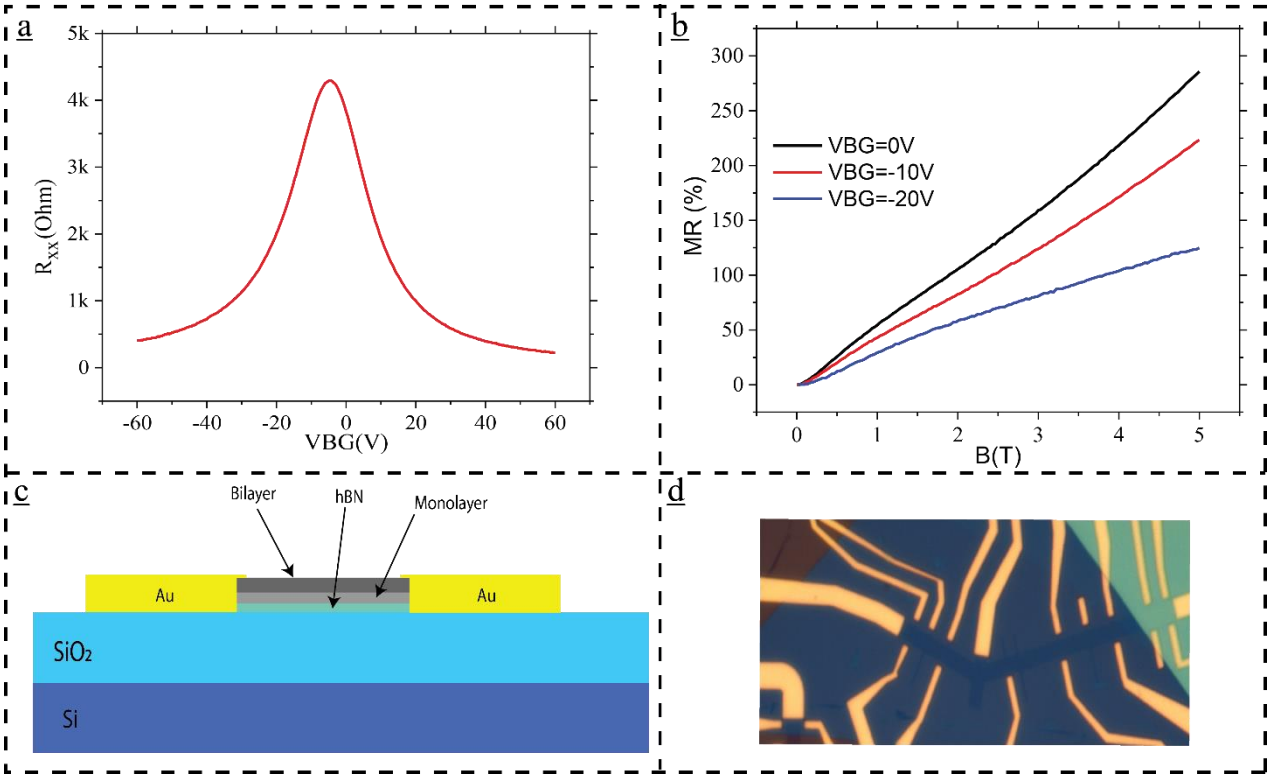

Figure 5-9 Electrical properties and schematic structure for two overlapping electron gases through the channel **a-** R-V_{BG} for the device. **b-** Magnetoresistance of this configuration at different V_{BG}s. **c-** The side view schematics of the two overlapping parallel electron gases. **d-** Optical image of the device

5.4 Summary

Magnetoresistance in nonmagnetic materials is a sensitive tool to study the effects of magnetic fields on its charge transport. Here, we have focused on the mobility of charge carriers to modify the transport. A variety of configurations was used to probe and increase the MR, with a specific aim of achieving high LMR values. These configurations were based on different parallel electron gas concepts. The designs were grouped into two main types: one, in which the two parallel electron gases are spatially separated; and a second, where the electron gases overlap. In the devices of the first type we observed up to 100% MR at room temperature by applying a magnetic field of 5T, whilst in the second type, we succeed to increase the LMR to almost 300%. The results of the LMR recorded in this chapter are summarised in **Figure (5-10)** for all the configurations in which the MR reached more than 100%.

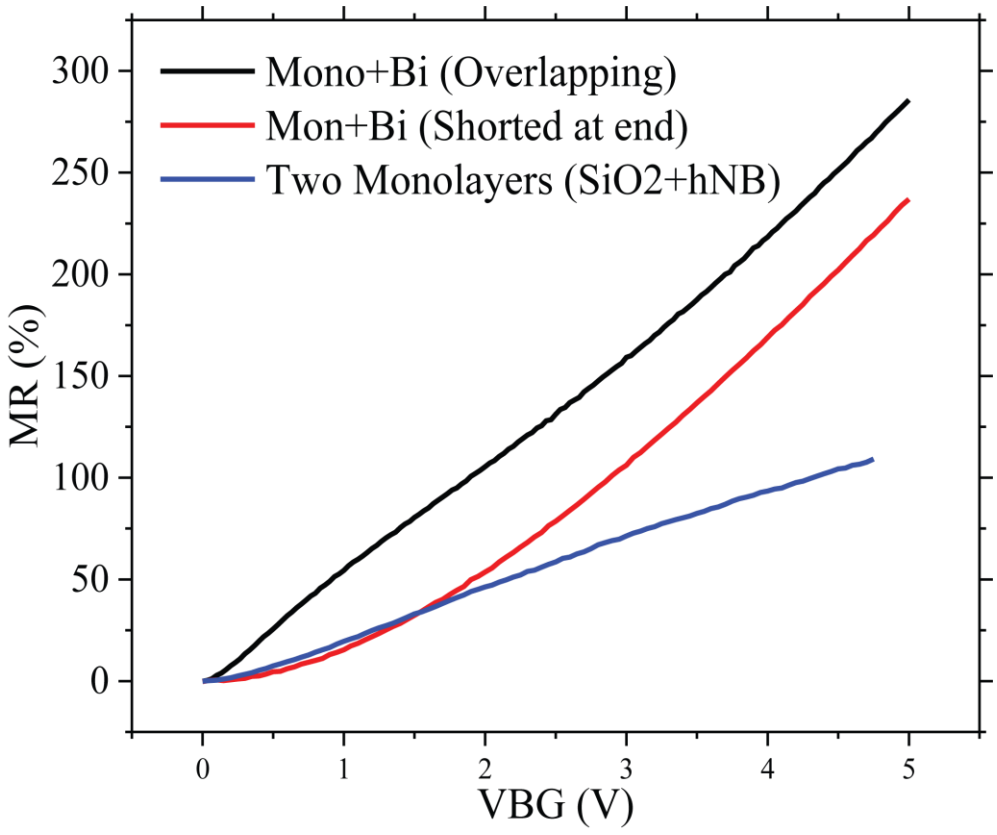

Figure 5- 10 Comparison between different device structures

From **Figure (5-10)**, it is clear that the configuration in which the two electron gases are shorted only at the channels' ends shows a parabolic behaviour at low field, becoming linear at higher fields, while the performance for the device in which the two electron gases are overlapping throughout the channel is nearly linear even for low fields.

We therefore conclude that the main requirement for high MR in these devices is to design devices in which two electron gases with very high mobility can be modulated.

References

1. Friedman AL, Tedesco JL, Campbell PM, Culbertson JC, Aifer E, Perkins FK, *et al.* Quantum Linear Magnetoresistance in Multilayer Epitaxial Graphene. *Nano Letters* 2010, **10**(10)**:** 3962-3965.

2. Liao Z-M, Wu H-C, Kumar S, Duesberg GS, Zhou Y-B, Cross GLW, *et al.* Large Magnetoresistance in Few Layer Graphene Stacks with Current Perpendicular to Plane Geometry. *Advanced Materials* 2012, **24**(14)**:** 1862-1866.

3. Gopinadhan K, Shin YJ, Yudhistira I, Niu J, Yang H. Giant magnetoresistance in single-layer graphene flakes with a gate-voltage-tunable weak antilocalization. *Physical Review B* 2013, **88**(19)**:** 195429.

4. Kisslinger F, Ott C, Heide C, Kampert E, Butz B, Spiecker E, *et al.* Linear magnetoresistance in mosaic-like bilayer graphene. *Nat Phys* 2015, **advance online publication**.

5. Parish MM, Littlewood PB. Non-saturating magnetoresistance in heavily disordered semiconductors. *Nature* 2003, **426**(6963)**:** 162-165.

6. Abrikosov AA. Quantum magnetoresistance. *Physical Review B* 1998, **58**(5)**:** 2788-2794.

7. Gopinadhan K, Shin YJ, Jalil R, Venkatesan T, Geim AK, Neto AHC, *et al.* Extremely large magnetoresistance in few-layer graphene/boron-nitride heterostructures. *Nat Commun* 2015, **6**.

Chapter 6

Ionic Polymer gating

6.1 Introduction

The electrostatic modulation of the charge carriers in Field Effect Transistor devices based on a conductive channel of graphene (FETG) exfoliated on a p-doped Si/SiO2 substrate is attained by an applied voltage to the doped-Si substrate. In such structures, the breakdown electric field of SiO_2 limits the maximum values of charge carrier accumulation that can be accumulated in the single layer of carbon atoms to $<10^{14}$ cm^{-2}. At the same time, charged trap states present in the SiO_2 dielectric layer are a well-established source of scattering for the charges in graphene which ultimately hinders the electrical transport in this single layer of carbon atoms. Alternative methods for the implementation of an efficient electrostatic gating which do not suffer from the aforementioned limitations inherent to SiO_2 are the focus of a wide scientific research. Air gap graphene transistors with bridge gates have been shown to exhibit record high charge carrier mobility by eliminating any charge trap states[130, 131]. However, in these suspended structures the maximum level of doping that can be reproducibly attained is $<10^{13}$ cm^{-2} due to strong electrostatic forces pulling on the graphene membrane and causing its collapse. One way to overcome this limitation and enable the study of the physical properties of graphene in the so-called high doping regime (i.e. $>10^{14}$ cm^{-2}) is to exploit liquid electrolyte gating. In the electrolyte, mobile ions suspended in a polymer or liquid matrix can re-distribute themselves after applying a voltage, forming an electrostatic double layer (EDL) at the interface between graphene and the electrolytic solution, called the Debye layer. Based on the ion concentration, the EDL can be only a few nanometers thick. Consequently, the capacitance of the EDL can be much higher than the capacitance of a conventional SiO2 back gate.

This property of the EDL enables much wider tuneability of the Fermi energy in graphene as compared to any other gating technique, while requiring a much lower

operating voltage applied to the reference electrode in the electrolyte than the voltages currently used with dielectric oxide gates and/or suspended air-gap gates.

The high gated voltage gives a much more prominent role to the quantum capacitance of graphene than the back-gate capacitance (geometrical capacitance) [132, 133, 134, 135]. The total equivalent capacitance can be written as

$\frac{1}{C} = \frac{1}{C_G} + \frac{1}{C_Q}$.

The geometrical capacitance C_G is define as $C_G = \varepsilon_0 \varepsilon / d$, d is the thickness of the dielectric, ε_0 and ε are the permittivity of free space and the relative permittivity of the substrate. The quantum capacitance is defined as $C_Q = e^2 D$, where D is the density of states at the Fermi level and in graphene is a strong function of the Fermi energy $E_F = \hbar v_F \sqrt{\pi |n|}$. Therefore, D can be changed by applying a gate voltage: $D(E) = dn/dE$ [136, 137].

This technique provides doping levels much higher than those obtained with the conventional back gate [80, 138]. In addition, the mobile ions in the electrolyte effectively screen charged impurities underneath the graphene benefitting the electrical properties of graphene as compared to other high dielectric environments[139]. All these facts indicate that electrolytic top gating is an interesting solution to explore novel physical regimes in FETs of graphene and transition metal dichalcogenides (TMDs).

6.2 Solid Polymer Electrolyte (SPE)

A polymer is made up of repeated subunits which form long chains. If it hosts salts, it is called a polymer electrolyte. The ions can move in the space provided by the free volume of the polymer host. The solid polymer electrolyte used in this thesis consists of two components: Poly (ethylene oxide) (PEO) and lithium perchlorate ($LiClO_4$). PEO is a polyether compound with a chemical structure of H–(O–CH2–CH2)n–OH, see **Figure (6-1a)**, which was discovered by Wright[140, 141] and has been intensively studied as an electrolyte in dry batteries[142]. Its ethylene oxide (EO) units have a high donor number for Li+ and high chain flexibility, which are important properties for promoting ion transport. $LiClO_4$ is an inorganic salt, as shown in **Figure (6-1b)**, which is easily dissolvable in the polymer. The electrical conductivity for $LiClO_4$/PEO mixture was first studied by Wright[140] and others [143]. Its conducting mechanism involves the segmental motion-assisted diffusion of lithium ions in a PEO matrix. The main restriction of the ions in the polymer is the presence of the crystalline region in the polymer chain, see **Figure (6-1c)**. As a result, many experiments have been done to minimise the crystallinity to improve the conductivity at room temperature[142].

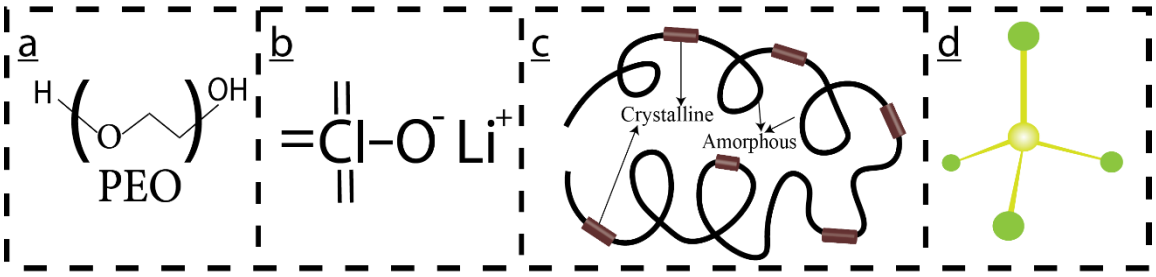

Figure 6-1 Structure of linear PEO **a-** chemical structure **b-** chemical expression. **c-** Morphologies of semi-crystalline PEO. **d-** Tetrahedral structure, class AX4.

The electron configuration for Perchlorate (ClO_4) is Cl= $1s^2$ $2s^2$ $2p^6$ $3s^2$ $3p^5$, O= $1s^2$ $2s^2$ $2p^4$, meaning that it has 32 valence electrons, (7+6*(4) +1) =32. It is a monovalent anion and has tetrahedral structure, class AX4, see **Figure (6-1d)**. Li has one valance electron, Li= $1s^2$ $2s^1$. It is a monovalent cation, see **Figure (5-1d)**. The lithium atom size is smaller than the C-C atom distance in Graphene which is about 1.42*A*°, therefore Li has the ability to sit in between the C-C atoms.

6.3 Electrolyte gated graphene FET

Usually in FETs the transport of charge carriers in the active channel is manipulated by the back-gate electrode. The common back-gate electrode is a heavily doped Si coated by a few hundred nanometers thick SiO_2 dielectric. This substrate has been widely used for the characterization of charge transport in graphene and TMDs. However, the charge carrier mobility measured in atomically thin transistors fabricated on SiO_2 is limited by scattering from charged surface states and impurities[14, 19, 27] substrate surface roughness[100, 112] and SiO2 surface optical phonons[19].

For example, in the case of graphene theory predicts that the intrinsic charge carrier mobility can reach up to 4 x 10^4 cm^2 V^{-1} s^{-1} at room temperature [19]. However, this value cannot be achieved on standard SiO_2 substrates owing to the aforementioned scattering sources. More specifically, charged impurities around and underneath the graphene on SiO_2 are responsible for long-range scattering due to the Coulomb potential introduced by their charged state. Another source of scattering is known as short-range. This is generated by atomic defects/ripples. The graphene sheet on SiO_2 partially conforms to the underlying substrate which is not flat[112]. The negative action by some of these sources of scattering can attenuated with the use of electrolyte gating *via* ionic screening distribution[144]. In this case, the redistribution of the ions in the electrolyte can efficiently screen charged impurities[104, 145], such as

Coulomb impurities. Ions reduce (compensate) the electrostatic potential fluctuation due to random distribution of the impurity charges on the surface of the substrate[104, 146]. Therefore, the polymer electrolyte can be used as top gate (TG) in an alternative strategy to the traditional back-gate.

Researchers have shown that a solid-state polymer electrolyte consisting of a Li ($LiClO_4$) dissolved in poly (ethylene oxide) (PEO) can be used as a top gate[80, 147]. With this polymer electrolyte it is possible to attain exceptionally large values of gate capacitance[101] >10 μF cm^{-2} owing to the formation of an EDL separated approximately by 1 nm from graphene. This is an important aspect in order to facilitate the fabrication of low-voltage circuitry and on flexible substrates. With this consideration, FETs were prepared, and the connection schematic of the device is shown in **Figure (6-2a)**. The sheet conductivity (σ) as a function of the voltage back-gated (V_{BG}) for a representative graphene transistor before and after encapsulation in electrolyte polymer are shown in **Figure (6-2b)**.

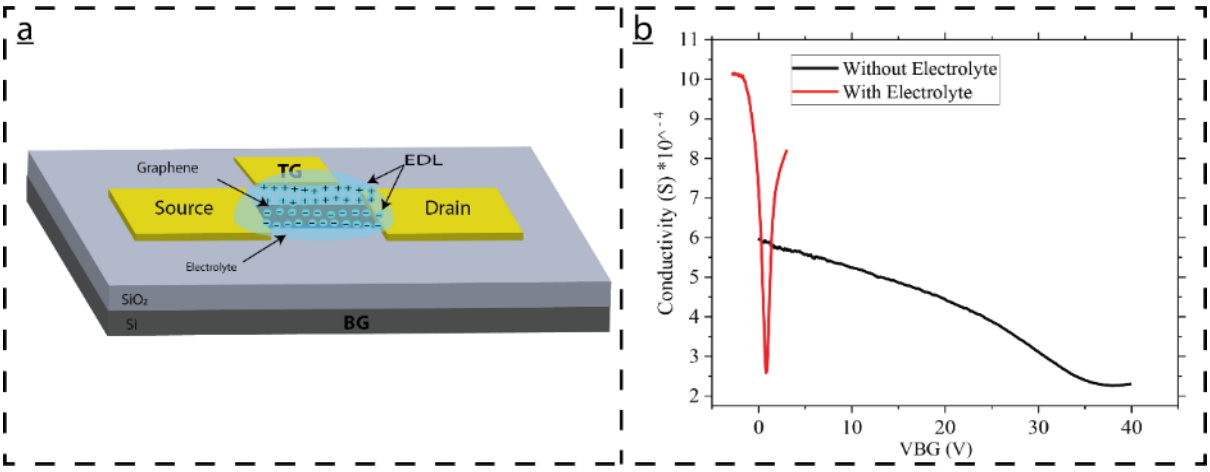

Figure 6- 2 Field effect transistor with top gate **a-** The schematic of the transistor. **b-** Conductivity (σ) versus voltage back gate (VBG).

It is apparent that electrolyte polymer increases dramatically the back-gate capacitance. Due to the large interfacial capacitance arising from a nearby layer of counter ions, it is possible to obtain a large and reversible modulation in graphene resistance with the application of small voltages. Covering graphene with a top dielectric causes an increase in the gate capacitance by up to two orders of magnitude. This capacitance change has a profound effect on the change of the electrical transport. The gate capacitance does not significantly depend on the ionic concentration and it appears to depend on the dielectric constant of the medium[103, 139].

To understand the role of the polymer electrolyte, it is necessary to compare the charge carrier concentration (n) modulated in a monolayer graphene upon sweeping just the back gate, before and after encapsulating the transistor with a polymer electrolyte. The values of charge density were extracted in two independent ways using (1) a parallel plate capacitor model (n_{FET}) and (2) a measurement of the Hall coefficient (n_{Hall}) as outlined in the equations:

$$n_{FET} = \frac{\varepsilon_o \varepsilon_{ox} V_{BG}}{de} = 7.3 * 10^{10} * V_{BG} \quad cm^{-2}V^{-1}$$

$$n_{Hall} = \frac{I}{e}\frac{dB}{dV_H}$$

where I is the bias current, d and ε_{ox} are the thickness and permittivity of SiO2, respectively; ε_0 is the permittivity for free space, B is the applied magnetic field, V_H is the Hall voltage.

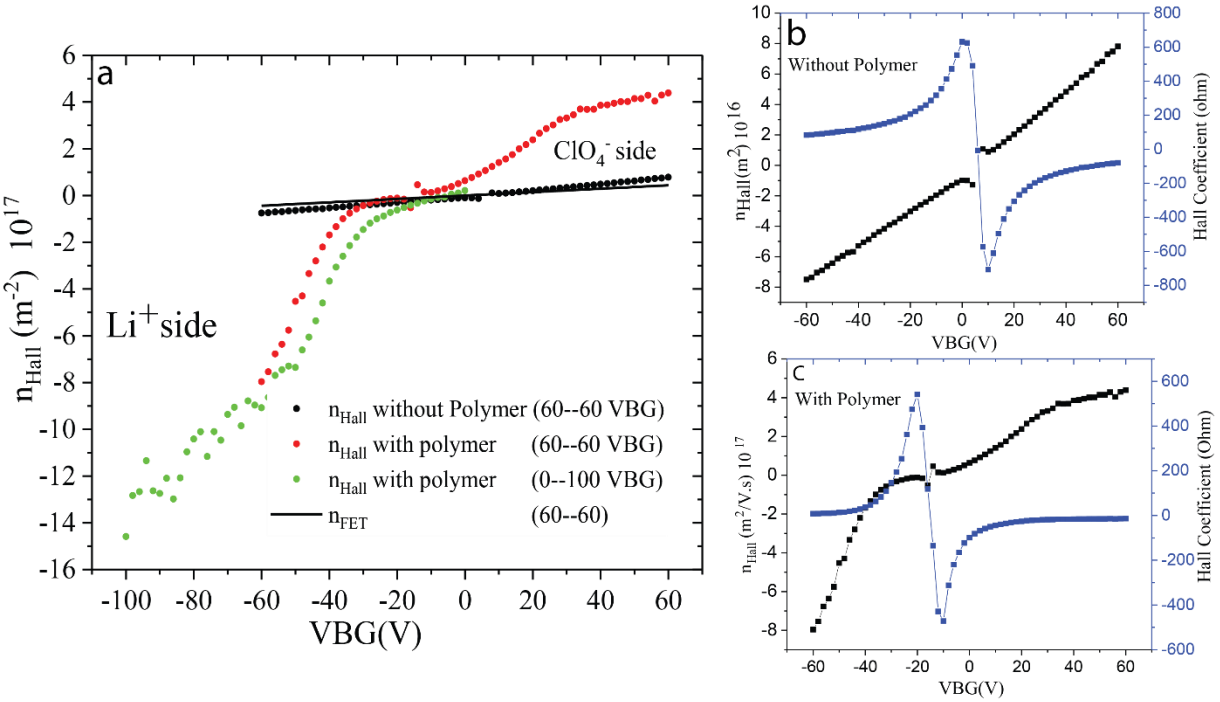

Figure 6- 3 the comparison of charge carrier concertation with and without polymer **a-** the charge carrier concentration (n), the values of (n) extracted depend on the Drude and Hall model. **b-** and **c-** Hall coefficient when the graphene is uncovered and covered by electrolyte.

Figure (6-3a) shows the charge carrier concentration of monolayer graphene as a function of V_{BG}. Both n_{FET} and n_{Hall} display a linear dependence on V_{BG} when there is no electrolyte polymer. However, upon encapsulation by the electrolyte, the modulation of the charge density is no longer linear in gate voltage. The observed asymmetries between the positive and negative bias applied to the gate are attributed to the different size of the ions forming the EDLs for the two polarities. In the presence of the EDL the capacitance depends strongly on V_G. The total capacitance (C) characterised experimentally is given by ($\frac{1}{C} = \frac{1}{C_g} + \frac{1}{C_Q}$); where C_g and C_Q are the geometrical capacitance and quantum capacitance. The C_g is less dominant

because the Si is separated from the graphene by hundreds of nanometers, while C_Q comes from the EDL which is just a few nano-meters away from the graphene. Therefore, the value of C_Q dominates the total capacitance. This explains the observation that the position of the Fermi energy E_F can be tuned over large values with the application of small bias to the back gate.

6.4 Ionic polymer as a screen to improve time response

The alternative strategy to the conventional back gate (Si/SiO_2) is using a solid-state polymer electrolyte, which has improved the performance of Graphene FETs (i.e charge transport and reach high charge concentration) [104, 146, 148]. Electrolyte gating is also highly promising for TMD-based switching devices[149, 150, 151], with almost ideal transport characteristics at low operating gate voltage. The improvement in the performance of these transistors is triggered by a reduction of the contact resistance and an enhancement of the channel charge carrier mobility due to the suppression of Coulomb scattering as well as a modification of the phonon dispersion[149]. These factors lead to very steep subthreshold slopes for both electrons and holes and extremely low OFF-state currents.

The role of the Polymer electrolyte was also investigated in TMDs photodetector devices [152, 153, 154]. To date, a wide range of atomically thin photodetectors have been developed and studied both experimentally and theoretically. These studies have highlighted the detrimental influence of charge trap states on the photocurrent generation, especially in photoconductance (PC) and photogating (PG). Typically, trap states are located at the $TMDs/SiO_2$ interface or on the surface of TMDs and they have long-lifetime which suppresses the time response of light-sensitive electronic devices[155]. To avoid this issue, TMDs were encapsulated between two

layers of graphene, as heterostructure devices [156, 157, 158] . In such a hybrid structure, the photogenerated charge carriers are transferred to graphene *via* electrostatic bending of the conduction and valence bands at the TMD/graphene interface. The recombination time ($\tau_{lifetime}$) in TMDs should be longer than the transit time ($\tau_{transit}$) of the carrier through graphene to allow efficient collection of photogenerated charge carriers. However, charged adsorbates on the surface of the atomically thin materials which are then trapped between the stacked layers was found to inhibit the charge transport and reduce the photo-response[108]. Presently, a wide research effort is focussed on finding ways to enhance the time response of atomically thin photodetectors. Isolating the TMDs from the surrounding environment by encapsulation in a dielectric such as HfO_2[158] has boosted the responsivity up to 10^4 A/W due to the removal of atmospheric adsorbates from the surface of the TMDs. However, large values of back-gate bias pulses are needed to reverse any electric potential gradient at the TMD/graphene interface, allowing trapped charge carriers to recombine[157, 159].

In this chapter, an alternative method for enhancing the performance of atomically thin photodetectors is presented. This is based on the encapsulation of layered structures in an ionic electrolyte, which has been found to significantly improve the time operational bandwidth and responsivity of the photodetector up to 1.5 kHz and $10^6\ AW^{-1}$ respectively [76]. The studied structure consists of a van der Waals stack of WS_2 -exfoliated on a Si/SiO_2 (300nm) substrate- covered by a single layer of graphene. The system is then covered by ionic-polymer, as shown in **Figure (6-4a)**. The graphene used in these devices is of high quality and synthesised via chemical vapour deposition (CVD-graphene) as detailed in Ref.[68] . Electrical contact to WS2 and graphene are realized by standard electron-beam lithography followed by electron-beam evaporation of a Cr adhesion layer (5nm) and Au (50 nm) and a lift-

off process in acetone. Subsequently, conductive graphene channels of widths ranging from 3 to 10 μm and lengths 1–12 μm were defined by means of O_2 plasma etching. In the final step, the structure was covered by a transparent ionic polymer, lithium perchlorate/poly (ethylene oxide) LiClO4/PEO, (8:1) in methanol, which served as a top gate. The ionic-polymer plays the major role in improving the device responsivity. The key motivation behind its use is the ability to accumulate a very high carrier density in a graphene channel (~ 10^{14} cm^2 V^{-1} s^{-1}) and at the same time the highly mobile ions can efficiently screen the potential of charged impurities. Another advantage of the ionic polymer is that it requires a very small operating voltage compared to the conventional metal-oxide gate structures.

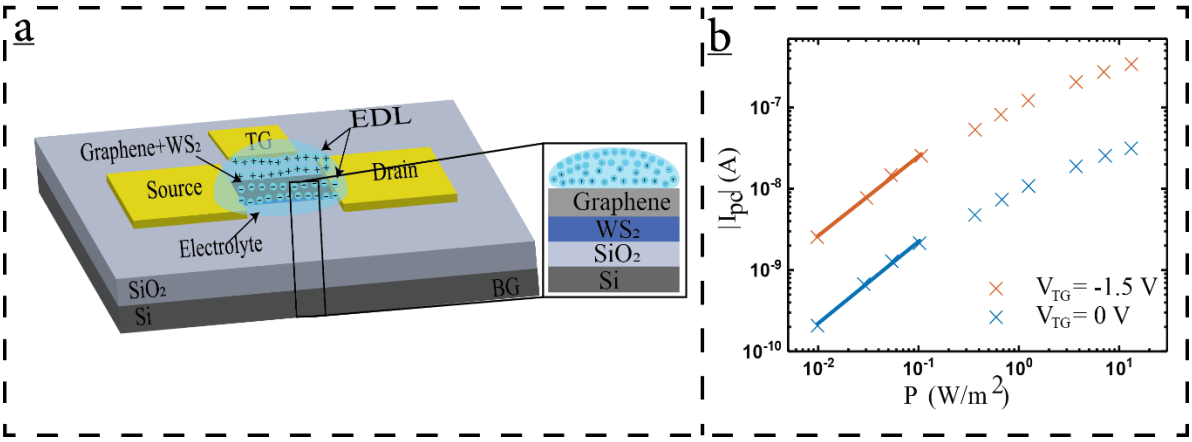

Figure 6- 4 Device structure and photocurrent **a-** The schematic with principal layers shown. **b-** Photocurrent (I_{pc}) versus incident powers (P) without and with biasing the gate.

At first the photocurrent in these devices was characterised under vacuum condition in order to avoid electrochemical reactions of the ionic polymer with moisture in the air during device operation. The device was illuminated with monochromatic light (λ=625 nm) of varying intensity whilst recording the photocurrent signals. **Figure (6-4b)** shows that upon biasing the top gate voltage (V_{gs}) the photocurrent (I_{pc})

increases for all incident optical powers. A maximum photocurrent of 339 nA is recorded for an incident power density of approximately 15 W m^{-2}, which reduces to 2.55 nA at the lowest detectable illumination levels ($V_{gs} = -1.5$ V, $V_{ds} = 100$ mV).

A measurement of the photocurrent as a function of the incident optical power can be used to unveil the microscopic origin of the photoresponse in these structures. More specifically, the observed largely nonlinear dependence suggests the presence of a photogating effect[58, 159, 160], which is generally known to lead to a sublinear increase of photocurrent as a function of incident optical power. In the structures presented in this thesis, the semiconducting WS_2 absorbs photons followed by the creation of electron-hole pairs which are subsequently split due to the built-in electric field at the interface between graphene and WS_2. At this point, one charge carrier is transferred to graphene and the other remains in WS_2, as shown schematically in **Figure (6-5a)**. The built-in electrical field is generated by the difference in work functions between graphene and WS_2. At large photon fluence, the built-in field is reduced due to a large number of photogenerated carriers accumulated at the interface generating an opposing electric field leading to a non-linear photoresponse [157, 159, 161].

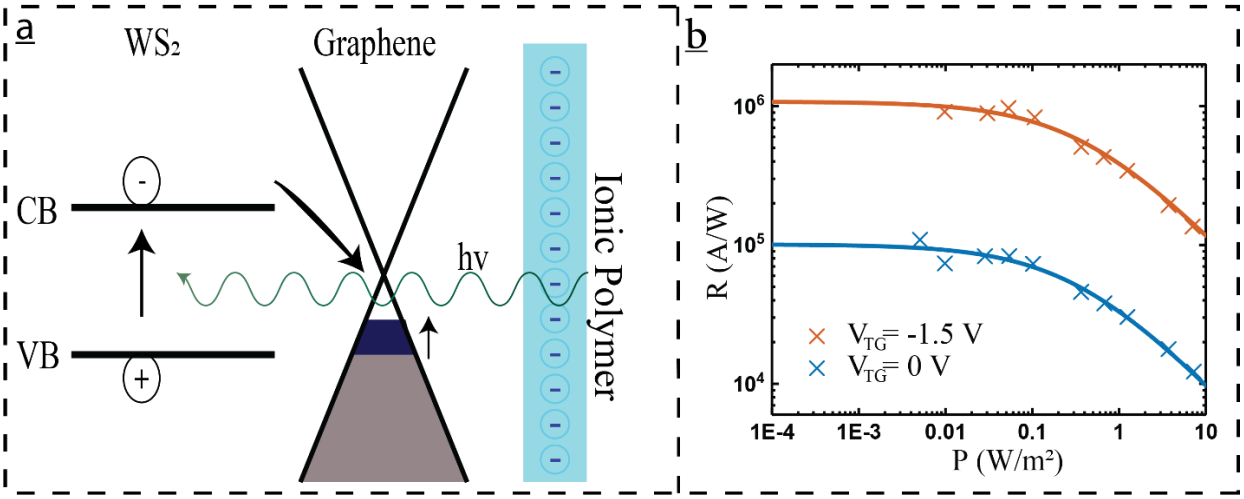

Figure 6- 5 band diagram of the structure and its responsivity **a-** energy level diagram of graphene/WS_2 illustrating the transfer of the charges at the interface. **b-** the responsivity as a function of incident optical power (P) at $V_{dc} = 100\ mV$.

The responsivity of these WS2/graphene structures as a function of incident optical power for both V_{gs}=0V and V_{gs}=-1.5 V are shown in **Figure (6-5b)**. Responsivity is calculated as:

$$R = I_{PC}/P_{opt} \qquad (1)$$

where I_{PC} is the photocurrent and P_{opt} is the incident optical power.

In these structures, the responsivities reach up to 1×10^6 A W^{-1} at $V_{gs} = -1.5$ V for V_{ds} = 100 mV, an order of magnitude higher than that without a bias applied to the top gate, corresponding to an external quantum efficiency of 2.0×10^6. The photo gain can be expressed as

$$G_{th} = \Delta n \times \mu \times V_{ds}/(L^2 \Phi) \qquad (2)$$

where Δn is the number of photoexcited electron–hole pairs and manifests itself as a shift in the Dirac point (ΔV_{gs}) of the graphene FET. Δn could be calculated using the steps outlined in reference[80] leading to the equation

$$V_{gs} = 1.16 \times 10^{-7}\sqrt{n} + 7.23 \times 10^{-14} n \qquad (3)$$

$\Delta n = 1.3 \times 10^{12} cm^{-1}$ which can be solved numerically around V_{gs}=2V using ΔV_{gs}=114mV. The highest photo-gain in these structures is found to be $G_{th} = 4.8 \times 10^{6}$, which is in excellent agreement with the experimental measurement of responsivity (**Figure 6-4b**).

The time response of this photodetector is characterized by fast electronic measurements across on/off light illumination transients. **Figure (6-6 a and b)** shows the time domain response for the same device before and after being encapsulated with ionic polymer. The rise and fall times are defined as the time period taken for ΔI_{pc} to change from 10% (90%) to 90% (10%) of its maximum value, respectively. In other words, the time response is defined as the time required for the transient output signal to reach 0.707 of the total change in photocurrent. The transient response occurs over sub-millisecond timescales with $\tau_{rise} = 130\ \mu s$ and $\tau_{fall} = 440\ \mu s$ with ionic polymer, which is much faster than without ionic polymer, <1s. Such a dramatic improvement is due to the effective screening of so-called long-lived charge trap states by the ionic polymer.

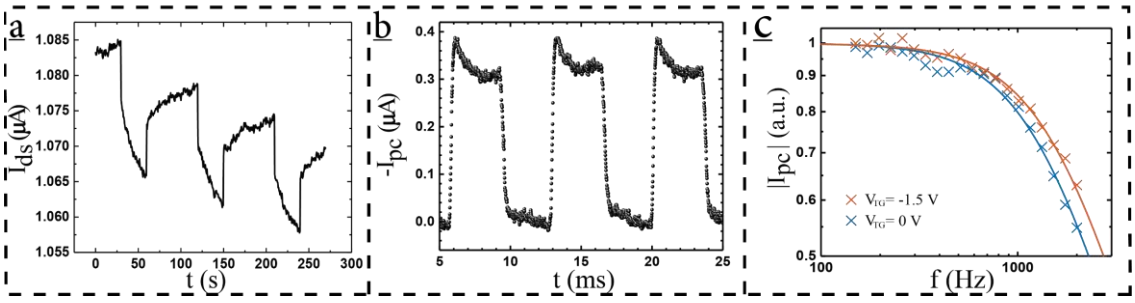

Figure 6-6 time-dependent photocurrent characterisation **a-b** the photocurrent in the absence of ionic polymer and in presence of ionic polymer. **c-** Normalized photoresponse as a function of light modulation frequency.

A detailed frequency-domain measurement reveals a $-3\ dB$ bandwidth for this type of photodetectors at room temperature. Such a parameter is defined by the frequency at which responsivity is reduced to 70% of its maximum value. To reduce the noise level in these measurements an optical chopper wheel was used to modulate the signal of the source enabling the use of a lock-in technique. **Figure (6-6c)** explains the relationship between the frequency and the normalized photocurrent signal, where photocurrent signals are normalized to the maximum which occurs at low modulation frequencies resulting in a $1.3\ kHz$ bandwidth at $(V_{gs} = 0\ V)$ and $1.3\ kHz$ at $V_{gs} = -1.5\ V$. The rise time is 220 μs extracted from $\tau_{rise} \approx 0.35/f_{-3dB}$, in good agreement with the time domain measurement in **Figure (6-6b)**.

The observed bandwidth (1.5 KHz) is within the range of video-frame-rate imaging applications, demonstrating the suitability of electrolyte polymer encapsulated graphene/WS2 photodetectors for these applications.

References

1. Khodkov T, Khrapach I, Craciun MF, Russo S. Direct Observation of a Gate Tunable Band Gap in Electrical Transport in ABC-Trilayer Graphene. *Nano Letters* 2015, **15**(7)**:** 4429-4433.

2. Khodkov T, Withers F, Christopher Hudson D, Felicia Craciun M, Russo S. Electrical transport in suspended and double gated trilayer graphene. *Applied Physics Letters* 2012, **100**(1)**:** 013114.

3. Dröscher S, Roulleau P, Molitor F, Studerus P, Stampfer C, Ensslin K, *et al.* Quantum capacitance and density of states of graphene. *Physica Scripta* 2012, **2012**(T146)**:** 014009.

4. Fang T, Konar A, Xing H, Jena D. Carrier statistics and quantum capacitance of graphene sheets and ribbons. *Applied Physics Letters* 2007, **91**(9)**:** 092109.

5. Guo J, Yoon Y, Ouyang Y. Gate Electrostatics and Quantum Capacitance of Graphene Nanoribbons. *Nano Letters* 2007, **7**(7)**:** 1935-1940.

6. Giannazzo F, Sonde S, Raineri V, Rimini E. Screening Length and Quantum Capacitance in Graphene by Scanning Probe Microscopy. *Nano Letters* 2009, **9**(1)**:** 23-29.

7. Ponomarenko L, Yang R, Gorbachev R, Blake P, Mayorov A, Novoselov K, *et al.* Density of States and Zero Landau Level Probed through Capacitance of Graphene. *Physical Review Letters* 2010, **105**(13)**:** 136801.

8. Cheremisin MV. Quantum capacitance of the monolayer graphene. *Physica E: Low-dimensional Systems and Nanostructures* 2015, **69:** 153-158.

9. Sonde S, Giannazzo F, Raineri V, Rimini E. Dielectric thickness dependence of capacitive behavior in graphene deposited on silicon dioxide. *Journal of Vacuum Science & Technology B: Microelectronics and Nanometer Structures Processing, Measurement, and Phenomena* 2009, **27**(2)**:** 868-873.

10. DasA, PisanaS, ChakrabortyB, PiscanecS, Saha SK, Waghmare UV, *et al.* Monitoring dopants by Raman scattering in an electrochemically top-gated graphene transistor. *Nat Nano* 2008, **3**(4)**:** 210-215.

11. Ponomarenko LA, Yang R, Mohiuddin TM, Katsnelson MI, Novoselov KS, Morozov SV, *et al.* Effect of a High-$\ensuremath{\kappa}$ Environment on Charge Carrier Mobility in Graphene. *Physical Review Letters* 2009, **102**(20)**:** 206603.

12. Fenton DE, Parker JM, Wright PV. Complexes of alkali metal ions with poly(ethylene oxide). *Polymer* 1973, **14**(11)**:** 589.

13. Wright PV. Electrical conductivity in ionic complexes of poly(ethylene oxide). *British Polymer Journal* 1975, **7**(5)**:** 319-327.

14. Xue Z, He D, Xie X. Poly(ethylene oxide)-based electrolytes for lithium-ion batteries. *Journal of Materials Chemistry A* 2015, **3**(38)**:** 19218-19253.

15. Ferloni P, Chiodelli G, Magistris A, Sanesi M. Ion transport and thermal properties of poly(ethylene oxide) - LiClO4 polymer electrolytes. *Solid State Ionics* 1986, **18:** 265-270.

16. Ando T. Screening Effect and Impurity Scattering in Monolayer Graphene. *Journal of the Physical Society of Japan* 2006, **75**(7)**:** 074716.

17. Hwang EH, Adam S, Sarma SD. Carrier Transport in Two-Dimensional Graphene Layers. *Physical Review Letters* 2007, **98**(18)**:** 186806.

18. Chen J-H, Jang C, Xiao S, Ishigami M, Fuhrer MS. Intrinsic and extrinsic performance limits of graphene devices on SiO2. *Nat Nano* 2008, **3**(4)**:** 206-209.

19. Ishigami M, Chen JH, Cullen WG, Fuhrer MS, Williams ED. Atomic Structure of Graphene on SiO2. *Nano Letters* 2007, **7**(6)**:** 1643-1648.

20. Morozov SV, Novoselov KS, Katsnelson MI, Schedin F, Elias DC, Jaszczak JA, *et al.* Giant Intrinsic Carrier Mobilities in Graphene and Its Bilayer. *Physical Review Letters* 2008, **100**(1)**:** 016602.

21. Jena D, Konar A. Enhancement of Carrier Mobility in Semiconductor Nanostructures by Dielectric Engineering. *Physical Review Letters* 2007, **98**(13)**:** 136805.

22. Chen F, Xia J, Tao N. Ionic Screening of Charged-Impurity Scattering in Graphene. *Nano Letters* 2009, **9**(4)**:** 1621-1625.

23. Kim BJ, Jang H, Lee S-K, Hong BH, Ahn J-H, Cho JH. High-Performance Flexible Graphene Field Effect Transistors with Ion Gel Gate Dielectrics. *Nano Letters* 2010, **10**(9)**:** 3464-3466.

24. Chen F, Xia J, Ferry DK, Tao N. Dielectric Screening Enhanced Performance in Graphene FET. *Nano Letters* 2009, **9**(7)**:** 2571-2574.

25. Lu C, Fu Q, Huang S, Liu J. Polymer Electrolyte-Gated Carbon Nanotube Field-Effect Transistor. *Nano Letters* 2004, **4**(4)**:** 623-627.

26. Cho JH, Lee J, He Y, Kim BS, Lodge TP, Frisbie CD. High-Capacitance Ion Gel Gate Dielectrics with Faster Polarization Response Times for Organic Thin Film Transistors. *Advanced Materials* 2008, **20**(4)**:** 686-690.

27. Ye J, Craciun MF, Koshino M, Russo S, Inoue S, Yuan H, *et al.* Accessing the transport properties of graphene and its multilayers at high carrier density. *Proceedings of the National Academy of Sciences* 2011, **108**(32)**:** 13002-13006.

28. Xia JL, Chen F, Wiktor P, Ferry DK, Tao NJ. Effect of Top Dielectric Medium on Gate Capacitance of Graphene Field Effect Transistors: Implications in Mobility Measurements and Sensor Applications. *Nano Letters* 2010, **10**(12)**:** 5060-5064.

29. RadisavljevicB, RadenovicA, BrivioJ, GiacomettiV, KisA. Single-layer MoS2 transistors. *Nat Nano* 2011, **6**(3)**:** 147-150.

30. Braga D, Gutiérrez Lezama I, Berger H, Morpurgo AF. Quantitative Determination of the Band Gap of WS2 with Ambipolar Ionic Liquid-Gated Transistors. *Nano Letters* 2012, **12**(10)**:** 5218-5223.

31. Ming-Wei L, Lezhang L, Qing L, Xuebin T, Kulwinder SD, Peng Z, *et al.* Mobility enhancement and highly efficient gating of monolayer MoS 2 transistors with polymer electrolyte. *Journal of Physics D: Applied Physics* 2012, **45**(34)**:** 345102.

32. Ubrig N, Jo S, Berger H, Morpurgo AF, Kuzmenko AB. Scanning photocurrent microscopy reveals electron-hole asymmetry in ionic liquid-gated WS2 transistors. *Applied Physics Letters* 2014, **104**(17)**:** 171112.

33. Kuiri M, Chakraborty B, Paul A, Das S, Sood AK, Das A. Enhancing photoresponsivity using MoTe2-graphene vertical heterostructures. *Applied Physics Letters* 2016, **108**(6)**:** 063506.

34. Namgung S, Shaver J, Oh S-H, Koester SJ. Multimodal Photodiode and Phototransistor Device Based on Two-Dimensional Materials. *ACS Nano* 2016, **10**(11)**:** 10500-10506.

35. Furchi MM, Polyushkin DK, Pospischil A, Mueller T. Mechanisms of Photoconductivity in Atomically Thin MoS2. *Nano Letters* 2014, **14**(11)**:** 6165-6170.

36. Britnell L, Ribeiro RM, Eckmann A, Jalil R, Belle BD, Mishchenko A, *et al.* Strong Light-Matter Interactions in Heterostructures of Atomically Thin Films. *Science* 2013, **340**(6138)**:** 1311-1314.

37. Yu WJ, Liu Y, Zhou H, Yin A, Li Z, Huang Y, *et al.* Highly efficient gate-tunable photocurrent generation in vertical heterostructures of layered materials. *Nature Nanotechnology* 2013, **8:** 952.

38. Kufer D, Konstantatos G. Highly Sensitive, Encapsulated MoS2 Photodetector with Gate Controllable Gain and Speed. *Nano Letters* 2015, **15**(11)**:** 7307-7313.

39. Haigh SJ, Gholinia A, Jalil R, Romani S, Britnell L, Elias DC, *et al.* Cross-sectional imaging of individual layers and buried interfaces of graphene-based heterostructures and superlattices. *Nat Mater* 2012, **11**(9)**:** 764-767.

40. Roy K, Padmanabhan M, Goswami S, Sai TP, Ramalingam G, Raghavan S, *et al.* Graphene–MoS2 hybrid structures for multifunctional photoresponsive memory devices. *Nature Nanotechnology* 2013, **8:** 826.

41. Mehew JD, Unal S, Torres Alonso E, Jones GF, Fadhil Ramadhan S, Craciun MF, *et al.* Fast and Highly Sensitive Ionic-Polymer-Gated WS2–Graphene Photodetectors. *Advanced Materials* 2017**:** 1700222-n/a.

42. Bointon TH, Barnes MD, Russo S, Craciun MF. High Quality Monolayer Graphene Synthesized by Resistive Heating Cold Wall Chemical Vapor Deposition. *Advanced Materials* 2015, **27**(28)**:** 4200-4206.

43. Koppens FHL, Mueller T, Avouris P, Ferrari AC, Vitiello MS, Polini M. Photodetectors based on graphene, other two-dimensional materials and hybrid systems. *Nat Nano* 2014, **9**(10)**:** 780-793.

44. Buscema M, Island JO, Groenendijk DJ, Blanter SI, Steele GA, van der Zant HSJ, *et al.* Photocurrent generation with two-dimensional van der Waals semiconductors. *Chemical Society Reviews* 2015, **44**(11)**:** 3691-3718.

45. Konstantatos G, Badioli M, Gaudreau L, Osmond J, Bernechea M, de Arquer FPG, *et al.* Hybrid graphene-quantum dot phototransistors with ultrahigh gain. *Nat Nano* 2012, **7**(6)**:** 363-368.

Chapter 7

Novel circuit design for high-impedance and non-local electrical measurements of two-dimensional materials

7.1 Motivation

The recently discovered classes of new materials such as the atomically thin and the topological materials lead to the emergence of modern physics concepts: spintronics[162, 163, 164] and valleytronics[43, 165, 166, 167] which can be investigated using electrical transport measurements in a non-local geometry. In such a non-local electrical transport measurement the voltage appears between probes that are placed far away from the classical current path. However, the difficulty of measuring data underpinning these concepts evade detection by the standard electrical measurement techniques and require advances in the design of the electrical circuits employed. In particular, rather than typical low-impedance (Low-Z), a high-impedance (Hi-Z) circuit is required to eliminate and distinguish the spurious signals from the real signal. Those concepts are very sensitive to any distortion from the device itself or from the environment. Therefore, a high accuracy tool needs to be used to detect the signal. It is commonly agreed that alternate-current (AC) lock-in amplifier can recover signals in the presence of an overwhelming noise background or, alternatively, it can provide high resolution measurements of relatively clean signals over several orders of magnitude and frequency. This means that lock-in amplifiers can be used to characterize the response underlying these concepts in electrical devices. However, careful consideration needs to be given when lock-in amplifier is used to characterize non-local measurements. The spurious negative value of resistance[162, 166] can be present when using lock-in amplifier due to the low impedance of its input, which can lead to the flow of the current between the input and the ground. Also, the negativity arises from the incomplete rejection of the common-mode voltage (CMV) at the input of lock-in amplifier and the dielectric leakage of the transmission lines, usually BNC-terminated coaxial cables. DC

amplifiers can be the solution since they have higher input impedance. However, low DC easy to pick noise and high DC currents generate Joule heating, making challenging the DC characterization of insulating states with narrow energy gaps, such as those found in 2D materials[168].

These challenges motivated us to develop an experimental apparatus designed specifically to overcome the aforementioned limitations, allowing us to eliminate spurious artefacts and grant direct access to the aforementioned Hi-Z states. We employ this circuit in two state-of-the-art experiments: measurement of the non-local resistance in a graphene Hall bar in a perpendicular magnetic field and AC electrical characterisation of an atomically thin WS2 field-effect transistor, as I will show in this chapter.

7.2 Operating principles

The main idea of these type of circuits is to isolate electrically the circuit responsible to current injection from the that to probe the voltage variation. The best way to make the isolation is to use the optical isolator (or optocoupler) circuit. It consists of light emitting diodes (LED) and photodiodes, in which the electrical signal will convert to optical signal then back to electrical signal.

Figure (7-1) illustrates the key electronic circuit. This is made up of a bipolar optocoupler with integrated double supply in terms of two HCNR201 high-linearity analogue optocoupler (OC2 and OC1) ICs (integrated circuits). These ICs consist of two photodiodes and a LED. While the secondary photodiode is applied as a feedback to bring about optimum stability and linearity, a primary photodiode is applied to convey the input signal to the output. Such a property makes the HCNR201 performance extremely close to that of a perfect optocoupler. In fact, the characteristic nonlinearity (that is, the end-point divergence from a straight line in

the correlation between the current calculated from the second, I_{pd} and the current calculated from the first photodiode) of the instrument is 0.01 percent, with a maximum of 0.05 percent under test conditions of$0\ V < I_{pd} < 15\ V$ and $5\ nA < I_{pd} < 50$ mA. On the other hand, the temperature coefficient of HCNR201 is -0.3%/ºC between -40 ºC and 85 ºC, equivalent to a maximum nonlinearity of 0.07% in this scope[169].

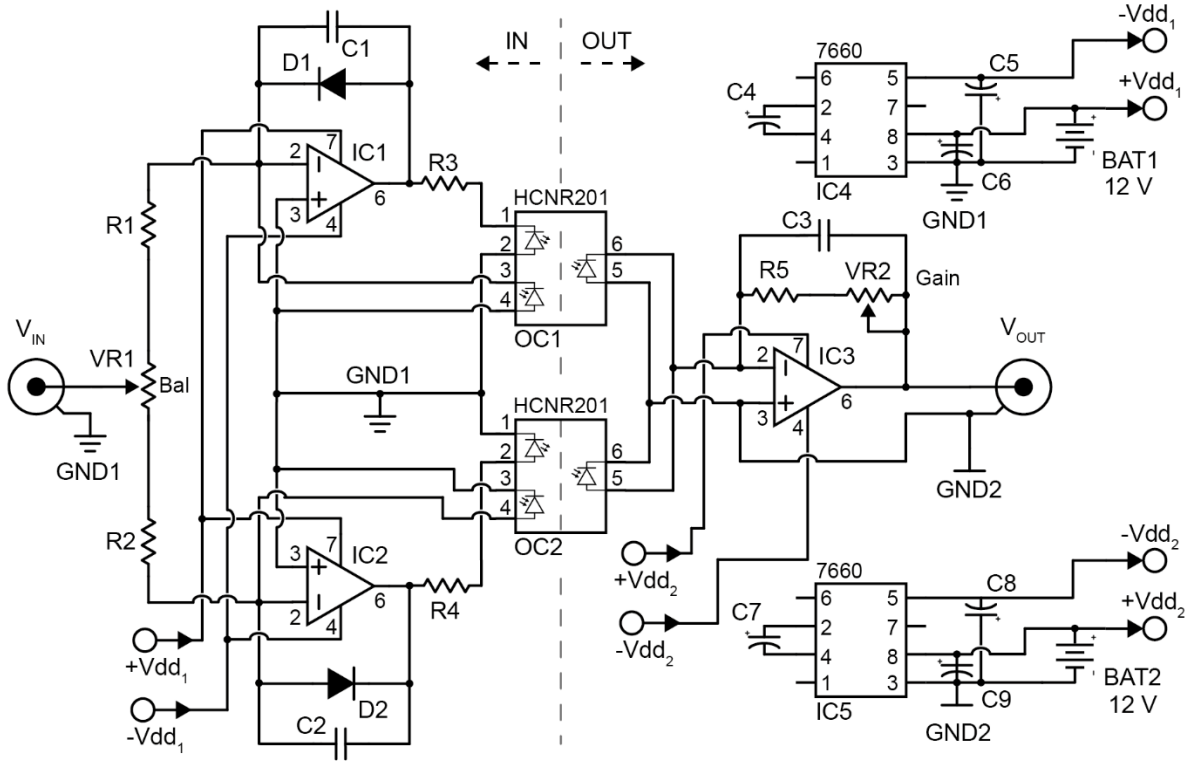

Figure 7- 1 Electronic schematic of the bipolar optocoupler circuit. The circuit is designed around two HCNR201 high-linearity optocouplers (OC1 and OC2) powered by two 12 V batteries. Two ICL7660 CMOS voltage converters (IC4 and IC5) are used to supply the required dual voltage (_12 V) to the operational amplifiers (IC1, IC2, and IC3). The vertical dashed line indicates the optical coupling point between the input (IN) and the output (OUT) stages of the circuit.

The V_{IN} (input signal) is fed via VR1 (a balance variable resistor) to the LED stage of the optocouplers. All the secondary photodiodes are connected to a feedback loop consisting of a diode (D1 and D2, correspondingly) and an operational amplifier (Op

Amp, IC1 as well as IC2, correspondingly). The diodes are connected so that the negative and positive sections of the signal are conveyed through one HCNR201 or the other. The variable resistor (VR1) is applied to make up for the resistance disparity in the input phase between the two routes of the circuit, and it is regulated before operation so as to get similar voltage swings in the negative and positive sections of the AC signal. The input stage of HCNR201 is ground in common with the shell of the input BNC. The output phase is made up of an IC3 (operational amplifier) with a gain of 1 (controlled via VR2) and the HCNR201 primary photodiodes. The input path is isolated from the one of the grounding of the output phase. The circuit of the power-supply is made up of two ICL7660A voltage inverters (IC5 and IC4) which produce the dual voltage (±12 V) needed for the right working of the Op-Amps, and two 12V LiPo (lithium-polymer) batteries (one for the output stage and the other for the input). The size of the instrument is reduced by the use of the two voltage inverters which eliminate the application of two pairs of batteries to generate a dual voltage. Ultimately, three LT1097 Op-Amps are used for the output and input stages (IC1, IC2, and IC3) in the low-power design, but these are substituted with three LT1028 Op-Amps in the low-noise one.

The separation of the electrical wirings used to connect the measuring devices (including spectrum analysers, oscilloscopes, and voltage and lock-in amplifiers) to the instrument to be tested is achieved through the design shown in **Figure (7-2)**. Vacuum chamber is provided with a PET (polyethylene terephthalate) vacuum extension onto which 9 vacuum-suited SMA links are wired, see **Figure (7-2a)**. The PET structure of the extension gives high insulation between the shells of the SMA connectors (>1 TΩ). A single-core copper wire is used to directly wire the central pin of each connector to the sample holder. The component to be tested is wired on a custom-built printed-circuit-board whereby high insulation between every contact

pin is secured by using double spaces in single-in-line commercial links, between 2.54 mm and 5.08 mm, as illustrated in **Figure (7-2c)**. The break-out box used to wire every SMA connector to the measuring instrument is the most significant component of the device. It has to uphold a strong electrical insulation acquired in the vacuum chamber. This is diagrammatically illustrated in **Figure (7-2b)**. Essentially, the possibility of connecting every core and every shell separately to one ground line (GND1) or another (GND2) is facilitated by the use of mechanical switches. **Figure (7-2d)** presents a picture of the actual device. The entire assemblage is intended to retrofit into some dimension units such as optical microscopes, dipping probes and cryostats (for this case, this has been mounted to an *Oxford Instruments* Microstat MO highly conducting magnet).

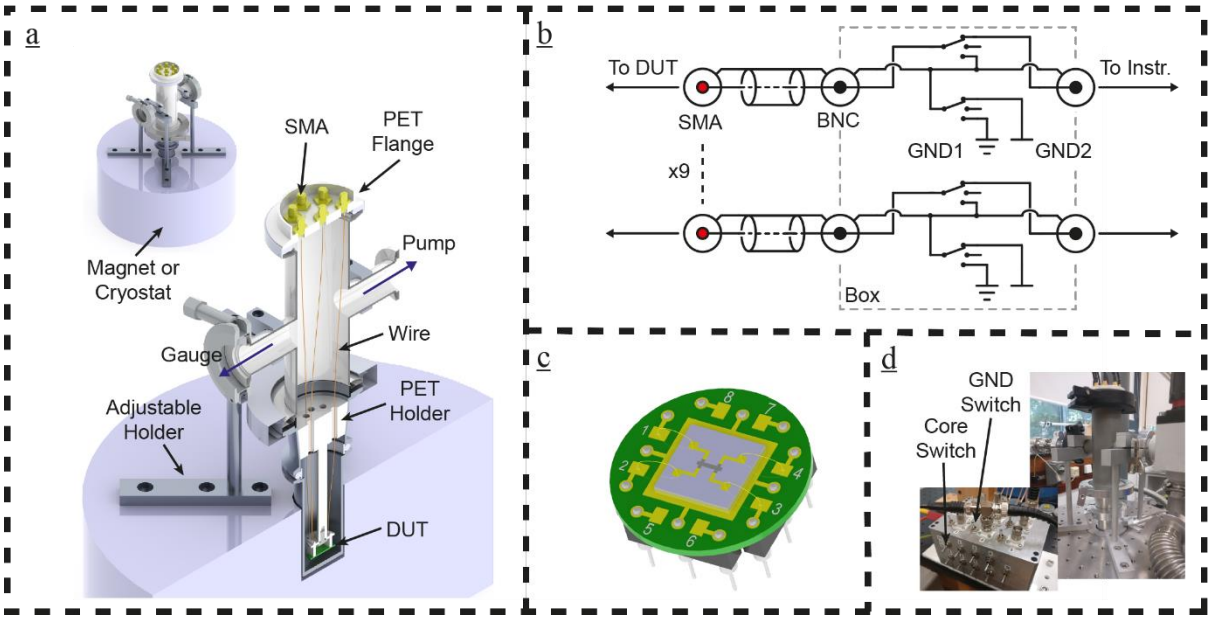

Figure 7- 2 High-impedance measuring chamber and circuitry **a-** Schematic drawing of the vacuum chamber used to perform the measurements, configured to retrofit a magnet or cryostat. In order to avoid stray capacitance, each SMA connector is wired to the device under test (DUT) using a single-core insulated copper wire. **b-** Schematic of the break-out box used to interface the DUT to the measuring instruments. For each BNC connector, it is possible to choose two separate terminals for the shielding (GND1 and GND2), in order to ensure complete floating of the measuring probes. **c-** Model of the printed circuit board (PCB) used to mount the DUT. The pins are spaced 5 mm apart to ensure high insulation. **d-** Photograph of the actual chamber mounted on an *Oxford Instruments* Microstat MO superconducting magnet.

Figure (7-1) shows the circuit that is wired on a printed circuit board and fitted in a metal box for protection, by means of through-hole elements. Such a circuit can easily be adjusted to utilize surface-mount parts for premium space operations. The fidelity, that is, the capacity to give out the V_{in} (input signal) at the V_{out} (output), of both sides of the circuit is presented in **Figure (7-3a)** (in which V2 is the low-noise and V1 is the low-power type). For the two versions, no considerable distinction is seen in the input curves from the output ones.

The noise has been determined as a function of frequency by use of an *Ametek* Model 7270 DSP lock-in amplifier in the noise-determination mode. The noise from the two versions of the optocoupler and the lock-in (black line) are shown in **Figure (7-3b)**. It is apparent that the low-power type has a noise level of $> 10^{-5}V/\sqrt{Hz}$ and an evident peak about 100 Hz. The noise level at higher frequencies ranges from one to two orders of magnitude higher than the lock-in intrinsic level ($> 10^{-7}V/\sqrt{Hz}$). This is mainly due to the noise efficiency of the chosen Op-Amps. The apparent sharp peak at 6 kHz matches with the opeating frequency of ICL7660A to give the negative supply voltage. On the other hand, the low-noise type illustrates a low frequency noise level similar to that of the lock-in amplifier ($> 10^{-5}V/\sqrt{Hz}$). This indicates that its intrinsic noise level is no less than one order of magnitude less than the lock-in noise level. Although with a somewhat higher noise level larger than 1 kHz, similar characterstics of the low-power version is seen at higher frequencies. For the two versions, the frequency of ICL7660A can easily be adjusted in a wide range by introducing a small capacitor to the circuit (between GND and pin 7 in **Figure (7-1)**, facilitating the modification of the optocoupler's high-frequency noise level.

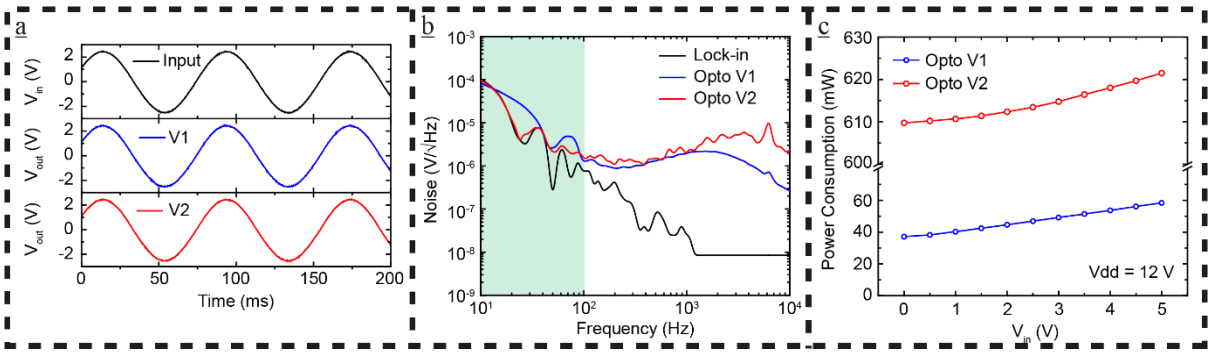

Figure 7- 3 Performance of the optocoupler circuits **a-** Input versus output signal for the low-power (V1) and low-noise (V2) versions. **b-** Noise as a function of frequency for the two versions compared to the intrinsic noise of the measuring lock-in amplifier. The low-frequency region is highlighted in green. **c-** Power consumption as a function of input voltage (peak-to-peak) for the two versions of the optocoupler circuit.

Figure (7-3c) demonstrates the amount of power consumed as a function of input voltage for every model. It can be deduced that the low noise version consumes about ten times the amount of power compared to the low-power one. This is caused by the bigger current used by the LT1028 low noise operational amplifier as this operational amplifier's input transistor works at about 1 mA of collector currents to attain low voltage noise, because the square root of the collector current is inversely proportional to voltage noise. To allow for the remote use of the circuit, it is estimated that a 4Ah battery (used in the tests) is capable of powering the low power type for about 40 days in constant operation (with the assumption that $V_{in} = 2.5\,V$), while the low-noise version go for approximately 3.5 days.

7.3 Non-local and high-impedance measurement

The description of a field-effect transistor based on WS2 with high contact resistance and the non-local resistance in a graphene Hall bar are the two state-of-the-art measurements vulnerable to the adverse effects from artefacts in a normal

experimental arrangement so as to demonstrate the capabilities and use of the instrument.

Non-local resistance measurements denote the setup where the voltage calculations distant from the flow of current, characteristically in a Hall bar arrangement. Such a form of measurement in graphene apparatus has, in recent years, showed some odds of charge transmission, which include hydrodynamic transmission of charges, topological valley transmission in bilayer graphene and lifting of valley/spin degeneracy in monolayer graphene. In any case, small voltages and/or small currents have to be resolved in environmentally responsive apparatus and a Clock-in measurement determine the suitable experimental method to use. The objects that occur in these measurements and how to be removed using the developed optocouplers are discussed here. The apparatus under investigation is composted of a single-layer exfoliated graphene flake sandwiched between two thin layers of hBN (hexagonal Boron Nitride) put on a Si substrate with 300 nm SiO_2 as the gate dielectric. Au/Cr electrodes are used to contact the graphene in a 1D contact or a side-contact configuration. This design and the geometry of contacts facilitate the attainment of the ultra-high mobilities needed in the observation of non-local effects in micron-scaled graphene.

Figure (7-4a) schematically shows a characteristic room temperature non-local lock-in setup of a graphene Hall bar. The current flows between contacts 1 and 2, via R_B (a ballast resistor), and the V_{nl} (voltage drop) is determined between contacts 3 and 4. This experimental setup gives the results illustrated in **Figure (7-4b)**, in which the R_{nl} (non-local resistance) is plotted as against V_{bg} (gate voltage) in the absence, and presence, of a B (magnetic field) perpendicularly applied to the sample. It is clear that the graph in **Figure (7-4b)** for B = 2 T gives a negative resistance peak at V_{bg} = -10 V, corresponding to the graphene Hall bar charge neutrality point. The

manifestation of a negative bending resistance is a signature of the room temperature ballistic transport, although it has been observed in graphene. This effect is immeasurable in our geometry since it necessitates a cross-shaped apparatus, where the voltage-sensing and current-injection are conducted by means of a pair of orthogonal contacts. Thus, the observed feature is a feature presented by the measurement setup. This is due to the

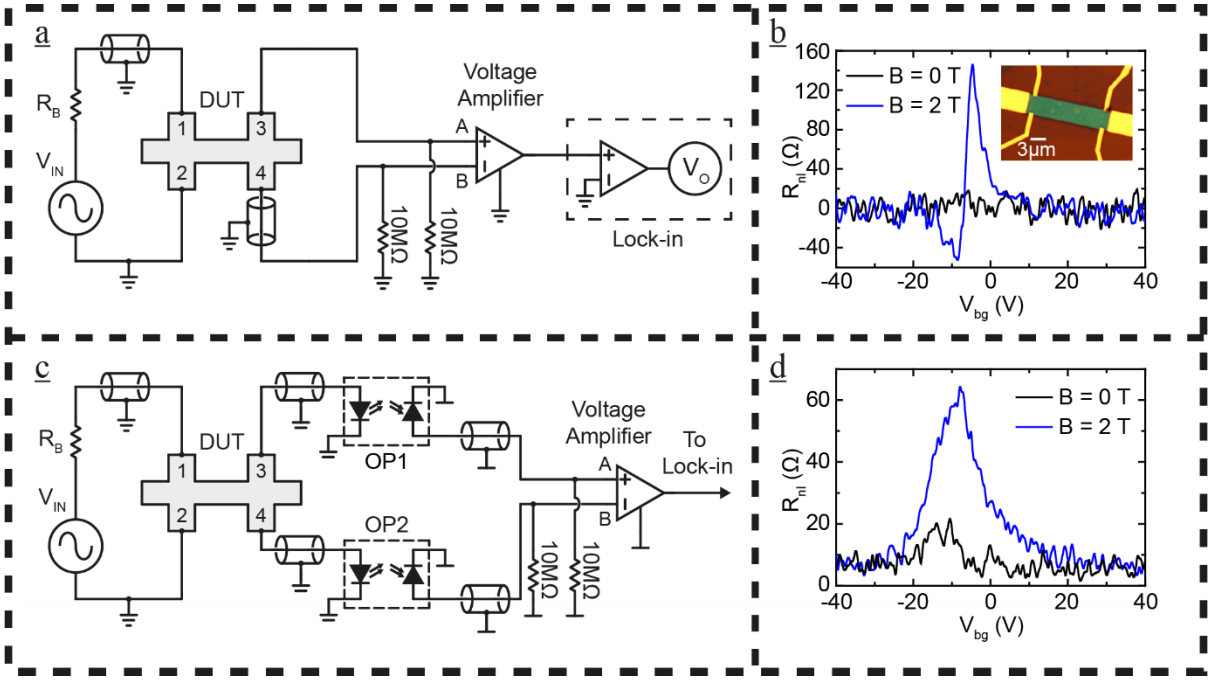

Figure 7- 4 Measurement of non-local resistance in graphene **a-** Standard lock-in measurement configuration. The current is injected between points 1 and 2 in a graphene Hall bar, and the non-local voltage is measured between points 3 and 4. **b-** Non-local resistance (R_{nl}) as a function of gate voltage in a sample device (inset) measured using the arrangement in panel (a) with and without the magnetic field (B = 2 T). **c-** Floating-probe arrangement with optocouplers of the same measurement and **d-** non-local resistance measured in this configuration.

partial rejection of the V_{cmv} (CMV) at the amplifier's input side. A difference in the resistance between the current-injection leads results in a voltage drop which would be connected to the voltage-probes through the device itself and through ground

coupling (between pins 2–4 and 1–3). The equation below is used to calculate fake non-local voltage.

$$V'_{nl} = \frac{V_{cmv}R_{in}}{R_{in}+R_1} - \frac{V_{cmv}R_{in}}{R_{in}+R_2} \approx (R_2 - R_1)\frac{V_{cmv}}{R_{in}},$$

Where, R_{in} represents the voltage amplifier's input impedance, normally 1–10 MΩ, and $R_1(R_{2)}$ represents the sum of resistance across the local section of the circuit, including RB, the contact resistance of points 2 and 4 (or1 and 3) and R_{in}. The BNC cables's dielectric leakage toward the cable insulation leads to the ground coupling. This successfully enables a signal produced between contacts 1 and 2 to be detected between contacts 3 and 4 evading the device. The V_{cmv} value rises with the increase in channel resistance, and its maximum value is at the charge neutrality point. **Figure (7-4b)** notably reveals that the value V'_{nl} can be bigger than the actual non-local signal, depending on R_1 and R_2 values, and it can have opposite sign. The configuration demonstrated in **Figure (7-4c)** was adopted so to hold back this fake signal. Furthermore, two of the optocoupler circuits illustrated in Fig. 1 are applied in floating the voltage probes. The design of the measuring chamber and battery-powered circuits allow for decoupling the shells of the coaxial cables and ground lines. **Figure (7-4d)** shows the non-local measurement obtained using such an arrangement, whereby no artefact exists, and a non-local resistance peak is observable where there is a magnetic field at room temperature. This is shown in the study for a single-layer graphene on a Si/SiO2 substrate, in which this signal has been related to the FHE (flavour Hall Effect). A residual non-local signal is evident at zero magnetic fields. This has been attributed to Joule heating in the study (it brings about a voltage in the non-local probes caused by the disparity in contact resistance). Remarkably, the experiments reveal that the fake signal is almost the

size of the actual non-local signal, since it can be observed by evaluating the values of R_{nl} illustrated in **Figures (7-4b)** and **(7-4d)** and determined using Equation (1). In addition, the ground coupling seen in the connectors and coaxial wires, liable for the evident artefacts, normally occurs in a standard AC lock-in measurement. It can also be calculated in other Hi-Z apparatus including the insulating state of 2D materials or metallic thin films.

From this point, the application of the developed optocoupler in the AC electrical properties of a thin semiconductor transistor in terms of WS2 will be demonstrated. The apparatus is composted of a single-layer chemical-vapour-deposition developed WS2 on a Si substrate with 300 nano meter SiO2 as gate dielectric, with Cr/Au electrodes defined in terms of lithography. The inset of **Figure (7-5c)** shows a micrograph of the device. The electrical circuit arrangement applied in the description with and without the optocouplers is shown in **Figures (7-5b)** and **(7-5a)**, correspondingly. In **Figure (7-5c)**, a DC characterization of the device is benchmarked against the measurements acquired from the two different AC arrangements. It was experimentally established that the AC attributes differ considerably from the DC capacities without optocouplers. However, the correct features [**Figure (7-5c)**, red line] are observable through the configuration shown in **Figure (7-5b)**. Owing to a big barrier created at the contacts, a common issue in both CVD-grown and exfoliated transition-metal dichalcogenides, a sharp decrease in the channel resistance with the applied bias voltage is anticipated in these materials. This feature is correctly demonstrated in the AC configuration and in the DC capacity by means of the optical isolators.

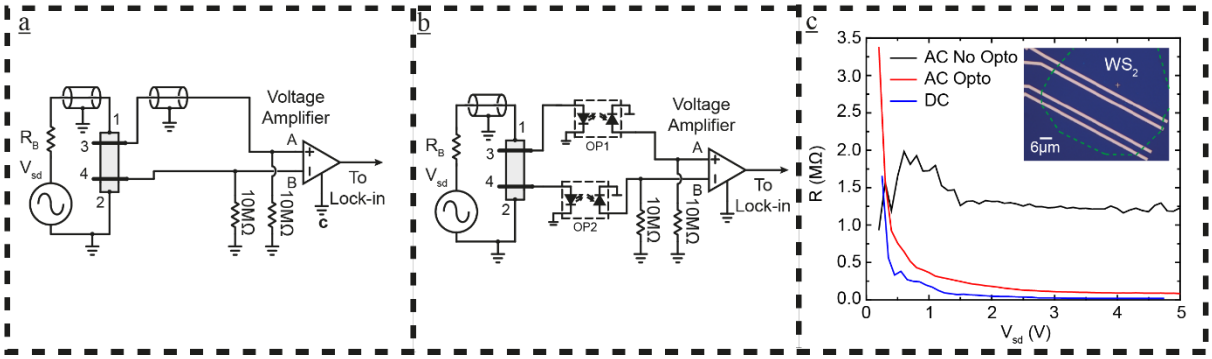

Figure 7- 5 Characterization of a WS2 field-effect transistor **a-** Electrical circuit configuration for the local 4-probe AC measurement of a field-effect transistor (FET). **b-** Floating-probe arrangement of the same FET measurement in panel (a); coaxial cables are omitted for clarity. **c-** Resistance as a function of bias of a WS2-based (FET), measured in the two AC configurations shown in panels (a) and (b) and in DC.

7.4 Conclusion

To conclude, an integrated optoelectrical circuit was presented which allowed the application of low input impedance and low-noise AC lock-in for the classification of high- Z apparatus. It was shown that such an optocoupler removes big fake electrical signals by successfully decoupling the voltage sensing devices from the current-driving circuit. Its performance was demonstrated based on fidelity, power consumption, which results in a continuous operation up to 40 days using a small-size battery and noise level, which is as low as the intrinsic noise level of the measuring instrument. The size of the circuit can easily be reduced by means of surface-mount modules and rapidly up-scaled to suit flexible applications when two or more contacts are required in a minute space, for instance in space applications, big machines including particle accelerators and in current research on quantum computing. The built optocouplers suitably fit the low-noise electrical classification of narrow-gap conditions and semiconductors future applications in quantum technologies including sensing, communication and computation. Although the use

of the circuitry in the characterization of 2D systems was the focus of this study, the method can be used in the electrical measurement of a huge number of devices where high-impedance states has to be reached, which include quantum dots, nanotubes, nanowires, metal thin-films, polymers and composites.

References

1. Banszerus L, Schmitz M, Engels S, Dauber J, Oellers M, Haupt F, *et al.* Ultrahigh-mobility graphene devices from chemical vapor deposition on reusable copper. *Science Advances* 2015, **1**(6).

2. Lee C, Wei X, Kysar JW, Hone J. Measurement of the Elastic Properties and Intrinsic Strength of Monolayer Graphene. *Science* 2008, **321**(5887)**:** 385-388.

3. Nair RR, Blake P, Grigorenko AN, Novoselov KS, Booth TJ, Stauber T, *et al.* Fine Structure Constant Defines Visual Transparency of Graphene. *Science* 2008, **320**(5881)**:** 1308-1308.

4. Wallace P. The Band Theory of Graphite. *Physical Review* 1947, **71**(9)**:** 622-634.

5. Atkins PW, De Paula J, Walters V. *Physical Chemistry*. Macmillan Higher Education, 2006.

6. Craciun MF. Alkali-doped metal-phthalocyanine and pentacene compounds. PhD thesis, TUDelft, 2006.

7. Grosso G, Parravicini GP. *Solid State Physics*. Elsevier Science, 2013.

8. Wong HSP, Akinwande D. *Carbon Nanotube and Graphene Device Physics*. Cambridge University Press, 2011.

9. McCann E, Abergel DSL, Fal'ko VI. Electrons in bilayer graphene. *Solid State Commun* 2007, **143**(1)**:** 110-115.

10. Katsnelson MI, Katsnel′son MI. *Graphene: Carbon in Two Dimensions*. Cambridge University Press, 2012.

11. Shon NH, Ando T. Quantum Transport in Two-Dimensional Graphite System. *Journal of the Physical Society of Japan* 1998, **67**(7)**:** 2421-2429.

12. Du X, Skachko I, Barker A, Andrei EY. Approaching ballistic transport in suspended graphene. *Nat Nano* 2008, **3**(8)**:** 491-495.

13. Bolotin KI, Sikes KJ, Jiang Z, Klima M, Fudenberg G, Hone J, *et al*. Ultrahigh electron mobility in suspended graphene. *Solid State Commun* 2008, **146**(9-10)**:** 351-355.

14. Ando T. Screening Effect and Impurity Scattering in Monolayer Graphene. *Journal of the Physical Society of Japan* 2006, **75**(7)**:** 074716.

15. Adam S, Hwang EH, Galitski VM, Das Sarma S. A self-consistent theory for graphene transport. *Proceedings of the National Academy of Sciences* 2007, **104**(47)**:** 18392-18397.

16. Galitski VM, Adam S, Das Sarma S. Statistics of random voltage fluctuations and the low-density residual conductivity of graphene. *Physical Review B* 2007, **76**(24)**:** 245405.

17. Pereira VM, Nilsson J, Castro Neto AH. Coulomb Impurity Problem in Graphene. *Physical Review Letters* 2007, **99**(16)**:** 166802.

18. Adam S, Hwang EH, Das Sarma S. Scattering mechanisms and Boltzmann transport in graphene. *Physica E: Low-dimensional Systems and Nanostructures* 2008, **40**(5)**:** 1022-1025.

19. Chen J-H, Jang C, Xiao S, Ishigami M, Fuhrer MS. Intrinsic and extrinsic performance limits of graphene devices on SiO2. *Nat Nano* 2008, **3**(4)**:** 206-209.

20. Mariani E, von Oppen F. Flexural Phonons in Free-Standing Graphene. *Physical Review Letters* 2008, **100**(7)**:** 076801.

21. Castro EV, Ochoa H, Katsnelson MI, Gorbachev RV, Elias DC, Novoselov KS, *et al.* Limits on Charge Carrier Mobility in Suspended Graphene due to Flexural Phonons. *Physical Review Letters* 2010, **105**(26)**:** 266601.

22. Fratini S, Guinea F. Substrate-limited electron dynamics in graphene. *Physical Review B* 2008, **77**(19)**:** 195415.

23. Hwang EH, Das Sarma S. Acoustic phonon scattering limited carrier mobility in two-dimensional extrinsic graphene. *Physical Review B* 2008, **77**(11)**:** 115449.

24. Cheianov VV, Fal'ko VI. Selective transmission of Dirac electrons and ballistic magnetoresistance of $n\text{-}p$ junctions in graphene. *Physical Review B* 2006, **74**(4)**:** 041403.

25. Novoselov KS, Geim AK, Morozov SV, Jiang D, Zhang Y, Dubonos SV, *et al.* Electric Field Effect in Atomically Thin Carbon Films. *Science* 2004, **306**(5696)**:** 666-669.

26. Hwang EH, Das Sarma S. Graphene magnetoresistance in a parallel magnetic field: Spin polarization effect. *Physical Review B* 2009, **80**(7)**:** 075417.

27. Hwang EH, Adam S, Sarma SD. Carrier Transport in Two-Dimensional Graphene Layers. *Physical Review Letters* 2007, **98**(18)**:** 186806.

28. Zhu W, Perebeinos V, Freitag M, Avouris P. Carrier scattering, mobilities, and electrostatic potential in monolayer, bilayer, and trilayer graphene. *Physical Review B* 2009, **80**(23)**:** 235402.

29. Ferry DK, Goodnick SM, Bird J. *Transport in Nanostructures*. Cambridge University Press, 2009.

30. Ohta T, Bostwick A, McChesney JL, Seyller T, Horn K, Rotenberg E. Interlayer Interaction and Electronic Screening in Multilayer Graphene

Investigated with Angle-Resolved Photoemission Spectroscopy. *Physical Review Letters* 2007, **98**(20)**:** 206802.

31. Guinea F. Charge distribution and screening in layered graphene systems. *Physical Review B* 2007, **75**(23)**:** 235433.

32. Dean CR, Young AF, MericI, LeeC, WangL, SorgenfreiS, *et al*. Boron nitride substrates for high-quality graphene electronics. *Nat Nano* 2010, **5**(10)**:** 722-726.

33. Banszerus L, Schmitz M, Engels S, Goldsche M, Watanabe K, Taniguchi T, *et al*. Ballistic Transport Exceeding 28 μm in CVD Grown Graphene. *Nano Letters* 2016, **16**(2)**:** 1387-1391.

34. Malard LM, Pimenta MA, Dresselhaus G, Dresselhaus MS. Raman spectroscopy in graphene. *Physics Reports* 2009, **473**(5–6)**:** 51-87.

35. Ferrari AC, Basko DM. Raman spectroscopy as a versatile tool for studying the properties of graphene. *Nat Nano* 2013, **8**(4)**:** 235-246.

36. Saito R, Hofmann M, Dresselhaus G, Jorio A, Dresselhaus MS. Raman spectroscopy of graphene and carbon nanotubes. *Advances in Physics* 2011, **60**(3)**:** 413-550.

37. Manzeli S, Ovchinnikov D, Pasquier D, Yazyev OV, Kis A. 2D transition metal dichalcogenides. 2017, **2:** 17033.

38. Toh RJ, Sofer Z, Luxa J, Sedmidubsky D, Pumera M. 3R phase of MoS2 and WS2 outperforms the corresponding 2H phase for hydrogen evolution. *Chemical Communications* 2017, **53**(21)**:** 3054-3057.

39. Schutte WJ, De Boer JL, Jellinek F. Crystal structures of tungsten disulfide and diselenide. *Journal of Solid State Chemistry* 1987, **70**(2)**:** 207-209.

40. Kuc A, Zibouche N, Heine T. Influence of quantum confinement on the electronic structure of the transition metal sulfide TS${}_{2}$. *Physical Review B* 2011, **83**(24)**:** 245213.

41. Rycerz A, Tworzyd o J, Beenakker C. Valley filter and valley valve in graphene. *Nature Physics* 2007, **3**(3)**:** 172-175.

42. Xiao D, Yao W, Niu Q. Valley-Contrasting Physics in Graphene: Magnetic Moment and Topological Transport. *Physical Review Letters* 2007, **99**(23)**:** 236809.

43. Zhang YJ, Yoshida M, Suzuki R, Iwasa Y. 2D crystals of transition metal dichalcogenide and their iontronic functionalities. *2D Materials* 2015, **2**(4)**:** 044004.

44. Grosso G. 2D materials: Valley polaritons. *Nat Photon* 2017, **11**(8)**:** 455-456.

45. Klein A, Tiefenbacher S, Eyert V, Pettenkofer C, Jaegermann W. Electronic band structure of single-crystal and single-layer ${\mathrm{WS}}_{2}:$ Influence of interlayer van der Waals interactions. *Physical Review B* 2001, **64**(20)**:** 205416.

46. Yun WS, Han SW, Hong SC, Kim IG, Lee JD. Thickness and strain effects on electronic structures of transition metal dichalcogenides: 2H-$M{X}_{2}$ semiconductors (M $=$ Mo, W; X $=$ S, Se, Te). *Physical Review B* 2012, **85**(3)**:** 033305.

47. Liu G-B, Shan W-Y, Yao Y, Yao W, Xiao D. Three-band tight-binding model for monolayers of group-VIB transition metal dichalcogenides. *Physical Review B* 2013, **88**(8)**:** 085433.

48. Xu R, Husmann A, Rosenbaum TF, Saboungi ML, Enderby JE, Littlewood PB. Large magnetoresistance in non-magnetic silver chalcogenides. *Nature* 1997, **390**(6655)**:** 57-60.

49. Liang T, Gibson Q, Ali MN, Liu M, Cava RJ, Ong NP. Ultrahigh mobility and giant magnetoresistance in the Dirac semimetal Cd3As2. *Nat Mater* 2015, **14**(3)**:** 280-284.

50. Shekhar C, Nayak AK, Sun Y, Schmidt M, Nicklas M, Leermakers I, *et al.* Extremely large magnetoresistance and ultrahigh mobility in the topological Weyl semimetal candidate NbP. *Nat Phys* 2015, **11**(8)**:** 645-649.

51. Gopinadhan K, Shin YJ, Jalil R, Venkatesan T, Geim AK, Neto AHC, *et al.* Extremely large magnetoresistance in few-layer graphene/boron-nitride heterostructures. *Nat Commun* 2015, **6**.

52. Kisslinger F, Ott C, Heide C, Kampert E, Butz B, Spiecker E, *et al.* Linear magnetoresistance in mosaic-like bilayer graphene. *Nat Phys* 2015, **advance online publication**.

53. Assaf BA, Cardinal T, Wei P, Katmis F, Moodera JS, Heiman D. Linear magnetoresistance in topological insulator thin films: Quantum phase coherence effects at high temperatures. *Applied Physics Letters* 2013, **102**(1)**:** 012102.

54. Wang W, Du Y, Xu G, Zhang X, Liu E, Liu Z, *et al.* Large Linear Magnetoresistance and Shubnikov-de Hass Oscillations in Single Crystals of YPdBi Heusler Topological Insulators. *Scientific Reports* 2013, **3:** 2181.

55. Lee M, Rosenbaum TF, Saboungi ML, Schnyders HS. Band-Gap Tuning and Linear Magnetoresistance in the Silver Chalcogenides. *Physical Review Letters* 2002, **88**(6)**:** 066602.

56. Parish MM, Littlewood PB. Non-saturating magnetoresistance in heavily disordered semiconductors. *Nature* 2003, **426**(6963)**:** 162-165.

57. Konstantatos G, Sargent EH. Nanostructured materials for photon detection. *Nature Nanotechnology* 2010, **5:** 391.

58. Buscema M, Island JO, Groenendijk DJ, Blanter SI, Steele GA, van der Zant HSJ, *et al.* Photocurrent generation with two-dimensional van der Waals semiconductors. *Chemical Society Reviews* 2015, **44**(11)**:** 3691-3718.

59. Gabor NM, Song JCW, Ma Q, Nair NL, Taychatanapat T, Watanabe K, *et al.* Hot Carrier–Assisted Intrinsic Photoresponse in Graphene. *Science* 2011, **334**(6056)**:** 648-652.

60. Ashcroft NW, Mermin ND. *Solid State Physics*. Holt, Rinehart and Winston, 1976.

61. Patil V, Capone A, Strauf S, Yang E-H. Improved photoresponse with enhanced photoelectric contribution in fully suspended graphene photodetectors. *Sci Rep* 2013, **3**.

62. Richards PL. Bolometers for infrared and millimeter waves. *Journal of Applied Physics* 1994, **76**(1)**:** 1-24.

63. Novoselov KS, Jiang D, Schedin F, Booth TJ, Khotkevich VV, Morozov SV, *et al.* Two-dimensional atomic crystals. *Proceedings of the National Academy of Sciences of the United States of America* 2005, **102**(30)**:** 10451-10453.

64. Li H, Wu J, Huang X, Lu G, Yang J, Lu X, *et al.* Rapid and Reliable Thickness Identification of Two-Dimensional Nanosheets Using Optical Microscopy. *ACS Nano* 2013, **7**(11)**:** 10344-10353.

65. Li H, Wu J, Yin Z, Zhang H. Preparation and Applications of Mechanically Exfoliated Single-Layer and Multilayer MoS2 and WSe2 Nanosheets. *Accounts of Chemical Research* 2014, **47**(4)**:** 1067-1075.

66. Najmaei S, Liu Z, Zhou W, Zou X, Shi G, Lei S, *et al.* Vapour phase growth and grain boundary structure of molybdenum disulphide atomic layers. *Nature Materials* 2013, **12:** 754.

67. Lu X, Utama MIB, Lin J, Gong X, Zhang J, Zhao Y, *et al.* Large-Area Synthesis of Monolayer and Few-Layer MoSe2 Films on SiO2 Substrates. *Nano Letters* 2014, **14**(5)**:** 2419-2425.

68. Bointon TH, Barnes MD, Russo S, Craciun MF. High Quality Monolayer Graphene Synthesized by Resistive Heating Cold Wall Chemical Vapor Deposition. *Advanced Materials* 2015, **27**(28)**:** 4200-4206.

69. Britnell L, Gorbachev RV, Jalil R, Belle BD, Schedin F, Mishchenko A, *et al.* Field-Effect Tunneling Transistor Based on Vertical Graphene Heterostructures. *Science* 2012, **335**(6071)**:** 947-950.

70. Georgiou T, Jalil R, Belle BD, Britnell L, Gorbachev RV, Morozov SV, *et al.* Vertical field-effect transistor based on graphene-WS2 heterostructures for flexible and transparent electronics. *Nat Nano* 2013, **8**(2)**:** 100-103.

71. Sup Choi M, Lee G-H, Yu Y-J, Lee D-Y, Hwan Lee S, Kim P, *et al.* Controlled charge trapping by molybdenum disulphide and graphene in ultrathin heterostructured memory devices. *Nature Communications* 2013, **4:** 1624.

72. Bertolazzi S, Krasnozhon D, Kis A. Nonvolatile Memory Cells Based on MoS2/Graphene Heterostructures. *ACS Nano* 2013, **7**(4)**:** 3246-3252.

73. Hong X, Kim J, Shi S-F, Zhang Y, Jin C, Sun Y, *et al.* Ultrafast charge transfer in atomically thin MoS2/WS2 heterostructures. *Nature Nanotechnology* 2014, **9:** 682.

74. Wang H, Zhang C, Chan W, Tiwari S, Rana F. Ultrafast response of monolayer molybdenum disulfide photodetectors. *Nature Communications* 2015, **6:** 8831.

75. MassicotteM, SchmidtP, ViallaF, Schädler KG, Reserbat Plantey A, WatanabeK, *et al.* Picosecond photoresponse in van der Waals heterostructures. *Nat Nano* 2016, **11**(1)**:** 42-46.

76. Mehew JD, Unal S, Torres Alonso E, Jones GF, Fadhil Ramadhan S, Craciun MF, *et al.* Fast and Highly Sensitive Ionic-Polymer-Gated WS2–Graphene Photodetectors. *Advanced Materials* 2017**:** 1700222-n/a.

77. Cheng R, Li D, Zhou H, Wang C, Yin A, Jiang S, *et al.* Electroluminescence and Photocurrent Generation from Atomically Sharp WSe2/MoS2 Heterojunction p–n Diodes. *Nano Letters* 2014, **14**(10)**:** 5590-5597.

78. Withers F, Del Pozo-Zamudio O, Mishchenko A, Rooney AP, Gholinia A, Watanabe K, *et al.* Light-emitting diodes by band-structure engineering in van der Waals heterostructures. *Nat Mater* 2015, **14**(3)**:** 301-306.

79. Withers F, Del Pozo-Zamudio O, Schwarz S, Dufferwiel S, Walker PM, Godde T, *et al.* WSe2 Light-Emitting Tunneling Transistors with Enhanced Brightness at Room Temperature. *Nano Letters* 2015, **15**(12)**:** 8223-8228.

80. DasA, PisanaS, ChakrabortyB, PiscanecS, Saha SK, Waghmare UV, *et al.* Monitoring dopants by Raman scattering in an electrochemically top-gated graphene transistor. *Nat Nano* 2008, **3**(4)**:** 210-215.

81. Pisana S, Lazzeri M, Casiraghi C, Novoselov KS, Geim AK, Ferrari AC, *et al.* Breakdown of the adiabatic Born–Oppenheimer approximation in graphene. *Nature Materials* 2007, **6:** 198.

82. Stampfer C, Molitor F, Graf D, Ensslin K, Jungen A, Hierold C, *et al.* Raman imaging of doping domains in graphene on SiO2. *Applied Physics Letters* 2007, **91**(24)**:** 241907.

83. Casiraghi C. Doping dependence of the Raman peaks intensity of graphene close to the Dirac point. *Physical Review B* 2009, **80**(23)**:** 233407.

84. Froehlicher G, Berciaud S. Raman spectroscopy of electrochemically gated graphene transistors: Geometrical capacitance, electron-phonon, electron-electron, and electron-defect scattering. *Physical Review B* 2015, **91**(20)**:** 205413.

85. Ando T. Anomaly of Optical Phonon in Monolayer Graphene. *Journal of the Physical Society of Japan* 2006, **75**(12)**:** 124701.

86. Lazzeri M, Mauri F. Nonadiabatic Kohn Anomaly in a Doped Graphene Monolayer. *Physical Review Letters* 2006, **97**(26)**:** 266407.

87. Yan J, Zhang Y, Kim P, Pinczuk A. Electric Field Effect Tuning of Electron-Phonon Coupling in Graphene. *Physical Review Letters* 2007, **98**(16)**:** 166802.

88. Ryan B, Luiz Gustavo C, Lukas N. Raman characterization of defects and dopants in graphene. *Journal of Physics: Condensed Matter* 2015, **27**(8)**:** 083002.

89. Peres NMR, Guinea F, Castro Neto AH. Electronic properties of disordered two-dimensional carbon. *Physical Review B* 2006, **73**(12)**:** 125411.

90. Lazzeri M, Piscanec S, Mauri F, Ferrari AC, Robertson J. Phonon linewidths and electron-phonon coupling in graphite and nanotubes. *Physical Review B* 2006, **73**(15)**:** 155426.

91. Marianetti CA, Yevick HG. Failure Mechanisms of Graphene under Tension. *Physical Review Letters* 2010, **105**(24)**:** 245502.

92. Liu F, Ming P, Li J. Ab initio calculation of ideal strength and phonon instability of graphene under tension. *Physical Review B* 2007, **76**(6)**:** 064120.

93. Niclas SM, Sebastian H, Miriam Peña A, Patryk K, Sören W, Nick C, *et al.* Evaluating arbitrary strain configurations and doping in graphene with Raman spectroscopy. *2D Materials* 2018, **5**(1)**:** 015016.

94. Mohiuddin TMG, Lombardo A, Nair RR, Bonetti A, Savini G, Jalil R, *et al.* Uniaxial strain in graphene by Raman spectroscopy: G peak splitting,

Gr\"uneisen parameters, and sample orientation. *Physical Review B* 2009, **79**(20)**:** 205433.

95. Shioya H, Craciun MF, Russo S, Yamamoto M, Tarucha S. Straining Graphene Using Thin Film Shrinkage Methods. *Nano Letters* 2014, **14**(3)**:** 1158-1163.

96. Huang M, Yan H, Chen C, Song D, Heinz TF, Hone J. Phonon softening and crystallographic orientation of strained graphene studied by Raman spectroscopy. *Proceedings of the National Academy of Sciences* 2009, **106**(18)**:** 7304-7308.

97. Yoon D, Son Y-W, Cheong H. Strain-Dependent Splitting of the Double-Resonance Raman Scattering Band in Graphene. *Physical Review Letters* 2011, **106**(15)**:** 155502.

98. Androulidakis C, Koukaras EN, Parthenios J, Kalosakas G, Papagelis K, Galiotis C. Graphene flakes under controlled biaxial deformation. 2015, **5:** 18219.

99. Lee JE, Ahn G, Shim J, Lee YS, Ryu S. Optical separation of mechanical strain from charge doping in graphene. *Nat Commun* 2012, **3:** 1024.

100. Morozov SV, Novoselov KS, Katsnelson MI, Schedin F, Elias DC, Jaszczak JA, *et al.* Giant Intrinsic Carrier Mobilities in Graphene and Its Bilayer. *Physical Review Letters* 2008, **100**(1)**:** 016602.

101. Cho JH, Lee J, He Y, Kim BS, Lodge TP, Frisbie CD. High-Capacitance Ion Gel Gate Dielectrics with Faster Polarization Response Times for Organic Thin Film Transistors. *Advanced Materials* 2008, **20**(4)**:** 686-690.

102. Shimotani H, Asanuma H, Tsukazaki A, Ohtomo A, Kawasaki M, Iwasa Y. Insulator-to-metal transition in ZnO by electric double layer gating. *Applied Physics Letters* 2007, **91**(8)**:** 082106.

103. Ye J, Craciun MF, Koshino M, Russo S, Inoue S, Yuan H, *et al.* Accessing the transport properties of graphene and its multilayers at high carrier density. *Proceedings of the National Academy of Sciences* 2011, **108**(32)**:** 13002-13006.

104. Chen F, Xia J, Tao N. Ionic Screening of Charged-Impurity Scattering in Graphene. *Nano Letters* 2009, **9**(4)**:** 1621-1625.

105. Sakaki H, Noda T, Hirakawa K, Tanaka M, Matsusue T. Interface roughness scattering in GaAs/AlAs quantum wells. *Applied Physics Letters* 1987, **51**(23)**:** 1934-1936.

106. Jena D. Tunneling Transistors Based on Graphene and 2-D Crystals. *Proceedings of the IEEE* 2013, **101**(7)**:** 1585-1602.

107. Kang J, Cao W, Xie X, Sarkar D, Liu W, Banerjee K. Graphene and beyond-graphene 2D crystals for next-generation green electronics. SPIE Defense + Security; 2014: SPIE; 2014. p. 7.

108. Haigh SJ, Gholinia A, Jalil R, Romani S, Britnell L, Elias DC, *et al.* Cross-sectional imaging of individual layers and buried interfaces of graphene-based heterostructures and superlattices. *Nat Mater* 2012, **11**(9)**:** 764-767.

109. Andres C-G, Michele B, Rianda M, Vibhor S, Laurens J, Herre SJvdZ, *et al.* Deterministic transfer of two-dimensional materials by all-dry viscoelastic stamping. *2D Materials* 2014, **1**(1)**:** 011002.

110. Shioya H, Russo S, Yamamoto M, Craciun MF, Tarucha S. Electron States of Uniaxially Strained Graphene. *Nano Letters* 2015, **15**(12)**:** 7943-7948.

111. Chen JH, Jang C, Adam S, Fuhrer MS, Williams ED, Ishigami M. Charged-impurity scattering in graphene. *Nat Phys* 2008, **4**(5)**:** 377-381.

112. Ishigami M, Chen JH, Cullen WG, Fuhrer MS, Williams ED. Atomic Structure of Graphene on SiO2. *Nano Letters* 2007, **7**(6)**:** 1643-1648.

113. Neumann C, Reichardt S, Venezuela P, Drogeler M, Banszerus L, Schmitz M, *et al.* Raman spectroscopy as probe of nanometre-scale strain variations in graphene. *Nat Commun* 2015, **6**.

114. Yankowitz M, Xue J, Cormode D, Sanchez-Yamagishi JD, Watanabe K, Taniguchi T, *et al.* Emergence of superlattice Dirac points in graphene on hexagonal boron nitride. *Nat Phys* 2012, **8**(5)**:** 382-386.

115. Woods CR, Britnell L, Eckmann A, Ma RS, Lu JC, Guo HM, *et al.* Commensurate-incommensurate transition in graphene on hexagonal boron nitride. *Nat Phys* 2014, **10**(6)**:** 451-456.

116. Ponomarenko LA, Gorbachev RV, Yu GL, Elias DC, Jalil R, Patel AA, *et al.* Cloning of Dirac fermions in graphene superlattices. *Nature* 2013, **497**(7451)**:** 594-597.

117. Hu J, Rosenbaum TF. Classical and quantum routes to linear magnetoresistance. *Nat Mater* 2008, **7**(9)**:** 697-700.

118. Kozlova NV, Mori N, Makarovsky O, Eaves L, Zhuang QD, Krier A, *et al.* Linear magnetoresistance due to multiple-electron scattering by low-mobility islands in an inhomogeneous conductor. *Nature Communications* 2012, **3:** 1097.

119. Friedman AL, Tedesco JL, Campbell PM, Culbertson JC, Aifer E, Perkins FK, *et al.* Quantum Linear Magnetoresistance in Multilayer Epitaxial Graphene. *Nano Letters* 2010, **10**(10)**:** 3962-3965.

120. Gopinadhan K, Shin YJ, Yudhistira I, Niu J, Yang H. Giant magnetoresistance in single-layer graphene flakes with a gate-voltage-tunable weak antilocalization. *Physical Review B* 2013, **88**(19)**:** 195429.

121. Wang WJ, Gao KH, Li ZQ, Lin T, Li J, Yu C, *et al.* Classical linear magnetoresistance in epitaxial graphene on SiC. *Applied Physics Letters* 2014, **105**(18)**:** 182102.

122. Novak M, Sasaki S, Segawa K, Ando Y. Large linear magnetoresistance in the Dirac semimetal TlBiSSe. *Physical Review B* 2015, **91**(4)**:** 041203.

123. Liu Y, Yudhistira I, Yang M, Laksono E, Luo YZ, Chen J, *et al.* Phonon-Mediated Colossal Magnetoresistance in Graphene/Black Phosphorus Heterostructures. *Nano Letters* 2018.

124. Ali MN, Xiong J, Flynn S, Tao J, Gibson QD, Schoop LM, *et al.* Large, non-saturating magnetoresistance in WTe2. *Nature* 2014, **514**(7521)**:** 205-208.

125. Wang ZH, Yang L, Li XJ, Zhao XT, Wang HL, Zhang ZD, *et al.* Granularity Controlled Nonsaturating Linear Magnetoresistance in Topological Insulator Bi2Te3 Films. *Nano Letters* 2014, **14**(11)**:** 6510-6514.

126. Koenig SP, Doganov RA, Schmidt H, Neto AHC, Özyilmaz B. Electric field effect in ultrathin black phosphorus. *Applied Physics Letters* 2014, **104**(10)**:** 103106.

127. Churchill HOH, Jarillo-Herrero P. Phosphorus joins the family. *Nature Nanotechnology* 2014, **9:** 330.

128. Liao Z-M, Wu H-C, Kumar S, Duesberg GS, Zhou Y-B, Cross GLW, *et al.* Large Magnetoresistance in Few Layer Graphene Stacks with Current Perpendicular to Plane Geometry. *Advanced Materials* 2012, **24**(14)**:** 1862-1866.

129. Abrikosov AA. Quantum magnetoresistance. *Physical Review B* 1998, **58**(5)**:** 2788-2794.

130. Khodkov T, Khrapach I, Craciun MF, Russo S. Direct Observation of a Gate Tunable Band Gap in Electrical Transport in ABC-Trilayer Graphene. *Nano Letters* 2015, **15**(7)**:** 4429-4433.

131. Khodkov T, Withers F, Christopher Hudson D, Felicia Craciun M, Russo S. Electrical transport in suspended and double gated trilayer graphene. *Applied Physics Letters* 2012, **100**(1)**:** 013114.

132. Dröscher S, Roulleau P, Molitor F, Studerus P, Stampfer C, Ensslin K, *et al.* Quantum capacitance and density of states of graphene. *Physica Scripta* 2012, **2012**(T146)**:** 014009.

133. Fang T, Konar A, Xing H, Jena D. Carrier statistics and quantum capacitance of graphene sheets and ribbons. *Applied Physics Letters* 2007, **91**(9)**:** 092109.

134. Guo J, Yoon Y, Ouyang Y. Gate Electrostatics and Quantum Capacitance of Graphene Nanoribbons. *Nano Letters* 2007, **7**(7)**:** 1935-1940.

135. Giannazzo F, Sonde S, Raineri V, Rimini E. Screening Length and Quantum Capacitance in Graphene by Scanning Probe Microscopy. *Nano Letters* 2009, **9**(1)**:** 23-29.

136. Ponomarenko L, Yang R, Gorbachev R, Blake P, Mayorov A, Novoselov K, *et al.* Density of States and Zero Landau Level Probed through Capacitance of Graphene. *Physical Review Letters* 2010, **105**(13)**:** 136801.

137. Cheremisin MV. Quantum capacitance of the monolayer graphene. *Physica E: Low-dimensional Systems and Nanostructures* 2015, **69:** 153-158.

138. Sonde S, Giannazzo F, Raineri V, Rimini E. Dielectric thickness dependence of capacitive behavior in graphene deposited on silicon dioxide. *Journal of Vacuum Science & Technology B: Microelectronics and Nanometer Structures Processing, Measurement, and Phenomena* 2009, **27**(2)**:** 868-873.

139. Ponomarenko LA, Yang R, Mohiuddin TM, Katsnelson MI, Novoselov KS, Morozov SV, *et al.* Effect of a High-$\ensuremath{\kappa}$ Environment on Charge Carrier Mobility in Graphene. *Physical Review Letters* 2009, **102**(20)**:** 206603.

140. Fenton DE, Parker JM, Wright PV. Complexes of alkali metal ions with poly(ethylene oxide). *Polymer* 1973, **14**(11)**:** 589.

141. Wright PV. Electrical conductivity in ionic complexes of poly(ethylene oxide). *British Polymer Journal* 1975, **7**(5)**:** 319-327.

142. Xue Z, He D, Xie X. Poly(ethylene oxide)-based electrolytes for lithium-ion batteries. *Journal of Materials Chemistry A* 2015, **3**(38)**:** 19218-19253.

143. Ferloni P, Chiodelli G, Magistris A, Sanesi M. Ion transport and thermal properties of poly(ethylene oxide) - LiClO4 polymer electrolytes. *Solid State Ionics* 1986, **18:** 265-270.

144. Jena D, Konar A. Enhancement of Carrier Mobility in Semiconductor Nanostructures by Dielectric Engineering. *Physical Review Letters* 2007, **98**(13)**:** 136805.

145. Kim BJ, Jang H, Lee S-K, Hong BH, Ahn J-H, Cho JH. High-Performance Flexible Graphene Field Effect Transistors with Ion Gel Gate Dielectrics. *Nano Letters* 2010, **10**(9)**:** 3464-3466.

146. Chen F, Xia J, Ferry DK, Tao N. Dielectric Screening Enhanced Performance in Graphene FET. *Nano Letters* 2009, **9**(7)**:** 2571-2574.

147. Lu C, Fu Q, Huang S, Liu J. Polymer Electrolyte-Gated Carbon Nanotube Field-Effect Transistor. *Nano Letters* 2004, **4**(4)**:** 623-627.

148. Xia JL, Chen F, Wiktor P, Ferry DK, Tao NJ. Effect of Top Dielectric Medium on Gate Capacitance of Graphene Field Effect Transistors: Implications in Mobility Measurements and Sensor Applications. *Nano Letters* 2010, **10**(12)**:** 5060-5064.

149. RadisavljevicB, RadenovicA, BrivioJ, GiacomettiV, KisA. Single-layer MoS2 transistors. *Nat Nano* 2011, **6**(3)**:** 147-150.

150. Braga D, Gutiérrez Lezama I, Berger H, Morpurgo AF. Quantitative Determination of the Band Gap of WS2 with Ambipolar Ionic Liquid-Gated Transistors. *Nano Letters* 2012, **12**(10)**:** 5218-5223.

151. Ming-Wei L, Lezhang L, Qing L, Xuebin T, Kulwinder SD, Peng Z, *et al.* Mobility enhancement and highly efficient gating of monolayer MoS 2 transistors with polymer electrolyte. *Journal of Physics D: Applied Physics* 2012, **45**(34)**:** 345102.

152. Ubrig N, Jo S, Berger H, Morpurgo AF, Kuzmenko AB. Scanning photocurrent microscopy reveals electron-hole asymmetry in ionic liquid-gated WS2 transistors. *Applied Physics Letters* 2014, **104**(17)**:** 171112.

153. Kuiri M, Chakraborty B, Paul A, Das S, Sood AK, Das A. Enhancing photoresponsivity using MoTe2-graphene vertical heterostructures. *Applied Physics Letters* 2016, **108**(6)**:** 063506.

154. Namgung S, Shaver J, Oh S-H, Koester SJ. Multimodal Photodiode and Phototransistor Device Based on Two-Dimensional Materials. *ACS Nano* 2016, **10**(11)**:** 10500-10506.

155. Furchi MM, Polyushkin DK, Pospischil A, Mueller T. Mechanisms of Photoconductivity in Atomically Thin MoS2. *Nano Letters* 2014, **14**(11)**:** 6165-6170.

156. Britnell L, Ribeiro RM, Eckmann A, Jalil R, Belle BD, Mishchenko A, *et al.* Strong Light-Matter Interactions in Heterostructures of Atomically Thin Films. *Science* 2013, **340**(6138)**:** 1311-1314.

157. Yu WJ, Liu Y, Zhou H, Yin A, Li Z, Huang Y, *et al.* Highly efficient gate-tunable photocurrent generation in vertical heterostructures of layered materials. *Nature Nanotechnology* 2013, **8:** 952.

158. Kufer D, Konstantatos G. Highly Sensitive, Encapsulated MoS2 Photodetector with Gate Controllable Gain and Speed. *Nano Letters* 2015, **15**(11)**:** 7307-7313.

159. Roy K, Padmanabhan M, Goswami S, Sai TP, Ramalingam G, Raghavan S, *et al.* Graphene–MoS2 hybrid structures for multifunctional photoresponsive memory devices. *Nature Nanotechnology* 2013, **8:** 826.

160. Koppens FHL, Mueller T, Avouris P, Ferrari AC, Vitiello MS, Polini M. Photodetectors based on graphene, other two-dimensional materials and hybrid systems. *Nat Nano* 2014, **9**(10)**:** 780-793.

161. Konstantatos G, Badioli M, Gaudreau L, Osmond J, Bernechea M, de Arquer FPG, *et al.* Hybrid graphene-quantum dot phototransistors with ultrahigh gain. *Nat Nano* 2012, **7**(6)**:** 363-368.

162. Abanin DA, Morozov SV, Ponomarenko LA, Gorbachev RV, Mayorov AS, Katsnelson MI, *et al.* Giant Nonlocality Near the Dirac Point in Graphene. *Science* 2011, **332**(6027)**:** 328-330.

163. Han W, Kawakami RK, Gmitra M, Fabian J. Graphene spintronics. *Nat Nano* 2014, **9**(10)**:** 794-807.

164. Atsufumi H, Koki T. Future perspectives for spintronic devices. *Journal of Physics D: Applied Physics* 2014, **47**(19)**:** 193001.

165. Shimazaki Y, Yamamoto M, Borzenets IV, Watanabe K, Taniguchi T, Tarucha S. Generation and detection of pure valley current by electrically induced Berry curvature in bilayer graphene. *Nat Phys* 2015, **11**(12)**:** 1032-1036.

166. Sui M, Chen G, Ma L, Shan W-Y, Tian D, Watanabe K, *et al.* Gate-tunable topological valley transport in bilayer graphene. *Nat Phys* 2015, **advance online publication**.

167. Schaibley JR, Yu H, Clark G, Rivera P, Ross JS, Seyler KL, *et al.* Valleytronics in 2D materials. *Nature Reviews Materials* 2016, **1:** 16055.

168. Craciun MF, RussoS, YamamotoM, Oostinga JB, Morpurgo AF, TaruchaS. Trilayer graphene is a semimetal with a gate-tunable band overlap. *Nat Nano* 2009, **4**(6)**:** 383-388.

169. -Hewlett-Packard- A. HCNR200/1 High-Linearity Analog Optocouplers Datasheet. 2015.

Chapter 8

Summary

The aim of this thesis was to investigate how to make high response magnetic and optical sensors based on graphene.

Throughout the first experimental chapter 4, I demonstrate that the bubbles at the interface between graphene and hBN generate an inhomogeneity in the carrier mobility. This is inferred through a Raman spectroscopy study. An analysis of the spatial Raman map across the graphene channel has revealed that the bubble areas have a higher doping level than the rest of the channel. I exploit this to probe LMR based on the inhomogeneity model. I then implemented this device to sense the change in magnetic field, which has led to LMR up to 350%. This value could be enhanced by engineering in-homogeneities in graphene. There are many ways to engineer in-homogeneities, for example by placing graphene on a substrate with holes.

Another concept related to LMR was presented in chapter 5 by exploiting the large dependence of the mobility in graphene on the Fermi level position. In this study, LMR was obtained in the presence of two parallel gases with different mobility. This was implemented through tuning the mobility of two graphene transistors via the

back gate, in different configurations. Further work can be done through finding two different high mobility gases for instance graphene with TMDs materials or traditional semiconductors.

In chapter 6 we show that the ionic polymer electrolyte improves the optoelectronic properties of hybrid graphene-WS_2 photodetectors. Our bandwidths reach up to 1.5 kHz, the Responsivity R = 106 A W^{-1} and detectivity D^* = 3.8 × 10^{11} Jones are observed, approaching that of single-photon counters. We interpreted our data based on the photo-gating mechanism. This improvement is due to the mobile ions in the polymer that are neutralizing the charged impurities at the interface. The combination of both high responsivity and fast response times makes these photodetectors suitable for video-frame-rate imaging applications. The future work can go further through controlling the transit time for the photogeneration charge between graphene and semiconductor by combining the top gate with the back gate. In addition, the role of charge traps states in the hybrid devices could be studied, using high mobility semiconductors.